Numerical analysis of flow structures and bed entrainment in turbulent open-channel flow

Ma, Jianmin

For additional information about this publication click this link.
https://qmro.qmul.ac.uk/jspui/handle/123456789/524

Numerical analysis of flow structures and bed entrainment in turbulent open-channel flow

Jianmin Ma

A thesis submitted to the University of London

for the degree of Doctor of Philosophy

Department of Engineering

Queen Mary, University of London

Mile End Road

London   E1 4NS

August, 2009

I hereby declare that this thesis is my own work, and that any material from the work of other people, published or otherwise, is fully acknowledged in accordance with the standard referring practices of the discipline.

Signed:

(Jianmin Ma)

Abstract

The results from a Direct Numerical Simulation (DNS) and a Large Eddy Simulation (LES) are employed to study the large-scale coherent structures and bed entrainment in the turbulent open-channel flow. The gravel bed is represented by a hexagonal arrangement of uniform spheres.

The large-scale coherent structures are composed of a group of quasi-streamwise vortices and asymmetric hairpin vortices. The meandering structures are shown to be longer than the length of the computational box, more than 20 times the effective flow depth in this study, and the width tends to be one order of magnitude smaller than the length. The signature of the large-scale motion is elongated local maximum of streamwise velocity. It is also found that these structures contribute substantially to both of the Reynolds Stress (RS) and the Turbulent Kinetic Energy (TKE).

The entrainment of bed gravels is investigated by the three-dimensional analysis of the relationship between near-wall coherent structures and the force moments exerted on the particles. It is found that the spanwise drag moment (M_{D2}) is of the same order of magnitude compared with the streamwise drag moment (M_{D1}). The majority of M_{D2} originates from pressure whilst the viscous force plays as an important role as pressure for M_{D1}. The contributions of the forces at different heights of the particle to M_{D1} and M_{D2} are explored. The quasi-streamwise vortices are strongly associated with M_{D2} and the ejections are shown to be more favorable for bed entrainment than the sweeps in this bed condition.

Acknowledgements

First of all, I would like to thank my supervisor Prof. John J. R. Williams for his guidance and support during the last three years. His valuable advice not only helped me improve the quality of my research work, but changed my view point of the world.

I wish to thank my fellow, Mr. Zaheer Ikram, for his support during my research. I want to give my thanks to the members of staff in the Department of Engineering and Queen Mary College, in particular, Prof. David Lee, Dr. Eldad Avital, Mr. Peter Smith, Mr. Jonathon Hills, Mr. Raymold Lam, Mr. Alem Million.

I would also like to thank my family, my friends and the academic staff in the School of Civil Engineering at Tianjin University, from the application of the Ph.D program all the way to this stage.

Table of Contents

Chapter 3

Large-scale Coherent Structures

Chapter 4

Structure Growth in the Larger Box

Chapter 5

Near-wall Coherent Structures

Chapter 6

Entrainment of Sediment Bed

Chapter 7

Conclusions and Recommendations

Table of Figures

Nomenclature

The following symbols are used in this thesis:

$$b_i \quad = \quad \text{body force component} \ (\ i = x, y, z\ )$$

$$C_s \quad = \quad \text{Smagorinsky model parameter}$$

$$d \quad = \quad \text{depth of channel}$$

$$E \quad = \quad \text{enstrophy}$$

$$= \quad (\overline{\omega_x^{\,2}} + \overline{\omega_y^{\,2}} + \overline{\omega_z^{\,2}})\big/2$$

$$e \quad = \quad \text{exposure of cube above upstream bed level}$$

$$F_{D1} \quad = \quad \text{streamwise drag force}$$

$$F_{D2} \quad = \quad \text{spanwise drag force}$$

$$F_D \quad = \quad \text{drag force}$$

$$F_L \quad = \quad \text{lift force}$$

$$F_r \quad = \quad \text{Froude number}$$

$$F_W \quad = \quad \text{submerged gravitational force}$$

$$g \quad = \quad \text{accelation of gravitity}$$

$$h \quad = \quad \text{channel height}$$

$$K \quad = \quad \text{turbulent kinetic energy}$$

$$= \quad (\overline{u'^2} + \overline{v'^2} + \overline{w'^2})\big/2$$

$$k_s \quad = \quad \text{equivalent sand roughness}$$

$$k_s^+ \quad = \quad \text{roughness Reynolds number}$$

$$= \quad k_s\, u_\tau / v$$

$$L \quad = \quad \text{characteristic length}$$

$$L_D \quad = \quad \text{lever arm of drag force}$$

$$L_L \quad = \quad \text{lever arm of lift force}$$

$$L_W \quad = \quad \text{lever arm of submerged gravitational force}$$

$$l_{z135} \quad = \quad \text{inclination angle of } 135^0$$

$$l_{z45} \quad = \quad \text{inclination angle of } 45^0$$

$$L_{1\sim5} \quad = \quad \text{five adjacent two-point correlations at the location}$$

of large coherent structures

$$M_{D1} \quad = \quad \text{moment of streamwise drag force}$$

$$M_{D2} \quad = \quad \text{moment of spanwise drag force}$$

$$M_{D1i} \quad = \quad \text{moment of streamwise drag force from different}$$

vertical regions ($i = 1 \sim 8$)

$$M_{D2i} \quad = \quad \text{moment of spanwise drag force from different}$$

vertical regions ($i = 1 \sim 8$)

$$M_L \quad = \quad \text{moment of lift force}$$

$$M_P \quad = \quad \text{moment contributed from pressure}$$

M_V =   moment contributed from viscous force

p =   pressure

P =   probability

P_1 =   pressure at the upstream side of the cube

P_2 =   pressure on top of the cube

P_3 =   pressure at the downstream side of the cube

Q =   the second invariant of velocity gradient tensor

= $\dfrac{1}{2}(\|\Omega\|^2 - \|S\|^2)$

Q_{max} =   maximum of Q

R =   correlation coefficient of Reynolds stress

= $-\overline{u'v'}/(u_{rms}v_{rms})$

R_k =   correlation of Reynolds stress and Turbulent

kinetic energy

= $-\overline{u'v'}/(2k)$

Re^+ =   Reynolds number based on bed shear velocity

= $u_\tau d/v$

R_i =   contribution to M_{DI} from different vertical regions

= M_{DIi}/M_{DI}

Re_θ =   Reynolds number based on momentum thickness

$$= u\,\theta/v$$

$$R_{uu} = \text{two-point spatial correlation}$$

$$= \overline{u(x)u(x+r)}\big/\overline{u^2(x)}$$

$$R_{\_u\_u} = \text{two-point correlation of } u$$

$$= \overline{u(x)u(x+r)}\big/\overline{u^2(x)}$$

$$R_{\_v\_v} = \text{two-point correlation of } v$$

$$= \overline{v(x)v(x+r)}\big/\overline{v^2(x)}$$

$$R_{\_w\_w} = \text{two-point correlation of } w$$

$$= \overline{w(x)w(x+r)}\big/\overline{w^2(x)}$$

$$R_x = \text{cross correlation of } |\omega_x| \text{ and } Q$$

$$= \overline{|\omega_x|Q}\Big/\left(\sqrt{\overline{|\omega_x|^2}}\,\sqrt{\overline{Q^2}}\right)$$

$$R_y = \text{cross correlation of } |\omega_y| \text{ and } Q$$

$$= \overline{|\omega_y|Q}\Big/\left(\sqrt{\overline{|\omega_y|^2}}\,\sqrt{\overline{Q^2}}\right)$$

$$R_z = \text{cross correlation of } |\omega_z| \text{ and } Q$$

$$= \overline{|\omega_z|Q}\Big/\left(\sqrt{\overline{|\omega_z|^2}}\,\sqrt{\overline{Q^2}}\right)$$

$$r = \text{the distance between two different velocity points}$$

$$r_i = \text{contribution to } M_{D2} \text{ from different vertical regions}$$

$$= M_{D2i}\,/\,M_{D2}$$

$$r_{uv} = \text{fractional contribution to total } -u'v'$$

Jianmin Ma

r_{uu} = fractional contribution to total u^2

r_{vv} = fractional contribution to total v^2

r_{ww} = fractional contribution to total w^2

r_{Re} = cumulative Reynolds stress

r_{TKE} = cumulative turbulent kinetic energy

S = strain rate of Q

$\quad$ = $\dfrac{1}{2}\left(\nabla v + (\nabla v)^t\right)$

$|\bar{S}|$ = velocity gradient of smagorinsky model

S_{ij} = strain rate of the large scale

$\quad$ = $\dfrac{1}{2}\left(\dfrac{\partial u_i}{\partial x_j} + \dfrac{\partial u_j}{\partial x_i}\right)$

t = time

U = plane-averaged mean velocity

u = instantaneous velocity

u_b = velocity adjacent to the sediment particle

U_{c1} = convection velocity in the streamwise direction of younger packet

U_{c2} = convection velocity in the streamwise direction of older packet

U_{c3} = convection velocity in the streamwise direction of

yet older packet

$$U^+ = \text{normalized velocity}$$

$$u_i = \text{velocity component in direction } x_i$$

$$u_x = \text{velocity at the location of } x$$

$$u_\tau = \text{bed shear velocity}$$

$$u',v',w' = \text{streamwise, vertical and spanwise turbulent velocity fluctuations}$$

$$u_{rms}, v_{rms} = \text{root mean square of velocity fluctuations}$$

$$= \sqrt{\overline{u'^2}}, \ \sqrt{\overline{v'^2}}$$

$$u'v'_2 = \text{ejection event}$$

$$u'v'_4 = \text{sweep event}$$

$$-\overline{u'v'} = \text{Reynolds stress}$$

$$V_{\Delta x} = \text{characteristic velocity in smagorinsky model}$$

$$v = \text{kinematic viscosity of the fluid}$$

$$v_t = \text{eddy viscosity}$$

$$X = \text{a random variable whose probability is } P$$

$$x_i = \text{Cartesian coordinates}(x, y, z) \text{ for } i = 1, 2, 3$$

$$x, y, z = \text{streamwise, vertical and spanwise Cartesian coordinates}$$

$$y^+ \quad = \quad \text{normalized effective height}$$

$$\rho \quad = \quad \text{density of fluid}$$

$$\omega_x \quad = \quad \text{vorticity component in } x\text{-direction}$$

$$\omega_y \quad = \quad \text{vorticity component in } y\text{-direction}$$

$$\omega_z \quad = \quad \text{vorticity component in } z\text{-direction}$$

$$\Omega \quad = \quad \text{rotate rate of } Q$$

$$= \quad \frac{1}{2}\left(\nabla v - (\nabla v)^t\right)$$

$$\Phi' \quad = \quad \text{pivot angle}$$

$$\Pi \quad = \quad \text{protrusion of cube compared with mean bed level}$$

$$\Delta x \quad = \quad \text{sub-grid scale length}$$

$$\nabla v \quad = \quad \text{velocity gradient tensor}$$

$$= \quad \frac{\partial u_i}{\partial x_j}$$

$$(\nabla v)^t \quad = \quad \text{transpose of velocity gradient tensor}$$

$$DNS_i \quad = \quad \text{instantaneous } DNS \text{ data } (i = 1 \sim 4)$$

$$L\text{-}SS \quad = \quad \text{low-speed streaks}$$

$$H\text{-}SS \quad = \quad \text{high-speed streaks}$$

$$S \quad = \quad \text{streak cycle}$$

$$W \quad = \quad \text{wall cycle}$$

$$SP \quad = \quad \text{stagnation point}$$

DHV = downstream hairpin vortex

PHV = primary hairpin vortex

SHV = secondary hairpin vortex

THV = tertiary hairpin vortex

QSV = quasi-streamwise vortex

$VLSM$ = very large scale motion

Chapter 1
Introduction

1.1 Background

Coherent structures in turbulent flows have been studied extensively during the past few decades as a large number of studies have demonstrated that coherent structures play an important role in turbulence. They determine the velocity distribution, momentum and energy transfer, etc. Their spatial and temporal coherent features indicate that turbulence is not a pure random behavior.

Hairpin vortices, also called horseshoe or omega-shape vortices, are commonly observed coherent structures in turbulent flows. The characteristics of the hairpin vortices, including origin, evolution, contributions to Reynolds Stress (defined as $-u'v'$ in this study) and Turbulent Kinetic Energy, as well as the interactions between the vortices, were explored by different research groups, e.g. Stanford, UIUC, Minnesota, etc. Similar organizations of the hairpin vortices were observed in boundary layer flows, channel flows and pipe flows. The signature of the hairpin vortices is local minimum momentum, between the legs of hairpin vortices. The coalescence of the vortices occurs in both streamwise and spanwise directions. Consequently, very long hairpin vortex packets, also reported as large-scale coherent structures or large-scale motions, are the dominant coherent structures in turbulent flows. These large packets

are shown to contain more than 50% of the Reynolds Stress and 65% of the energy (Guala et al., 2006). However, the organization of the elongated streaks is still not clear. The continuous long regions of high-speed and low-speed streaks cannot be simply explained by the hairpin vortex model.

The role of the near-wall coherent structures on sediment transport is another interesting topic. Since the beginning of last century, the analysis of sediment movement is based on the empirical formulas of drag force and lift force exerted on the particles. The threshold of movement is divided into suspension and rollover. More recently, both experimental and computational works reported the importance of near-wall coherent structures. The entrainment and transport of the sediment particles are closely associated with the well-known bursting events, i.e. ejections and sweeps, and quasi-streamwise vortices. Those entrainment models incorporating coherent structures show good agreement with the observed results. Therefore, a deep understanding of the effect of near-wall coherent structures on sediment entrainment is necessary for more accurate prediction.

1.2 Objective and Approach

The objective of this project is to numerically investigate the characteristics of the coherent structures in rough-wall turbulent flow and the effect of near-wall coherent structures on sediment entrainment. We employ the results of a Direct Numerical Simulation (DNS) and a Large Eddy Simulation (LES), both of which simulate the turbulent shallow flow over a hydraulically rough bed. The sediment gravels are represented by hexagonally arranged uniform spheres, which are fixed on the bed. The channel depth is four times the sphere diameter. The drag and lift force exerted on the particles can be better estimated than through experiments, as it is pretty difficult to measure the velocities and pressures among the bed particles experimentally.

The merging mechanism of large-scale coherent structures is captured by LES; and a Smagorinsky model is used as the sub-grid model for the small eddies. The bed geometry of the LES is exactly the same as that of the DNS. The lengh scale of the large coherent structures is not clear as different research groups report different results. The restriction of the computational or experimental domain is one of the main reasons accounting for the difference. In order to quantify the length scale, we doubled the length and the width of the box to observe the development of the structures in both horizontal directions.

This thesis is divided into seven chapters. In the next chapter, the details of the numerical simulations are described, including numerical techniques,

sub-grid scale model and data validation. In Chapter 3, the characteristics of the large-scale coherent structures are analysed using the data obtained in DNS. In Chapter 4, the growth of the coherent structures due to the increase of computational box by LES is reported. Analysis regarding the force moments exerted on the sphere particles is based on the DNS data. Chapter 5 mainly states the relationship between near-wall coherent structures and force moments. Chapter 6 analyses the features of drag force and lift force moments for the bed entrainment. Finally in Chapter 7, the concluding remarks are given and recommendations for the future work are proposed.

Chapter 2
Methodology

2.1 Direct Numerical Simulation

Direct Numerical Simulation is the complete resolution of the Navier-Stokes equations and continuity equation, without approximation. The computational domain must be larger than the largest eddy and the grid must be smaller than the smallest scales, the Kolmogorov length scale. Due to limitation of grid numbers during the computation, DNS only suits low Reynolds number flows. The computation is carried out on super-computers which require large memory and storage space. (J.H.Ferziger, 2002)

2.1.1 Numerical Techniques

The result of a DNS of the turbulent open-channel flow over a rough-bed is employed (Fig.2.1). The gravel bed is represented by a hexagonal arrangement of uniform spheres, which are fixed on the bed. The sphere diameter is a quarter of flow depth, *d*. The length scale of the numerical box is $4\sqrt{3}d$ in the streamwise direction and *4d* in the spanwise direction. Axes *x, y, z* represent the streamwise, vertical and spanwise directions respectively and, the center of the reference frame is located at the bottom of the channel.
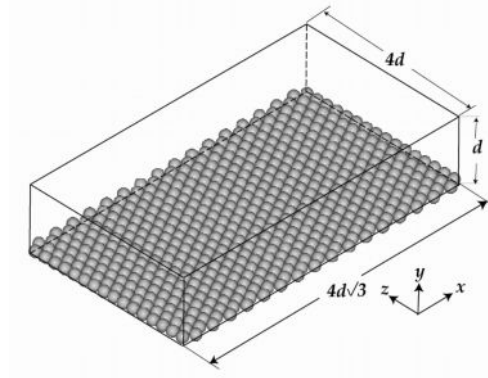
Figure 2.1: Geometry of the DNS (Singh et al. 2007).

The incompressible turbulent flow is governed by the Navier-Stokes equations and the continuity equation

$$\frac{\partial u_i}{\partial t} + \frac{\partial (u_i u_j)}{\partial x_j} = -\frac{1}{\rho}\frac{\partial p}{\partial x_i} + v\frac{\partial^2 u_i}{\partial x_j x_j} + b_i \qquad (1)$$

$$\frac{\partial u_i}{\partial x_i} = 0 \qquad (2)$$

In the above equations, u_i are the velocity components, t is time, ρ is the fluid density, p is the pressure, v is the kinematic viscosity, b_i are the body force components, x_i (i = 1,2,3) are the axes of Cartesian coordinate system.

No-slip and no-penetration conditions are employed on sphere surface and, a stress-free hard lid is used for channel top surface (Handler et al. 1999, Komori et al. 1993). The effect of any free surface disturbances is not considered in this study which is expected to be minimal particularly for

low Froude number ($Fr = U/\sqrt{gL}$) flow. A parallel complex-geometry code was performed in this simulation. Periodic boundary conditions were used in both horizontal directions. The flow Reynolds number Re^+ ($Re^+=u_\tau d/v$) is 533 and the roughness Reynolds number k_s^+ ($k_s^+= k_s u_\tau /v$) is 100 so that the bed is fully rough.

In the simulation, staggered grid with a second order finite difference method is used for spatial discretization and a second order Adams-Bashforth method for time integration. A fictitious domain multi-grid preconditioner with a conjugate gradient method is used for Poisson pressure equation. The simulation was performed as LES for about 30 LETOT (large eddy turnover time) first to establish a fully developed turbulent flow field. Then, the simulation was continued using a DNS grid until statistically steady, by checking the total shear stress profile. We employ a Cartesian grid of resolution of $1024 \times 512 \times 128$ for $4\sqrt{3}d \times 4d \times d$, with grid sizes of 3.6 wall units, 4.2 wall units and 4.2 wall units in *x, y, z* directions respectively. The Kolmogorov length scale is approximately 3.0 wall units. More details regarding the simulation can be found in Singh et al. (2007).

2.1.2 Data Validation

In order to validate the DNS data, simulation results are compared with experimental results. Fig.2.2 is the mean velocity profile. The solid line is DNS data and the dot line represents the log law. The trend of DNS data agrees well with the experimental data and as pointed out in Singh et al.

(2007), the wall roughness has an obvious effect on the velocity defect near the bottom. The turbulence intensities in Fig.2.3 shows that the DNS data generally agree well with the experimental data of Nezu (1977), which were obtained under a close roughness Reynolds number. But there is a discrepancy in the near wall region, possibly due to the unreliable measurements or different roughness condition. The correlation coefficient of Reynolds stress in Fig.2.4 is defined as $R = -\overline{u'v'}/(u_{rms}v_{rms})$ and the correlation between the Reynolds Stress and Turbulent Kinetic Energy $K = (\overline{u'^2} + \overline{v'^2} + \overline{w'^2})/2$ is $R_k = -\overline{u'v'}/(2k)$ in Fig.2.5. Both of the correlations agree well with the data of Nezu (1977), but show a peak below the top of roughness elements, where the statistical information is extremely difficult to obtain experimentally.
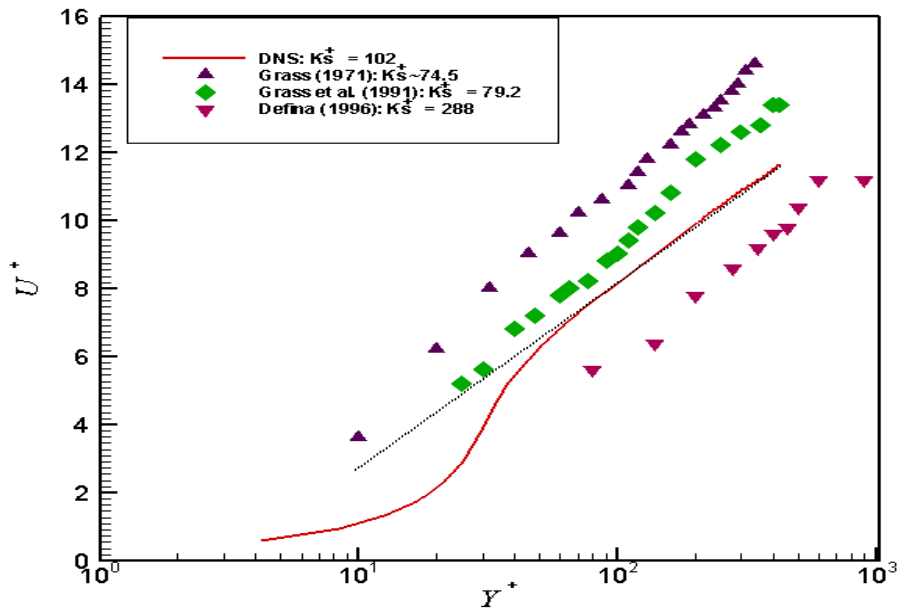
Figure 2.2: Mean velocity profile (U^+ is normalized by u_τ and Y^+ is normalized by d) (Singh et al. 2007).
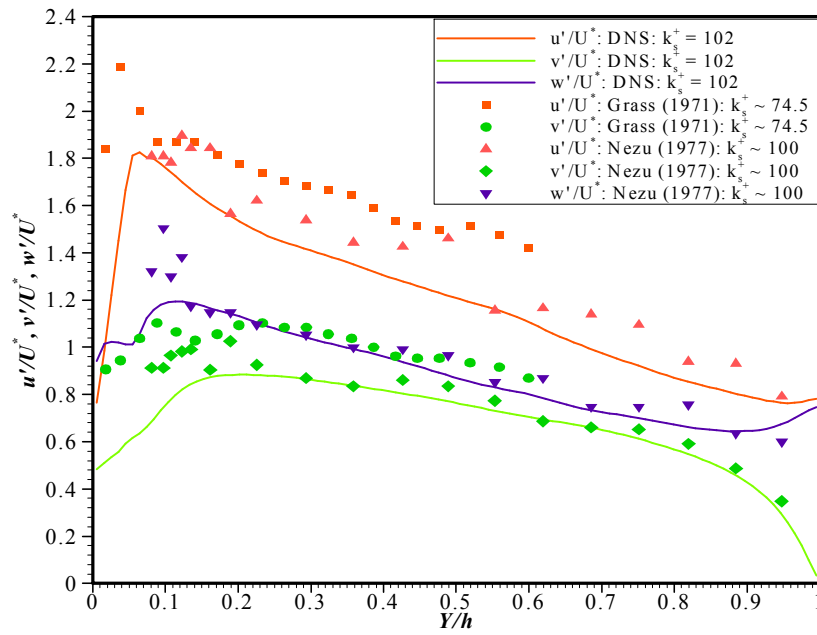
Figure 2.3: Turbulent intensities (Singh et al. 2007).
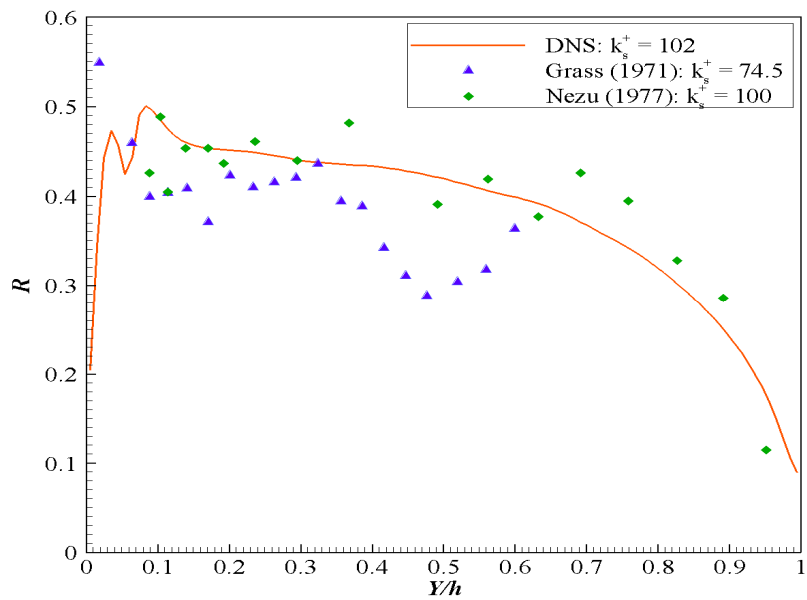
Figure 2.4: Correlation of Reynolds shear stress (Singh et al. 2007).
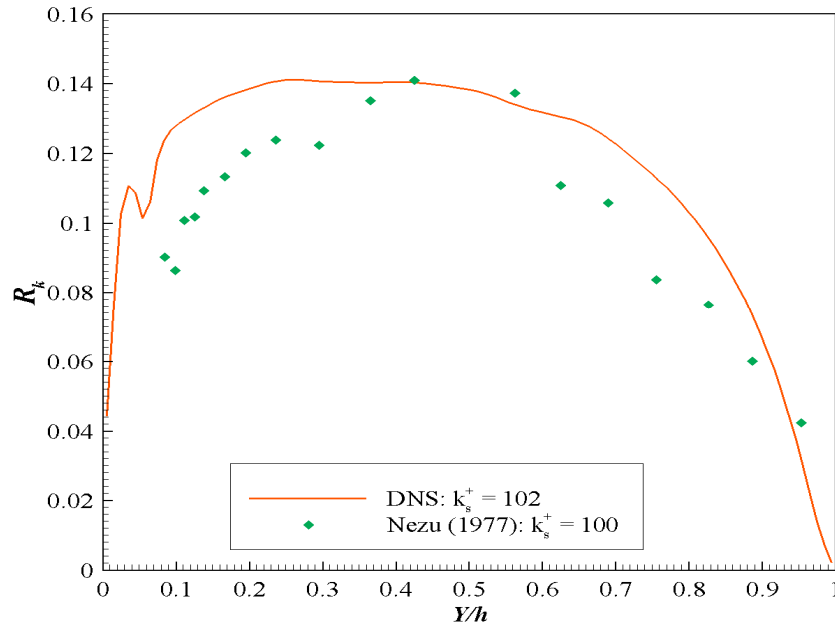
Figure 2.5: Correlation of RS and TKE (Singh et al. 2007).

2.1.3 Computation of Force Moments

Rollover is taken as the main mode for the initiation of movement as in the shallow flow condition, rollover is more possible than suspension for the coarse gravels. M_{D1}, M_{D2} and M_L are moments produced by forces F_{D1}, F_{D2} and F_L in streamwise, spanwise and vertical directions respectively. The forces are composed of two parts: viscous forces along the surface and pressures perpendicular to the surface. The moments are calculated by integrating the moments per unit area on the sphere surface.

As in Fig.2.6, the moments in clockwise direction are taken to be positive whilst anti-clockwise direction negative. Short dash lines in the vertical direction are pivots of M_{D1} and long dash lines in the horizontal direction
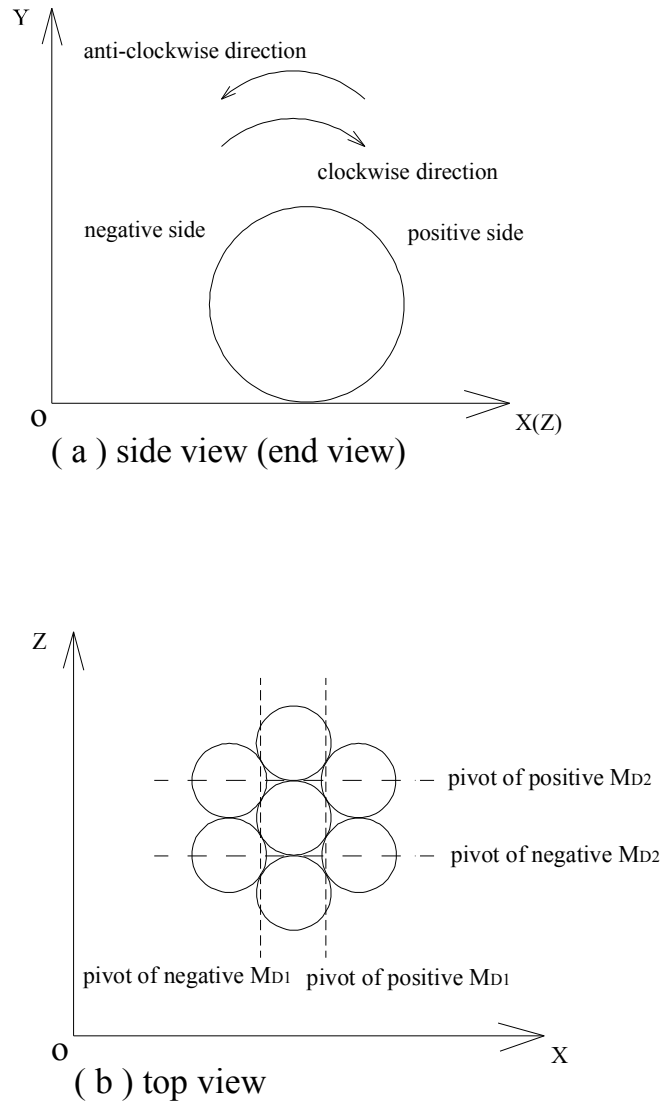
Figure 2.6: Calculation of the force moments: (a) side view (end view) and (b) top view(sphere in centre).

are for M_{D2}. The distances from the sphere center to the pivots of M_{D1} and M_{D2} are different due to the hexagonal arrangement. As a consequence, the calculation of M_{D1} and M_{D2} are different as for M_{D1}, the parts on both sides of the pivot need to be balanced and for M_{D2}, the computation is just integrating the unit moments over the whole sphere. Since different arrangement of the sphere particles may produce different relationships in the real condition, the quatitative results just apply to the ideal arrangement here.

Furthermore, this arrangement represents the gravel beds which have been water-worked, that is, the effect of protrusion of the gravels is neglected. The other factors which may influence the results, e.g. particle shape, size, composition, etc. are entirely simplified.

2.2 Large Eddy Simulation

Large Eddy Simulation is more complicated than Direct Numerical Simulation as it combines computation and modelling. In LES, only the large eddies are calculated whilst the small eddies are modelled by the sub-grid model. Therefore, the eddies are divided into two classes and a critical length scale applies. Because only the large-scale eddies are calculated, LES is computationally less expensive than DNS. In particular, LES is widely employed for high Reynolds number flows and those with complex geometries. (Ferziger, 2002)

2.2.1 Geometries

A LES is carry out based on two computational boxes; both the length and the width of the large box (Fig.2.7) are twice those of the small box. The arrangement of the bed gravels is exactly the same as the condition in the DNS. The grid size of the LES is twice that of the DNS in all of the three dimensions, i.e. 7.2 wall units, 8.4 wall units and 8.4 wall units in x, y, z directions respectively.

2.2.2 Sub-grid Scale Model

We choose the most commonly used sub-grid scale model, Smagorinsky model (Smagorinsky, 1963), as the eddy viscosity model for the LES, which is defined as $v_t = (Cs\Delta x)^2 |\overline{S}|$. Here $|\overline{S}| = \sqrt{2\overline{S_{ij}}\overline{S_{ij}}}$ is the velocity

gradient and the parameter $C_s = 0.09$. The eddy viscosity is assumed to be proportional to the characteristic sub-grid scale length Δx and characteristic velocity $v_{\Delta x} = \Delta x |\bar{S}|$. Although in most of the cases for isotropic turbulence, the parameter may vary as a function of Reynolds number or other parameters, C_s is approximately 0.2. For channel flows, C_s is reduced greatly to be around 0.065 (Ferziger, 2002). Although Smagorinsky model is not ideal for the laminar region near the wall (Blazek, 2001), it is good enough to be employed in this study as the bed is fully rough and the sphere surface is represented by a staircase structure, rather than smooth curve.
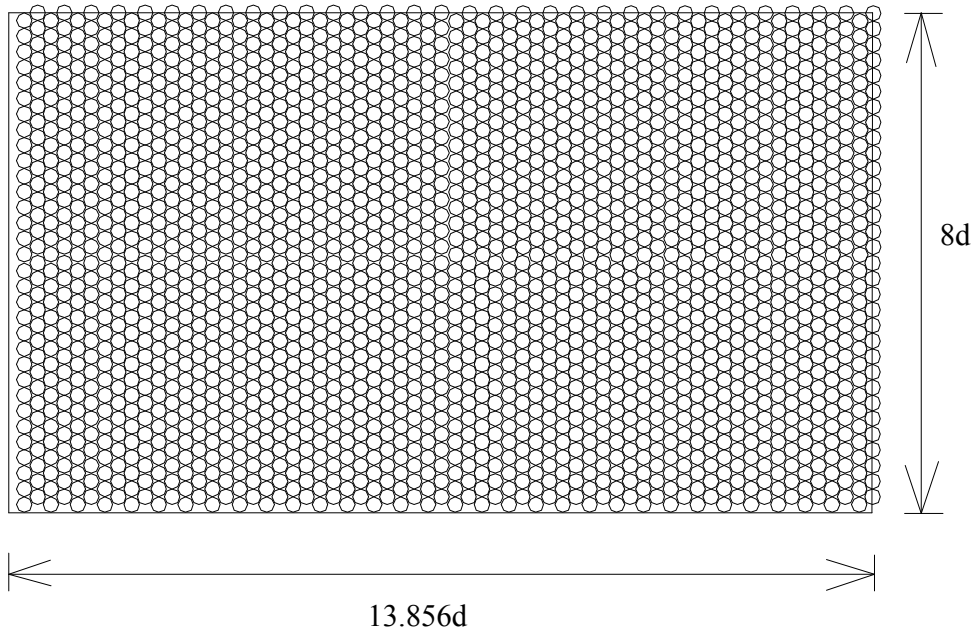
Figure 2.7: Geometry of the LES (top view of the large box).

2.2.3 Data Validation

The LES results are compared with the DNS results (Singh et al., 2007), including mean velocity, turbulence intensities, correlation coefficient of the Reynolds Stress and the correlation coefficient between the Reynolds Stress and the Turbulent Kinetic Energy (Fig.2.8~Fig.2.13). The solid lines denote DNS data, the dash lines denote LES data of the small box and the dash dot dot lines represent LES data of the large box.
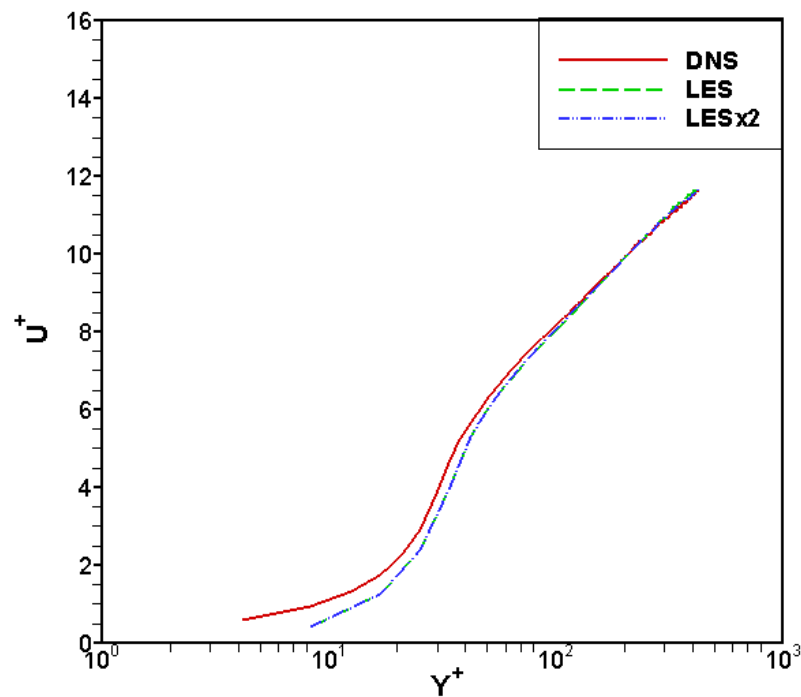
Figure 2.8:   Mean velocity profile

(U^+ is normalized by u_τ and Y^+ is normalized by d).

In general, both of the LES data agree well with the DNS data, though slight differences occur mainly in the near-wall region. Therefore, the Smagorinsky model is not an ideal tool to capture the near-wall turbulence information. But such slight difference due to the small eddies does not affect the investigation of the large scale structures. Furthermore, the statistical information of the large box corresponds better with the DNS than the small box, especially for R and R_k. These differences imply that the size of the computational domain does have an effect on the accuracy of the results, probably due to the influence on the flow structures or just simply from a statistical point of view.
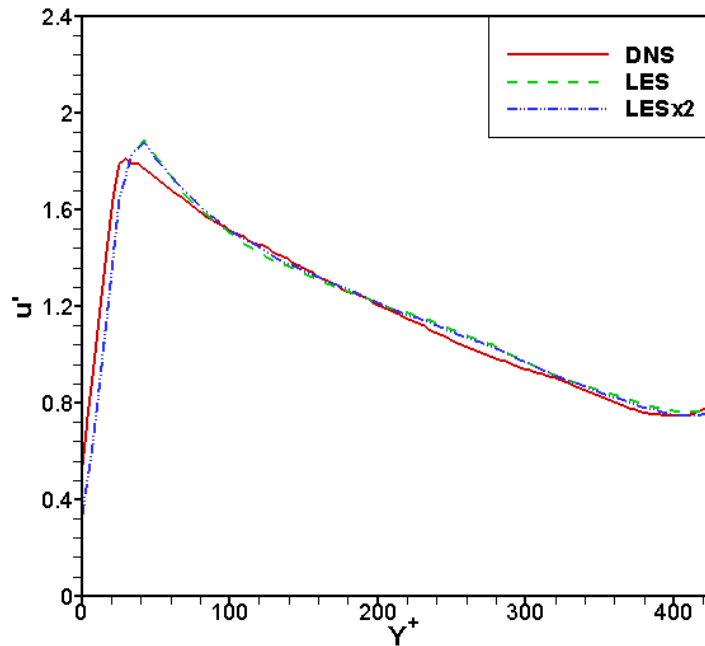
Figure 2.9:   Fluctuation of streamwise velocity
(u' is normalized by u_τ and Y^+ is normalized by d).
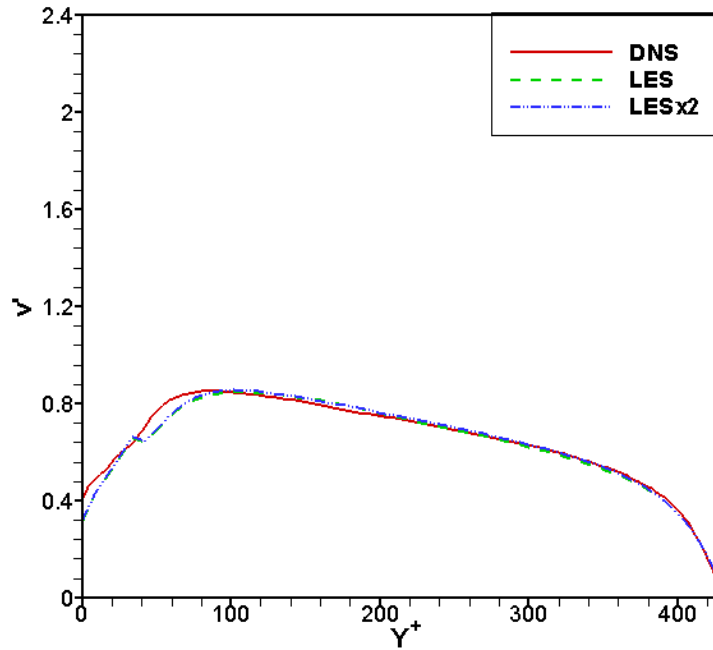
Figure 2.10: Fluctuation of vertical velocity
(*v'* is normalized by u_τ and Y^+ is normalized by *d*).
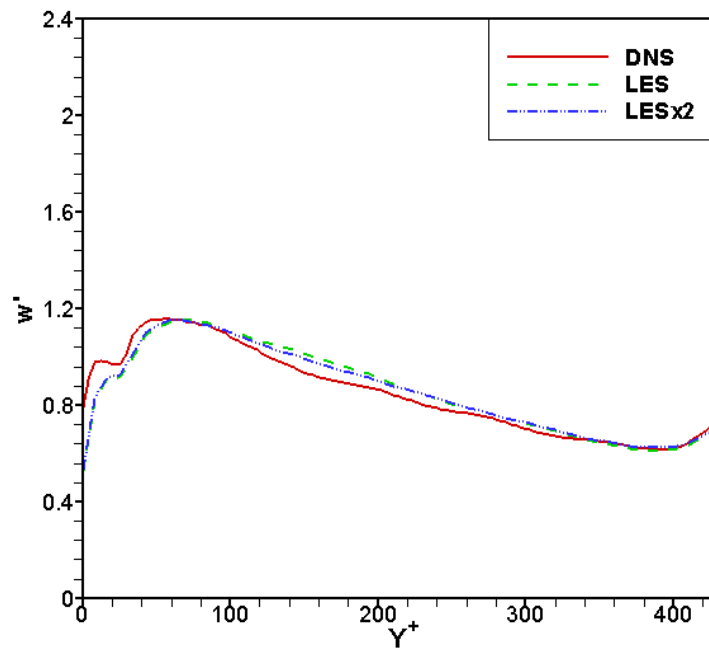
Figure 2.11: Fluctuation of spanwise velocity
(*w'* is normalized by u_τ and Y^+ is normalized by *d*).
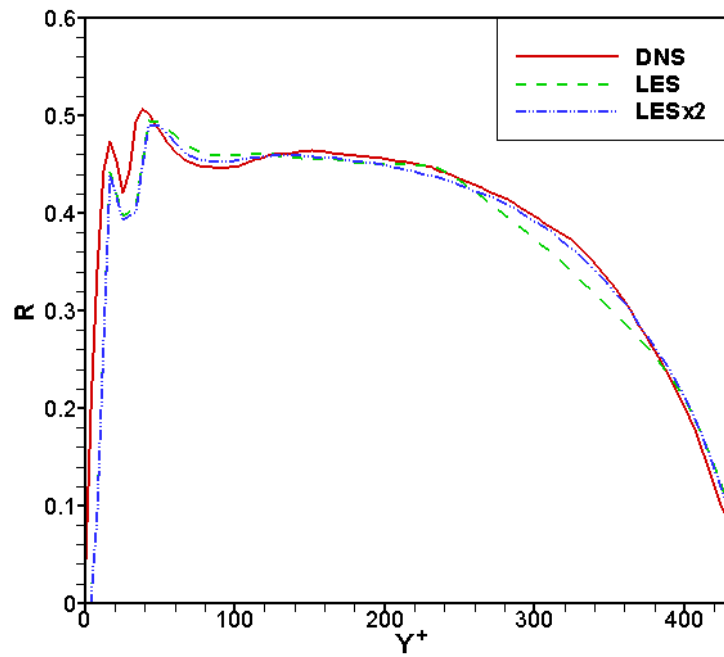
Figure 2.12:   Correlation of Reynolds Stress
(Y^+ is normalized by d).
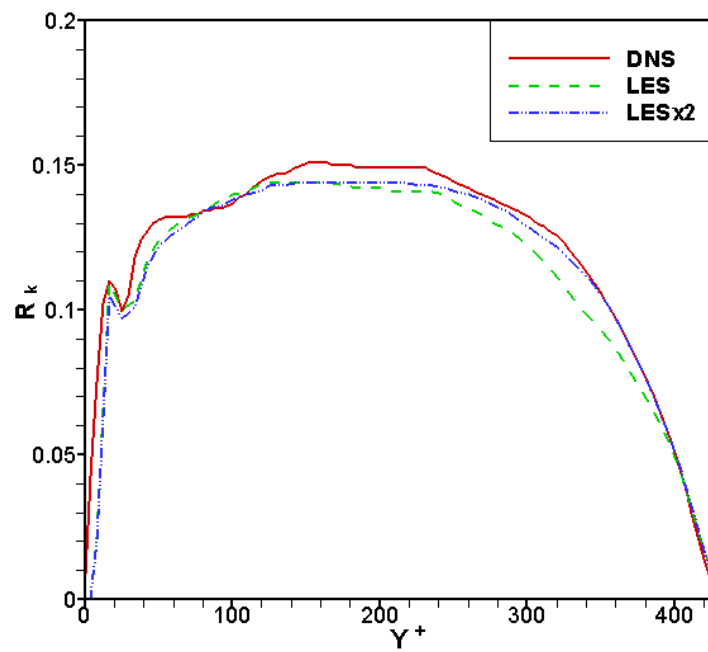
Figure 2.13:   Correlation of RS to TKE
(Y^+ is normalized by d).

Chapter 3
Large-scale Coherent Structures

3.1 Literature Review

The dynamics of coherent structures in turbulent flows has been studied extensively over the past few decades. More recently, the nature of large-scale coherent structures was explored by different groups. The structures are mostly observed to be composed of hairpin vortex packets (Tomkins et al. 2003, Ganapathisubramani et al. 2003) and identified according to their velocities, length and time scales as younger packets, older packets and even older packets from upstream (Adrian et al. 2000) or primary, secondary, tertiary and downstream hairpin vortices (Zhou et al. 1999) as in Fig. 3.1: PHV denotes primary hairpin vortex, SHV denotes secondary hairpin vortex, THV denotes tertiary hairpin vortex, DHV represents downstream hairpin vortex, QSV represents quasi-streamwise vortices. The small vortices increase and connect with each other with the distance away from the wall and develop into much larger structures (Zhou et al. 1999).

The length of the large structures has been shown to be approximately two to three times flow depth and their width to be of one-order of magnitude smaller in the turbulent boundary layer flow (Ganapathisubramani et al., 2003; Adrian et al., 2000) and channel flow (DEL Alamo et al. 2006, Hurther et al. 2007). In pipe flow, the wavelength of very large scale

motion, aligned by large scale packets, can be more than 8~16 pipe radii (Kim and Adrian, 1999; Guala et al., 2006). Moreover, these large coherent structures are demonstrated to contribute substantially to Reynolds Stress (Guala et al. 2006; Ganapathisubramani et al., 2003), mean shear and Turbulent Kinetic Energy (Hurther et al. 2007) and have been shown to have Reynolds number similarity (Guala et al. 2006).
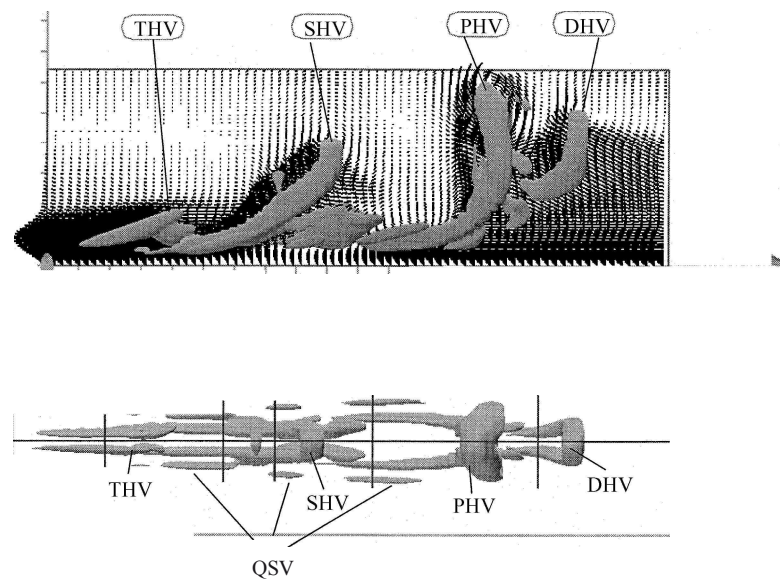
Figure 3.1: Organization of hairpin vortex packet in the streamwise direction (Zhou et al., 1999).

The packets are mainly in the logarithmic region, although they may possibly grow into the outer region (Guala et al., 2006). The formation of very large-scale structures is based on the continuous mechanism of self-production, i.e. young vortices are produced by the older ones. The formation of the long structures is easily disturbed and thus the effect of the top surface can possibly prevent the generation of very long structures

in field experiments.

In the experimental study of Praturi et al. (1978), which was performed using a stereoscopic medium-speed camera system, the spanwise vortices were the dominant features in the outer region of the turbulent boundary flow. These vortices were shown to transport large amount of fluid from the irrotational region into the outer region and thus, caused the variation of the outer edge of the boundary layer. The life time of the near-wall quasi-streamwise vortices was shorter than the spanwise vortices in the outer region. They conclude that the near-wall bursts originated from these vortices, rather than caused the bulges as suggested by Kim (1971) and, the quasi-streamwise vortices were produced from the interaction of high-speed and low-speed fluid, instead of producing the interaction as in a number of models.

Head and Bandyopadhyay (1981) reported the effect of Reynolds number, ranging from 500 to 17,500, on the hairpin vortices in a turbulent boundary layer. The inclination angle of hairpin vortices is approximate 45^0, though it might be smaller in higher Reynolds number cases. The length of the structures seems to be determined by the thickness of the boundary layer. In the low Reynolds number conditions, the structures were relatively stable and the large and small structures could be identified clearly. In the high Reynolds number conditions, the large structures were elongated and composed of a group of hairpins of different length scales. Their investigation presented a clear picture of the difference between the large structures at a range of Reynolds numbers and again indicated that

the large-scale structures were a significant feature of the boundary layer flow.

Moin and Kim (1985) investigated the hairpin vortices using large-eddy simulation data of turbulent channel flow. The hairpin structures were shown to originate from the spanwise vorticity sheets. Their velocity and vorticity fluctuation correlations suggested that the maximum inclination angle of the vortices was 45^0. In the second part of the analysis, Kim and Moin (1986), a couple of vortical structures were related to ejections and sweeps respectively. The structures were shown to contribute to Reynolds Stress and turbulent energy substantially.

Kaftori (1994) studied the turbulent boundary layer by laser Doppler anemometry. Their results suggested that the large streamwise vortices, like an expanding spiral, were the dominant structures in the wall region and could extend to the outer region. They also concluded that the quasi-streamwise vortices, ejections and sweeps were part of the funnel-shape vortices, which moved quickly in the low-speed background fluid and generated streaks.

Hussain (1983) reviewed the preceding observations regarding the large-scale coherent structures in turbulent flows. He defined the coherent structures as the connective fluid mass with a phase-correlated vorticity spatially, explained the formation of the structures and addressed the eduction methods. By comparing the coherent and average Reynolds Stress, he emphasized the importance of incoherent turbulence.

Grass et al. (1991) were probably the first who experimentally presented that the hairpin vortices dominated the dynamic process of the flow in rough wall conditions. It was shown that length-scale of the structures increased along with wall distance and was influenced by the roughness size. The bursting events were clearly shown to be associated with the hairpin vortices. His results agreed with Townsend's (1976) 'attached-eddy' hypothesis.

Haidari and Smith (1994) reported the evolution of single hairpin vortices produced by fluid injections. Both dye and hydrogen-bubble visualization were employed for flow visualization, along with hot-film anemometry. Two different kinds of hairpin vortices were observed due to different Reynolds number and injection parameters: one was decaying gradually; the other was growing and carrying the whole flow to develop. The new vortices could be created by the old ones in two ways: one was lateral spreading of subsidiary hairpin vortices on both sides of a primary vortex; the other was local separation of secondary hairpin vortices in the upstream region of the primary vortex. The low momentum streaks were created by the hairpin legs and the bursting events were produced during the formation process of the hairpin vortices.

Falco (1991) proposed a coherent structure model of the turbulent boundary layer flow based on their experimental data. The wall region flow structures were composed of streaks, hairpin vortices and the pockets related to the formation of the hairpin vortices. The outer region was characterized by large eddies and large-scale motions. The interaction

between the two regions generated bursting events and contributed significantly to Reynolds stress. This model incorporated most of the features of the turbulent boundary flow as observed in the preceding works.

Another model was proposed by Smith et al. (1991) who described the hairpin vortices as the essential structure in the turbulent boundary layer flow. The evolution of hairpin vortices was characterized by two processes. In the first process, the initial hairpin vortices were originated from small regions of vorticity due to the viscous-inviscid interactions and stimulated subsidiary vortices thereafter. The head of the hairpin grew in the spanwise direction as it rose away from the wall whereas the distance between the hairpin legs decreased in the near-wall region. Whenever the hairpin vortices were formed, the dynamic process of aggregation stopped and break-up between the vortices occurred. In the second process, low speed fluid with high vorticity was ejected, which finally evolved into secondary hairpin vortices. This process was determined by the location of the primary vortices and frequently occurred near the hairpin legs. Their model emphasized the asymmetry of most of the hairpin vortices in turbulent boundary layer, though the secondary hairpins appeared symmetrically.

In the structure model (Fig.3.2) proposed by Adrian et al. (2000), the hairpin packets originated from the wall due to some kind of disturbance, then intensified into an omega-shape structure, and might also induce a secondary hairpin if the primary structure was strong enough. The hairpin

vortex was basically asymmetric and was also associated with the bulges in the outer region. The angle of the vortex head ranged from 15° to 75°, as a function of the distance from the wall. One important feature was that the structures could break down and reconnect as indicated from their simulation data.
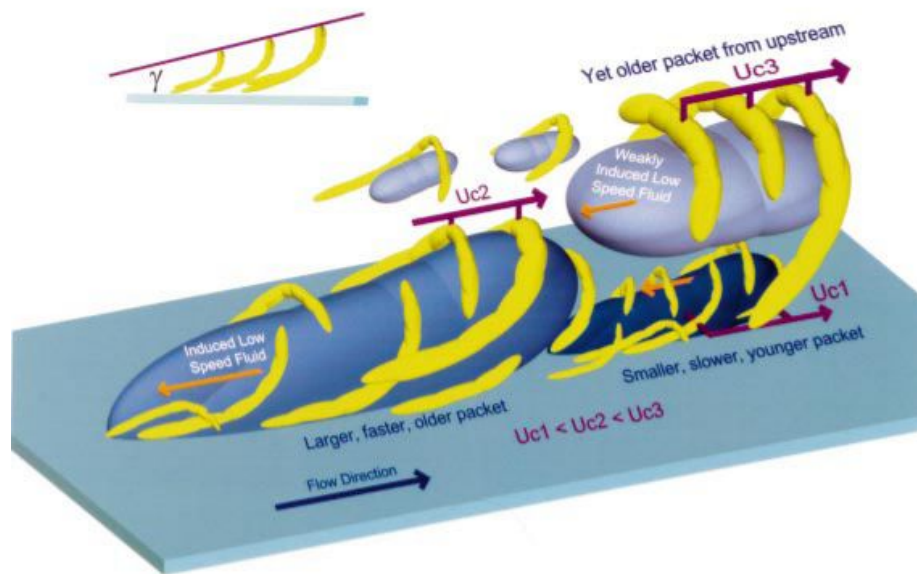
Figure 3.2: Model of hairpin vortex packets and the corresponding local uniform momentum, U_{c1}, U_{c2} and U_{c3} are convection velocities of the packets in the streamwise direction (Adrian et al., 2000).

Tomkins and Adrian (2003) revealed the spanwise growth mechanism of the hairpin structures (Fig.3.3). In their model the spanwise structure grew self-similarly in a general sense, although not strictly, from the evidence of a linear increase of the spanwise length away from the wall. This concept does help to explain the merging of the streaks although it does not support the growth of a very long low-speed region. The hairpin packets were

organized along the streamwise direction in the logarithmic region, characterised by the large-scale momentum deficit. The packet merging evidence was the stagnation point together with the spanwise distribution of two low momentum regions with a high momentum region in the middle.(Fig.3.4)
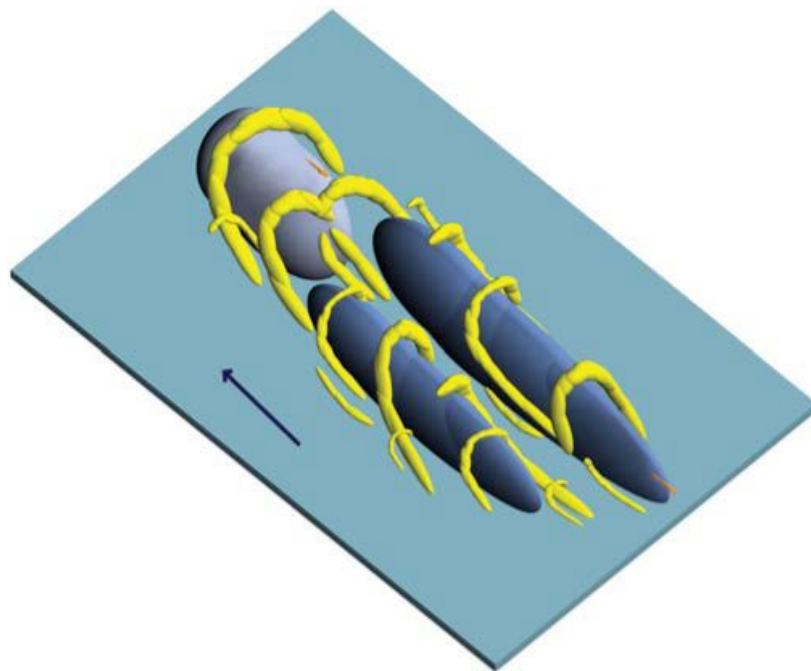
Figure 3.3: Merging mechanism of the hairpin vortices
(Tomkins and Adrian, 2003).

In the experimental study of Liu et al. (2001), the large-scale motion with length scale larger than $3.2h$ contained half of the turbulent kinetic energy and also more than two thirds of the Reynolds Stress. They suggested the streamwise length scale in channel flow could be as long as the pipe flows. Zhou et al. (1999) investigated the evolution of a single hairpin in the

channel flow by DNS. The hairpin vortex evolves into an omega shaped vortex and produces secondary, tertiary and downstream vortices. Quasi-streamwise vortices on the sides of the vortex structure are also observed. (Fig.3.1) The generation only occurred when the primary hairpin vortex was strong enough. It took less time for the stronger hairpin to produce new ones. The tilt angle of the hairpins varied from 8^0 to 75^0. This auto-generation mechanism reasonably explains the formation of the hairpin packets and should be applied to channel flow with different bed roughness and Reynolds number.
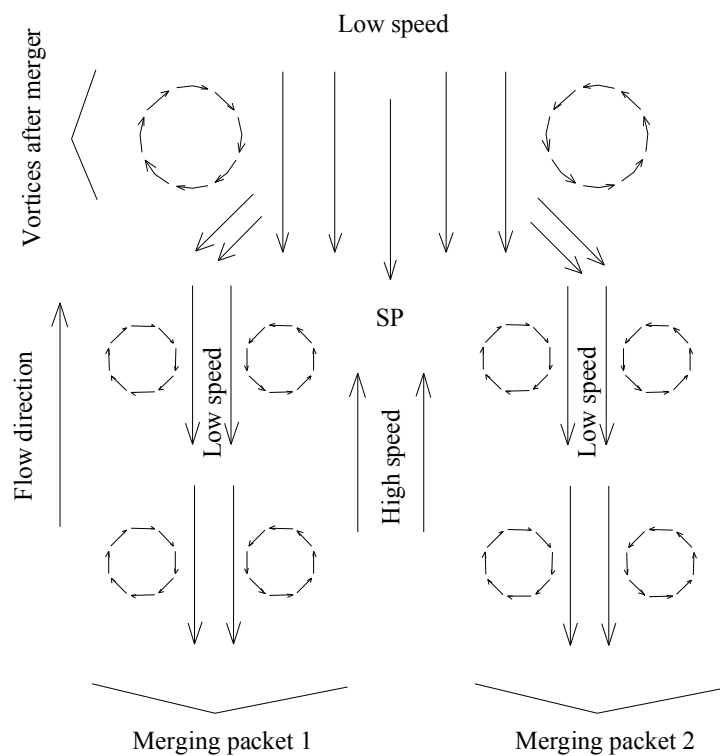
Figure 3.4: Merging signature of the vortex packets (Tomkins and Adrian, 2003).

In the numerical study of DEL Alemo et.al (2006), two kinds of clusters were observed: one was small vortex packets detached from the wall; the other was tall clusters attached to the wall. The low streamwise velocity motion was considered to be the wakes of the clusters and the clusters on the other hand, were produced by the wakes. This dynamic process offered another model for the structure organization in the turbulent flow.
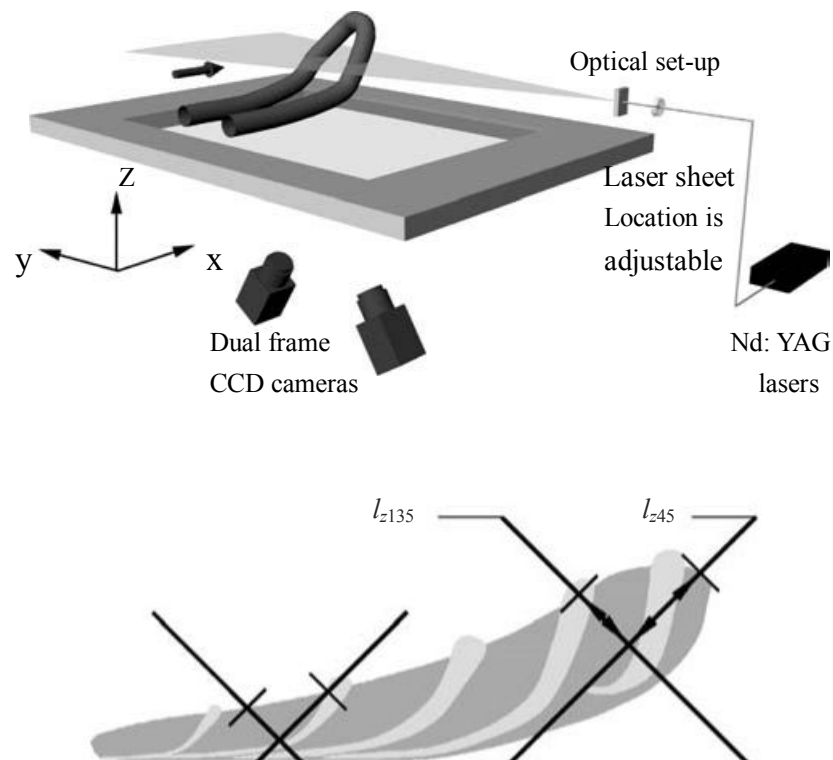
Figure 3.5: Stereoscopic PIV measurements of the hairpin vortex packet in a wind channel (Ganapathisubramani et al., 2005).

Ganapathisubramani et al. (2005) experimentally investigated the large-scale coherent structures in a wind tunnel (Fig.3.5). The two-point correlation analysis indicated that the length of the long uniform low momentum region increased in the log region and decreased in the wake region whereas the width kept increasing over the whole boundary but with different growth rate. The correlation of streamwise velocities in the 45^0 inclination was larger than in the 135^0 inclination, in accordance with the tilt of the hairpin packet head. The correlation of a near-wall reference point was small compared with far away. This implied that the hairpin packets did not greatly influence the turbulence of the very near wall region.

The interaction between the large structures and near-wall structures in a turbulent channel flow was examined by Toh and Itano (2005) using DNS. They revealed that the large-scale structures and near-wall structures were generated in a dynamic cycle. That is, the large-scale structures were generated by the aggregation of the near-wall structures and the near-wall structures could be formulated due to the growth of the large-scale ones. Although their computational domain was really small, they captured the large structures successfully. The domain restriction might have artificial influence on the interaction between the large and small structures, but the dynamic process was probably realistic.

Balakumar and Adrian (2007) compared the contributions from large-scale and very large-scale structures and noted a Reynolds number effect. When the Reynolds number increases, the very large-scale structures contain

more energy than the large-scale structures. For both channel and boundary layer flows, more than 45% of the streamwise kinetic energy and 40% of the Reynolds Stress are contributed from the large structures longer than $3h$. These fractions can be even larger in pipe flows as they pointed out. Similar results were obtained in the simulation by Jimenez et al. (2004). The large structures contained 46% of the total Reynolds Stress and 44% of the total kinetic energy. They also confirmed the significant contribution to streamwise kinetic energy as 51%, but comparatively less contribution to vertical kinetic energy as 20%.

The preceding results indicate that the large-scale coherent structures appear as a group of vortices (Kaftori 1994, Adrian et al. 2000), which can generate new vortices (Haidari and Smith 1994, Zhou et al. 1999) around them. The near-wall bursts (Grass et al. 1991, Falco 1991) are closely associated with the large structures. The organization of the structures is dynamic as the packets can break up and regenerate (Smith et al. 1991, Adrian et al. 2000). The length scale of the structures are shown to be influenced by the Reynolds number (Head and Bandyopadhyay 1981, Balakumar and Adrian 2007) and bed roughness (Grass et al. 1991). However, the maximum length remains an open question. The relationship between the organization of large structures and roughness element, e.g. roughness height, packing density, is still not clear.

In this work, the organization of large coherent structures in the open-channel flow is studied and compared with boundary layer flows (Adrian et al 2000, Tomkins and Adrian 2003). The variations of Reynolds

Stress and Turbulent Kinetic Energy due to the large structures are analysed as they contribute significantly to the whole flow field, around 50% according to the previous results (Balakumar and Adrian 2007, Jimenez et al. 2004). The length scale will be discussed separately in the next chapter.

3.2   Large Coherent Structures

The Q-criterion (Hunt et al. 1988), $Q = \frac{1}{2}(\|\Omega\|^2 - \|S\|^2)$, is employed to identify the vortices, i.e. the second invariant Q of ∇v is positive. Here S and Ω are the symmetric and anti-symmetric components of ∇v: $S = \frac{1}{2}(\nabla v + (\nabla v)^t)$ and $\Omega = \frac{1}{2}(\nabla v - (\nabla v)^t)$. As shown in Fig.3.6 and Fig.3.7, both of the instantaneous data contain three parallel large-scale structures. The experimental work of Roy et al. (2004) stated that the length of the large motions was 3 to 5 times flow depth and the width was 0.5 to 1 times flow depth in a gravel-bed river. The length of the structure is hard to estimate from the data in the present work as the computational box is not big enough to tell how long exactly the structures are. But it is simply larger than about 10 times the effective flow depth. The width is roughly the same as their experimental result. The structures are meandering and adjacent, which makes the identification of the structures from each other difficult. As observed by many other researchers (Robinson, 1991; Zhou et al, 1999), the asymmetric hairpin vortices with one leg are more frequently generated than the symmetric hairpin vortices. As a consequence, the long structures are mainly composed of quasi-streamwise vortices and asymmetric hairpin vortices with single leg.

The cross-correlation of the vorticity components and Q show the orientation of the vortices (Fig.3.8~Fig.3.10). The correlation between $|\omega_z|$ and Q, $\overline{|\omega_z|Q}\big/\left(\sqrt{\overline{|\omega_z|^2}}\sqrt{\overline{Q^2}}\right)$, increases sharply above the top of roughness elements due to the increasing amount of archlike vortices.

Corrrespondingly, the correlation between $|\omega_x|$ and Q, $\overline{|\omega_x|Q}\Big/\left(\sqrt{\overline{|\omega_x|^2}}\sqrt{\overline{Q^2}}\right)$,

decreases whilst the correlation of $|\omega_y|$ and Q, $\overline{|\omega_y|Q}\Big/\left(\sqrt{\overline{|\omega_y|^2}}\sqrt{\overline{Q^2}}\right)$, keeps

constant roughly. The kind of distribution agrees with the model of turbulent boundary layer flow proposed by Robinson (1991) as in Fig.3.11.

All of the correlations are positive, which implies that the vorticities are generally associated with the vortices. The correlation between $|\omega_x|$ and Q is primarily larger than the correlation between $|\omega_z|$ and Q. Therefore, the vortices are mainly aligned in the streamwise direction. The peak below the top of roughness in Fig.3.8 is created by the small vortices trapped among the spheres. The correlations tend to be zero near the top surface where the vortices disappear.

Tomkins and Adrian (2003) reported that the structures also exhibit spanwise growth away from the wall, that is, the structures are more elongated in the near-wall region than those far away. The haipin vortex packet signature is described as a low streamwise momentum region between two counter-rotating vortices, with a stagnation point due to the encounter of low-speed fluid with the high-speed fluid upstream. Such stagnation point may disappear if there is a vortex upstream which replaces the high-speed fluid. In their velocity vector plot, the vortices rotating in the counter-clockwise direction mainly exist on the right side of the streaks and the vortices in the clockwise direction appear on the other side (Fig.3.4). Such a combination causes a low momentum region

between the vortices. The merging of the vortex packets in the spanwise direction is characterized by a region of high momentum in the middle of two areas of low momentum, with a stagnation point downstream of the high momentum. The merging of the vortex packets frequently occurs between $20 < y^+ < 100$; but it is reduced above this region, possibly due to the larger distance between the structures. They described such merging as a "fork". However, the head of the "fork" can be either upstream or downstream of the structure. They interpreted it as coalescence in both directions or one is merging and the other is separating.

Fig.3.12 and Fig.3.13 indicate the growth of the structures along the depth of flow (Ma and Williams, 2009b). The high speed and low speed regions grow with the wall distance. The signature of the structure is the local maximum of streamwise velocity. This implies that the organization of the coherent structures is different from the hairpin vortex model proposed by Tomkins and Adrian (2003). In their model, the hairpin vortices are connected in the streamwise direction and the signature is the local minimum of streamwise velocity. They also observed stagnation points due to the local low momentum. But in this study, such stagnation point are not observed as almost all of the hairpin vortices are asymmetric. Fig.3.14 shows that the high velocity region originates from the counter-rotating vortex pairs. The dashed lines indicate the high velocity region corresponding to the streamwise velocity contour in Fig.3.13, with vortex pairs on both sides of the region. The rotating direction of the vortices is different from the hairpin packets model.

As shown in Fig.3.15, the left counter-rotating vortex pairs, which can increase the local streamwise velocities, tend to aggregate together to form the large-scale coherent structures as observed here; whilst the right vortex pairs, which decreases the local streamwise velocities, are easily separated by the main stream, unless they are strong enough to suffer the shear stress. Only the strong symmetric hairpin vortices themselves can produce the local low momentum region between the vortex legs.

Adrian et al. (2000) reported that the vortex packets were composed of a group of vortices with similar convection velocities and the inclination angle increased along with the distance from the wall. The packets transported downstream at different velocities and the organization of the vortices could keep stable for a long time; even individual vortices dispersed with a small velocity. The packets contained more than 10 hairpin vortices and the length could be two times the boundary layer thickness. In their conceptual model, the large vortices grew from small vortices and finally broke down into small vortices again. They proposed that the packets might be broken and become reconnected in the outer region of the boundary layer.

Fig.3.16-Fig.3.18 shows the organization of the structures: small and short quasi-streamwise vortices at the bottom whilst larger and longer quasi-streamwise vortices and asymmetric hairpin vortices far away from the wall. This is consistent with the observation of Tomkins and Adrian (2003) as the vortex core increases away from the wall. Consequently, the large distance between the vortices and also between the structures

explains the growth of the high-speed and low-speed streaks well.

Fig.3.19 and Fig.3.20 depicts the uniform streamwise momentum region retarded by the large structures, as observed by Adrian et al. (2000) and Hurther et al. (2007). The continuous region is well organized on top of the roughness elements. The circles in the figure denote the head of the hairpin vortices, with tilt angles range from 10^0 to 60^0 approximately, in agreement with the results of Adrian et al. (2000).
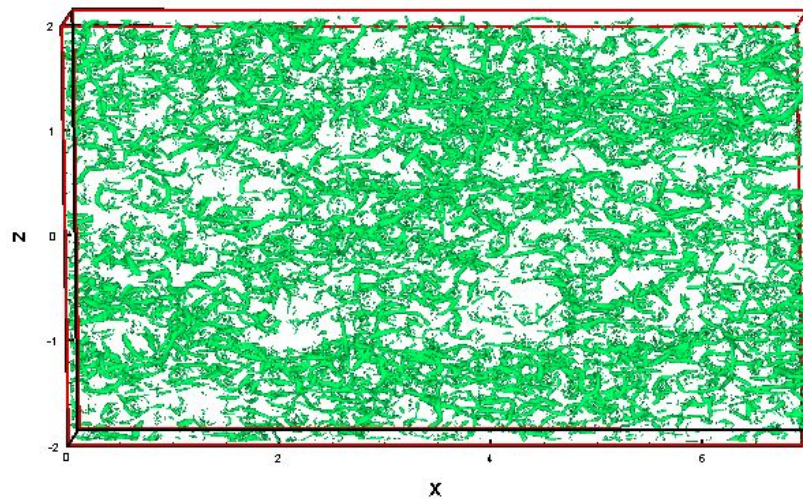
Figure 3.6: Instantaneous large-scale coherent structures visualized by Q-approach: $Q = 0.0098\ Q_{max.}$
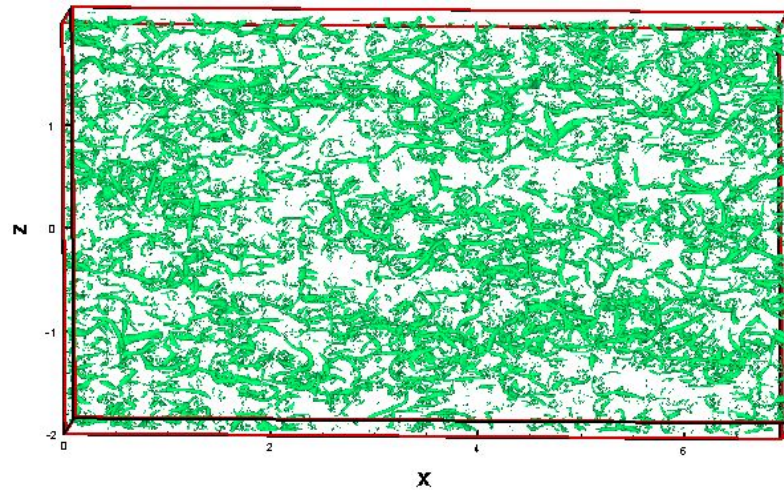
Figure 3.7: Instantaneous large-scale coherent structures visualized by *Q*-approach: $Q = 0.0149 \, Q_{max.}$
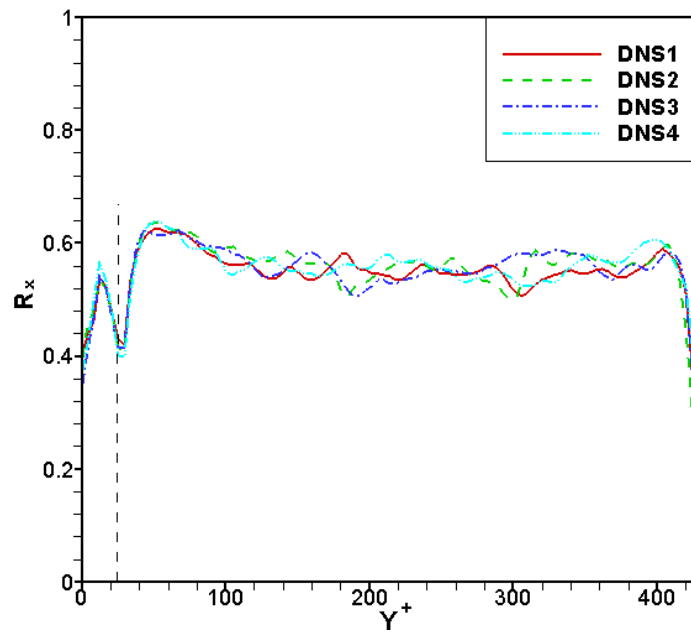
Figure 3.8: Cross-correlation of $|\omega_x|$ and Q
(Y^+ is normalized by d, dashed line denotes top of roughness).
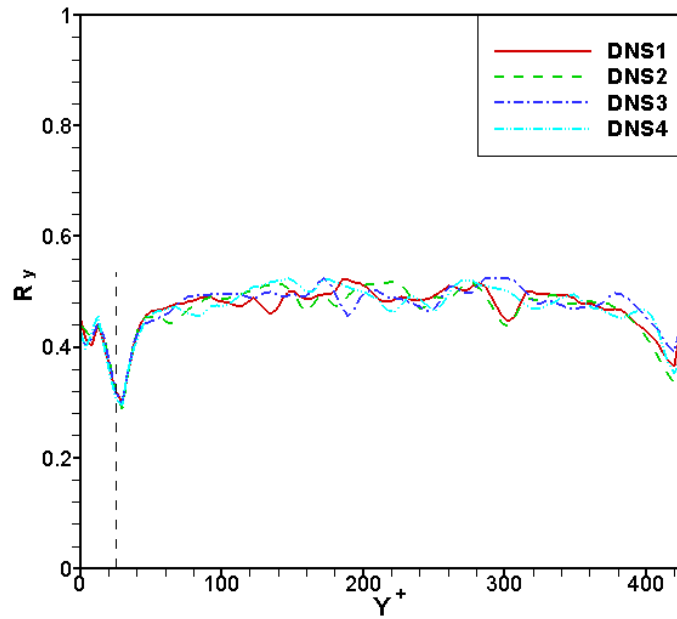
Figure 3.9: Cross-correlation of $\left|\omega_y\right|$ and Q
(Y^+ is normalized by d, dashed line denotes top of roughness).
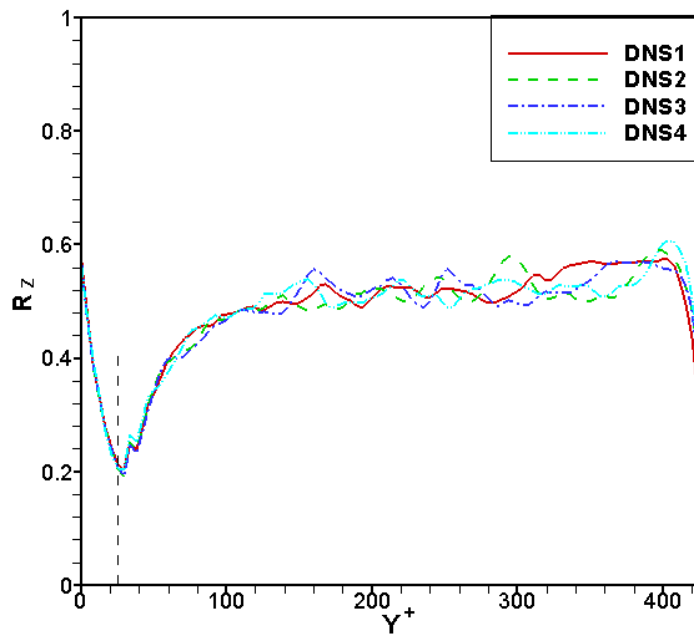
Figure 3.10: Cross-correlation of $\left|\omega_z\right|$ and Q
(Y^+ is normalized by d, dashed line denotes top of roughness).
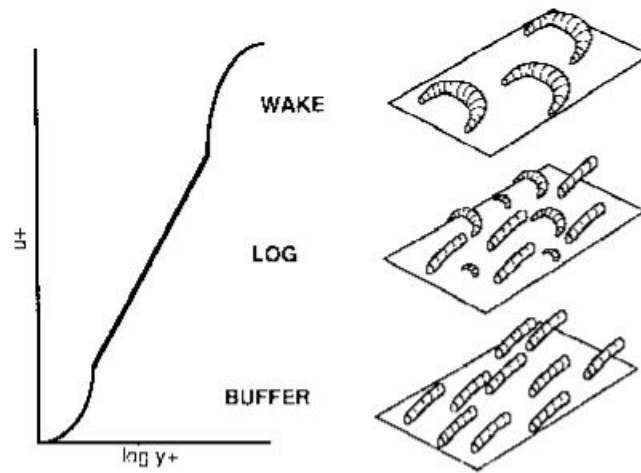
Figure 3.11: Ideal distribution of the vortices in different regions of the turbulent boundary layer flow (Robinson, 1991).
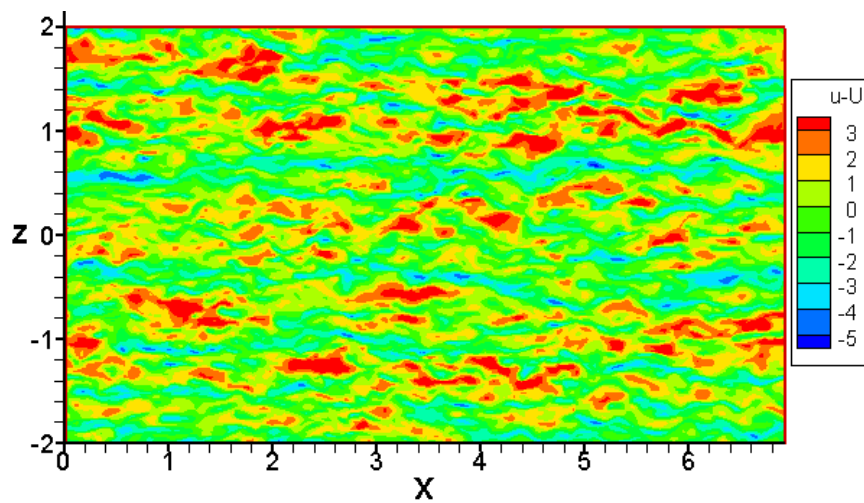
Figure 3.12: Contour of streamwise velocity fluctuation at $y = 0.28d$ (X and Z are normalized by d).
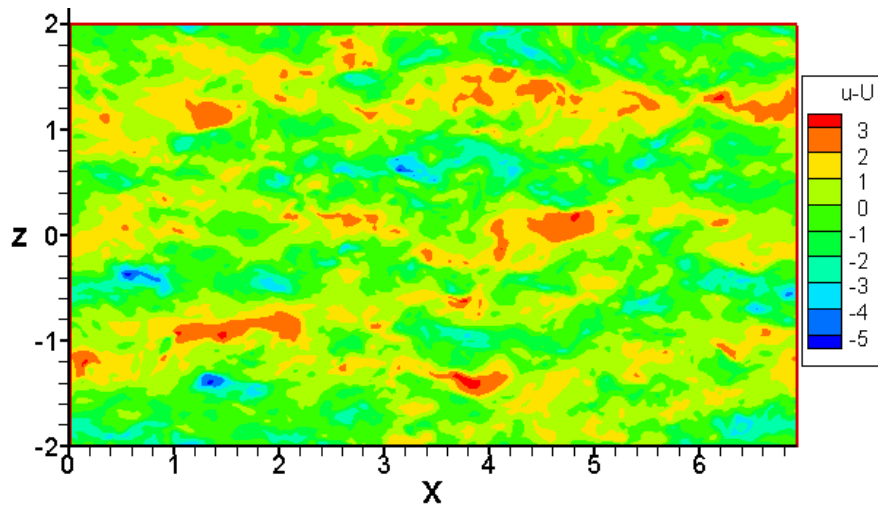
Figure 3.13: Contour of streamwise velocity fluctuation at $y = 0.56d$
(X and Z are normalized by d).
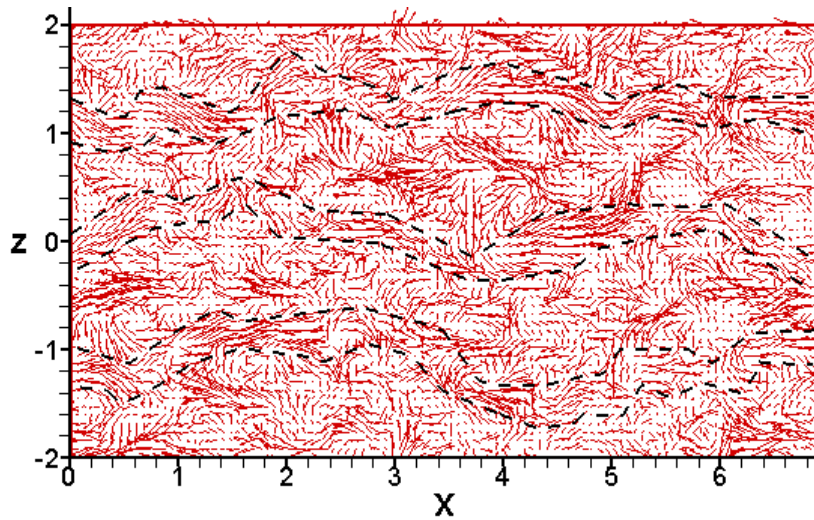
Figure 3.14:   Horizontal velocity vector plot at $y = 0.56d$
(X and Z are normalized by d, dashed lines denote meandering local
maximum momentum created by the large-scale coherent structures).

(*a*)   (*b*)
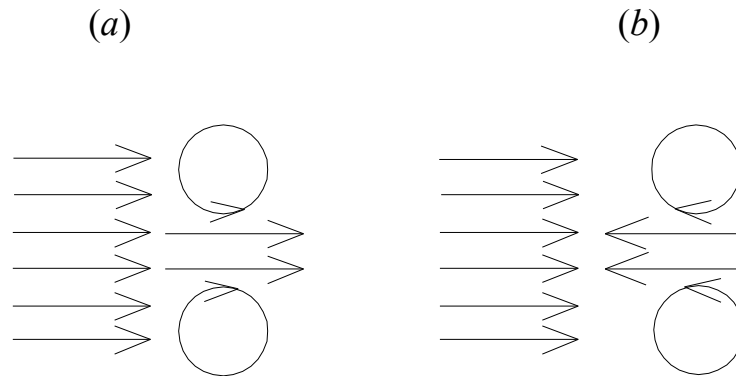
Figure 3.15: Different patterns of counter-rotating vortex pairs of large coherent structures. The former (*a*) creates local maximum momentum and the latter (*b*) produces local minimum momentum.
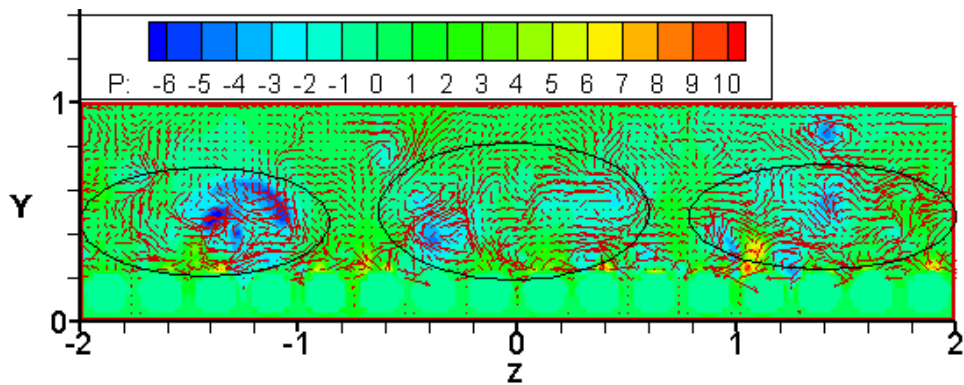
Figure 3.16: Spanwise velocity vector and pressure plot at *x* = 0.898 (*P* is normalized by ρu_τ^2, *Y* and *Z* are normalized by *d*, the circles denote three parallel large-scale coherent structures).
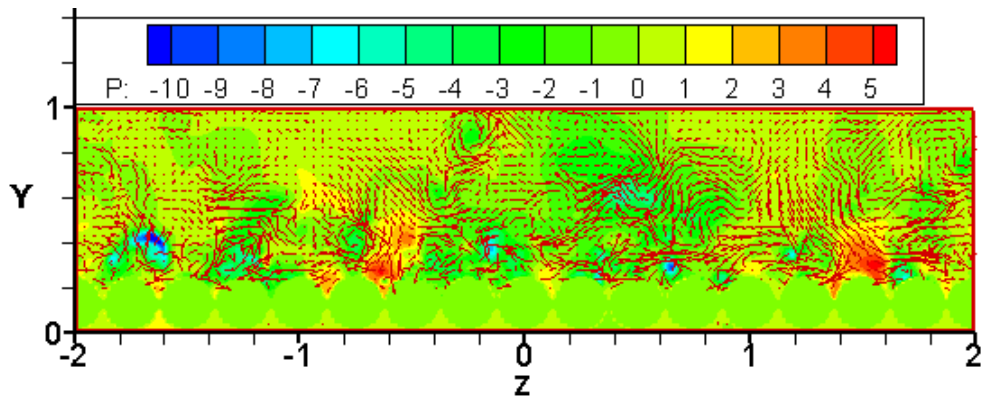
Figure 3.17: Spanwise velocity vector and pressure plot at $x = 0.498$
(P is normalized by ρu_τ^2, Y and Z are normalized by d).
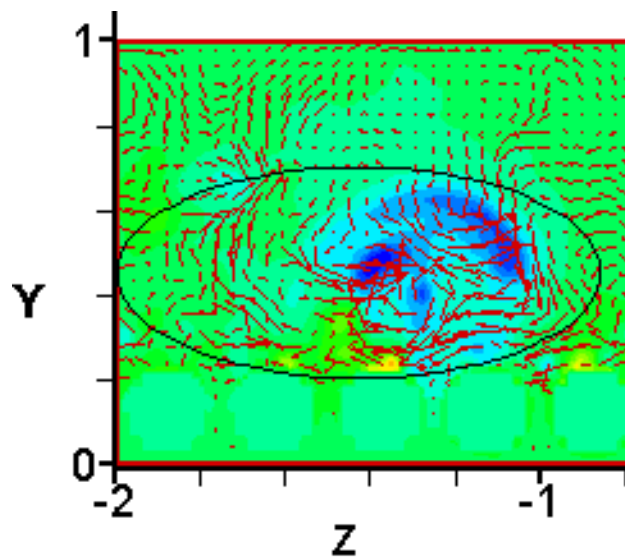
Figure 3.18: Spanwise organization of the vortex packet
(Y and Z are normalized by d).
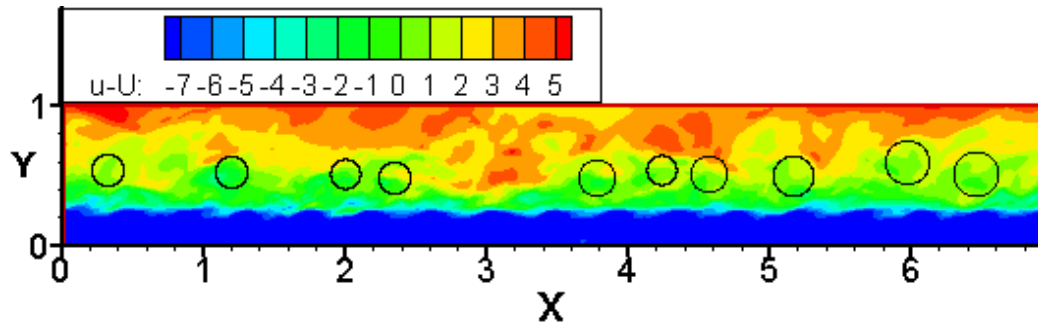
Figure 3.19: Uniform streamwise momentum at *z* = 1.992
(*u and U* are normalized by u_τ, *X* and *Y* are normalized by *d*, circles denote the heads of the vortices).
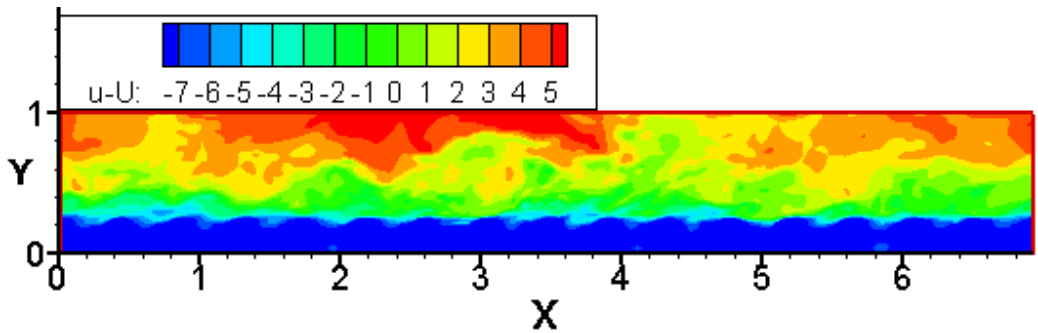
Figure 3.20: Uniform streamwise momentum at *z* = 0
(*u and U* are normalized by u_τ, *X* and *Y* are normalized by *d*).

3.3 Characteristics of Reynolds Stress and Turbulent Kinetic Energy

The channel is divided into three sub-regions as suggested in Nezu (1993): wall region [y/h < (0.15~0.2)], intermediate region [(0.15~0.2) $\leq$ y/h $\leq$ 0.6], and free-surface region (0.6< y/h $\leq$ 1.0). The wall region corresponds to the "Inner layer" of boundary layer flow whilst the intermediate and free-surface regions are outer layer. The effective flow depth originates from the effective bed level.

Liu et al. (2001) reported that the relative contributions from large-scale structures to Reynolds stress and Turbulent Kinetic Energy showed Reynolds number independence. The structures longer than 3.2h contribute more than two thirds of the Reynolds Stress and about half of the kinetic energy. However, the small structures are shown to contribute significantly to the vertical kinetic energy as the large structures contribute approximately 20% above 0.2h. Also, for the Reynolds Stress distribution, the small structures play an important role in the near-wall region as the large structures only contribute 13~26%.

Fig.3.21 shows the variation of the Reynolds Stress along the flow depth. DNS1~DNS4 represent four continuous LETOTs. As argued by Hutchins et al. (2007), the local instantaneous Reynolds Stress can be activated by the superstructures. The fluctuations of Reynolds Stress beneath the structures can be observed. The cumulative Reynolds Stress shows no fluctuations from the effective bed to top surface in Fig.3.22. This implies

the large structures actually not only influence the Reynolds Stress beneath them, also above them. In consequence, the ratio of contributions from different regions to the total remains the same. The large amplitude of Reynolds Stress fluctuation corresponds with the frequent bursting events.

Fig.3.23~Fig.3.25 indicate the variation of the contributions of fluctuating velocity components to the total Turbulent Kinetic Energy along with flow depth. More than 50% of the energy comes from u', whilst about 30% from w'. The u' contribution decreases from the top of spheres, all the way through the intermediate region, finally increases in the surface region. This corresponds with the uniform streamwise momentum retarded by the structures in Fig.3.19 and Fig.3.20. The v' contribution increases gradually from the wall region until the free surface, where the large structures disappear. This implies the large structures can activate the vertical fluctuating velocities, which is possibly due to the high-speed upwash and downwash fluid between the vortex pairs in Fig.3.18. The w' contribution remains stable in the intermediate region. The v' contribution tends to be zero near the top surface, whereas u' and w' contributions increase accordingly. The extreme activation of u', the peak around the top of roughness elements, makes both of v' and w' decrease.

Fig.3.26 indicates the variation of the Turbulent Kinetic Energy, though it is not as active as Reynolds Stress. Fig.3.27 shows the instantaneous cumulative TKE. These structures, which produce large TKE beneath them, also produce large TKE above them. Therefore, the amplification trend not only applies to RS, but also to TKE.

As reported by Guala et al. (2006), the large-scale motions contain more than 50% of the Reynolds Stress and 35% of the energy. the fractional contribution to the total Reynolds Stress and the total Turbulent Kinetic Energy are plotted according to Q value (Fig.3.28~Fig.3.31). For both Reynolds Stress and Turbulent Kinetic Energy, the contributions from the vortices, where $Q > 0$, are more than 50% of the total. In particular, the contributions from the small quasi-streamwise vortices near the bed, where $0 < Q < 500$ approximately, occupy a large part of the area.
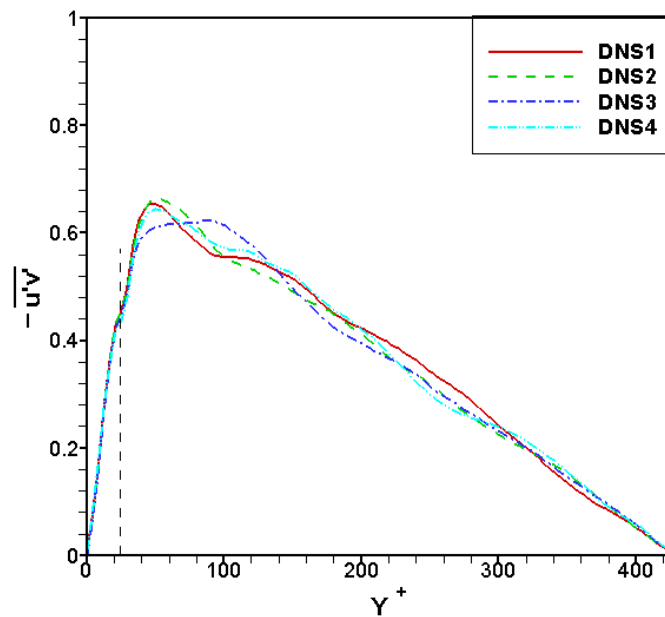
Figure 3.21: Instantaneous Reynolds Stress $-u'v'$
($-u'v'$ is normalized by u_τ^2, Y^+ is normalized by d, vertical dashed line denotes top of spheres).
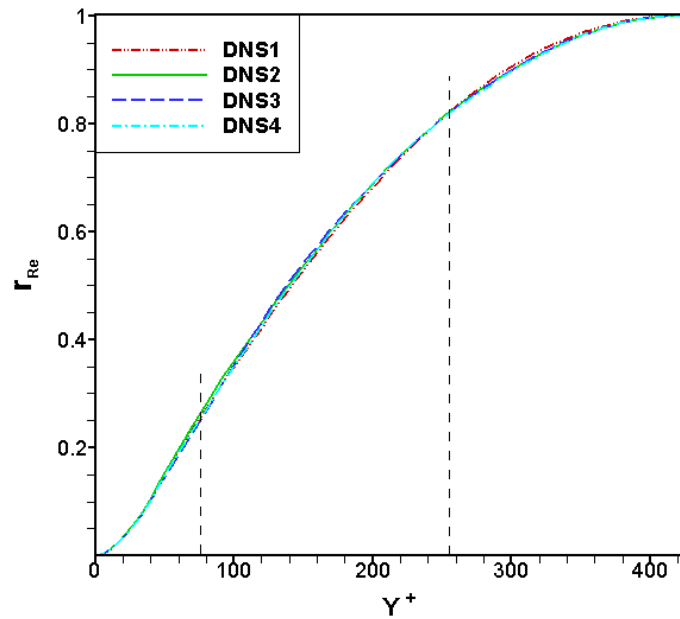
Figure 3.22: Instantaneous cumulative Reynolds Stress (Y^+ is normalized by d, vertical dashed lines denote three sub-regions of the channel).
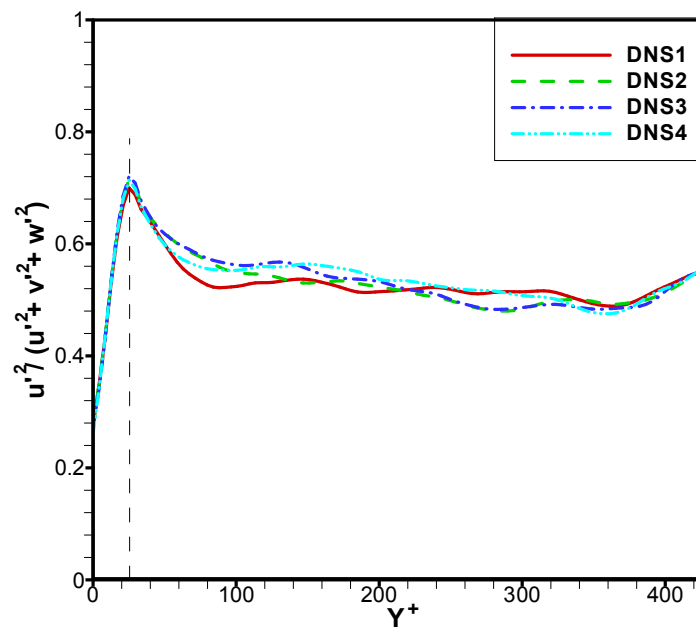
Figure 3.23: Contribution of u' to total Turbulent Kinetic Energy (Y^+ is normalized by d, vertical dashed line denotes top of spheres).
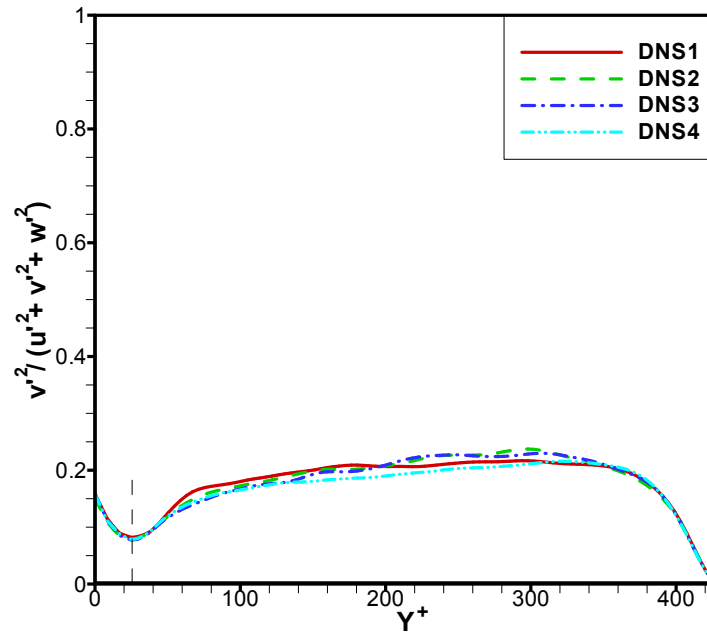
Figure 3.24: Contribution of *v'* to total Turbulent Kinetic Energy (Y^+ is normalized by *d,* vertical dashed line denotes top of spheres).
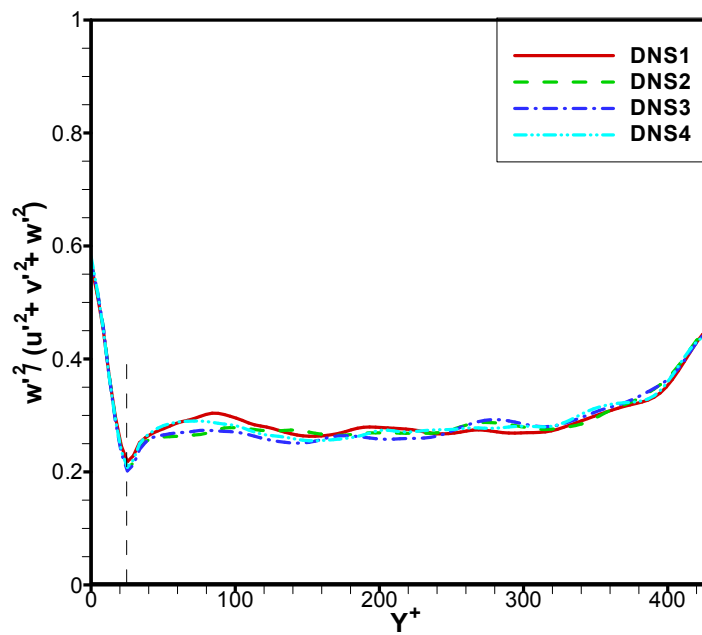
Figure 3.25: Contribution of *w'* to total Turbulent Kinetic Energy (Y^+ is normalized by *d,* vertical dashed line denotes top of spheres).
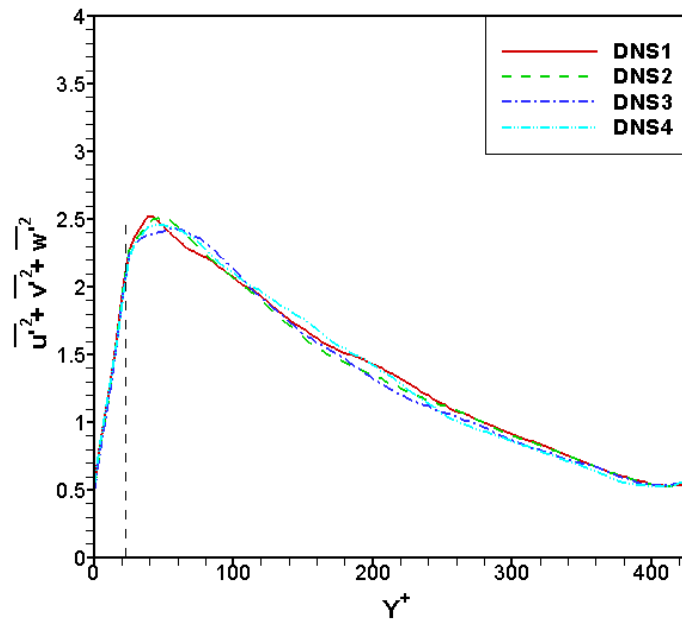
Figure 3.26: Instantaneous Turbulent Kinetic Energy
(TKE is normalized by u_τ, Y^+ is normalized by *d,* vertical dashed line
denotes top of spheres).
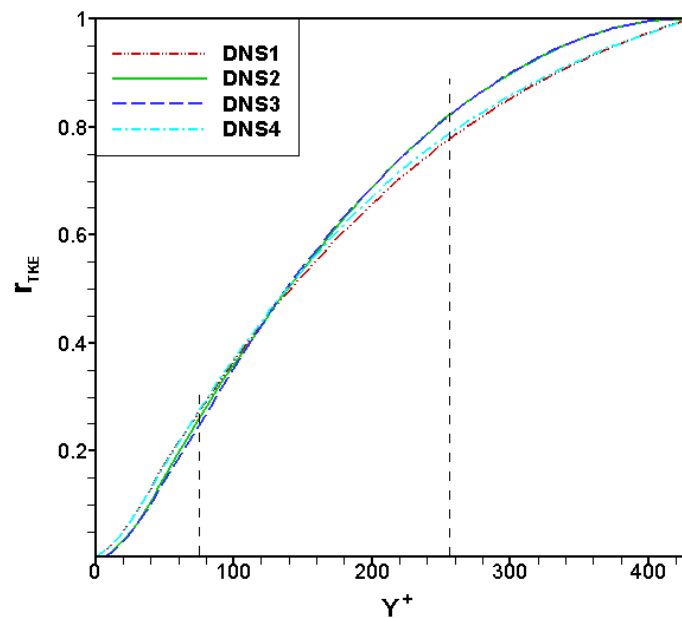
Figure 3.27: Instantaneous cumulative Turbulent Kinetic Energy
(Y^+ is normalized by *d,* vertical dashed lines denote three
sub-regions of the channel).
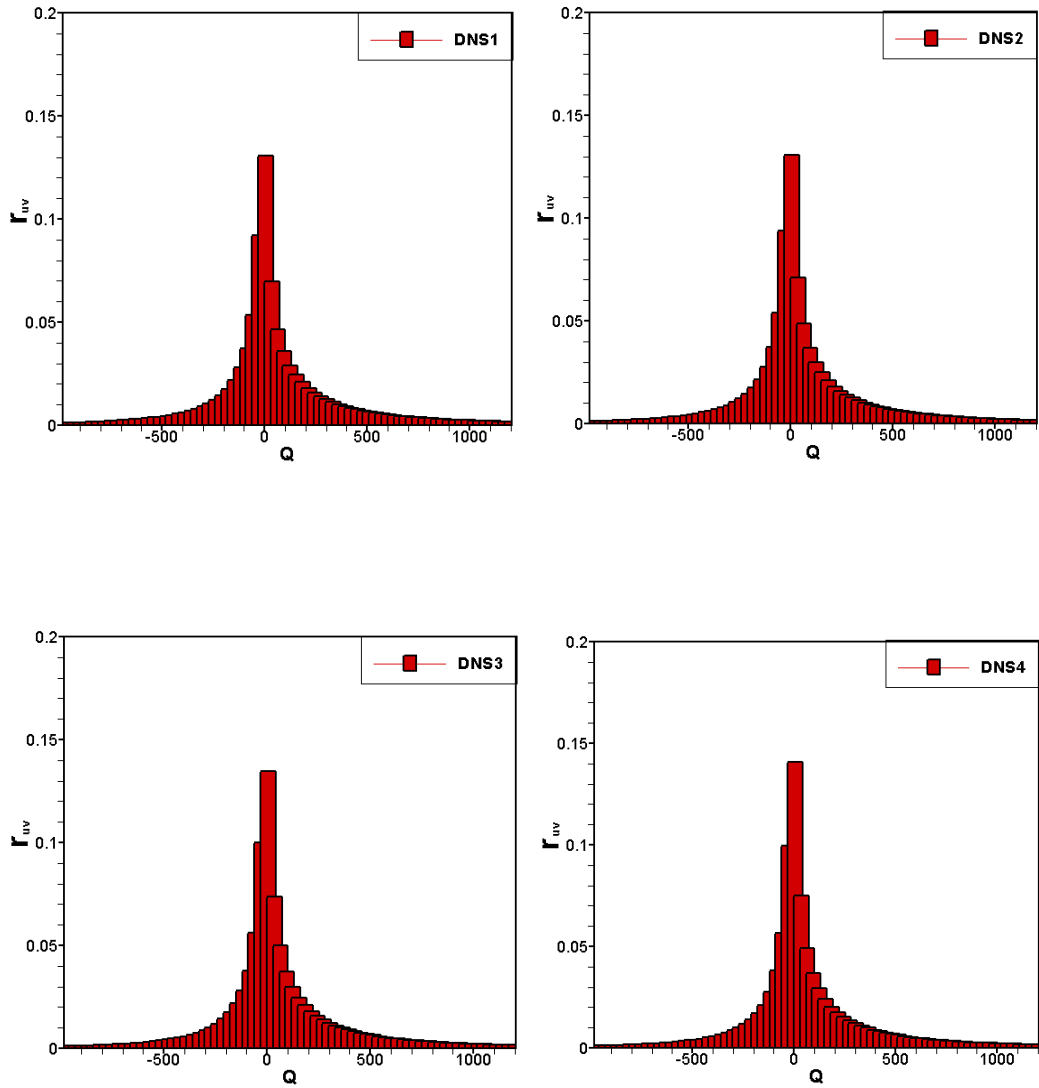
Figure 3.28: Instantaneous distribution of Reynolds Stress –*u'v'* according to *Q*.
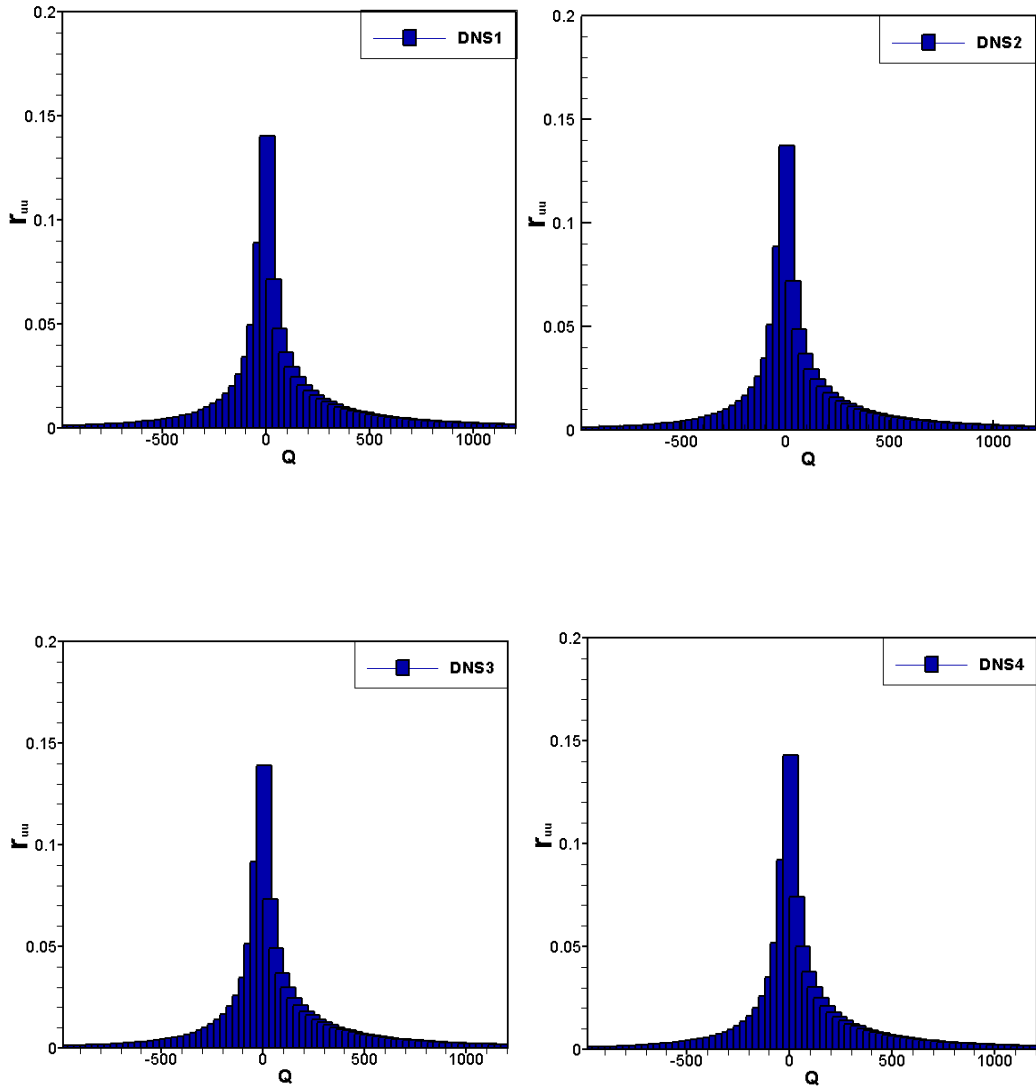
Figure 3.29: Instantaneous distribution of u'^2 according to Q
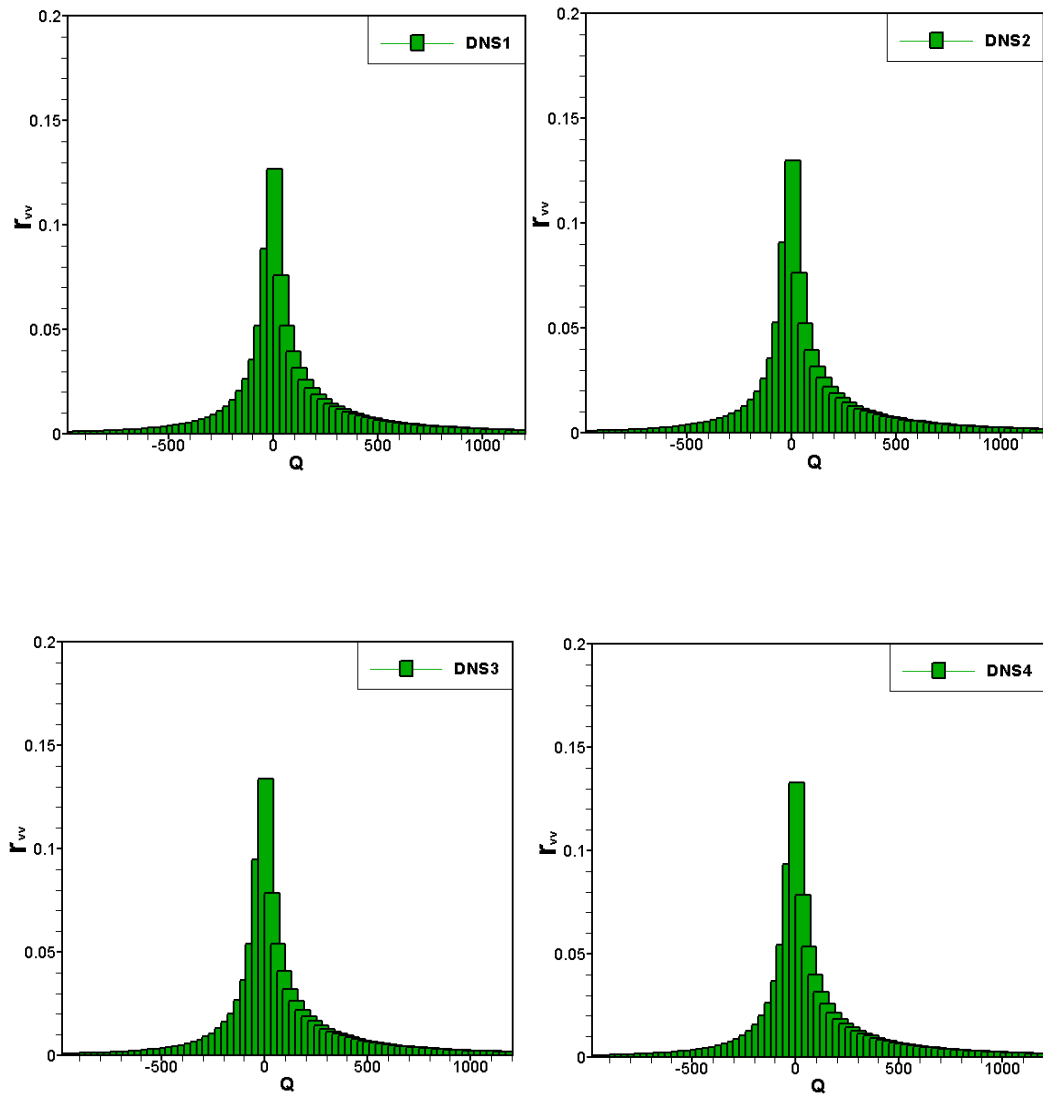
Figure 3.30: Instantaneous distribution of v'^2 according to Q.
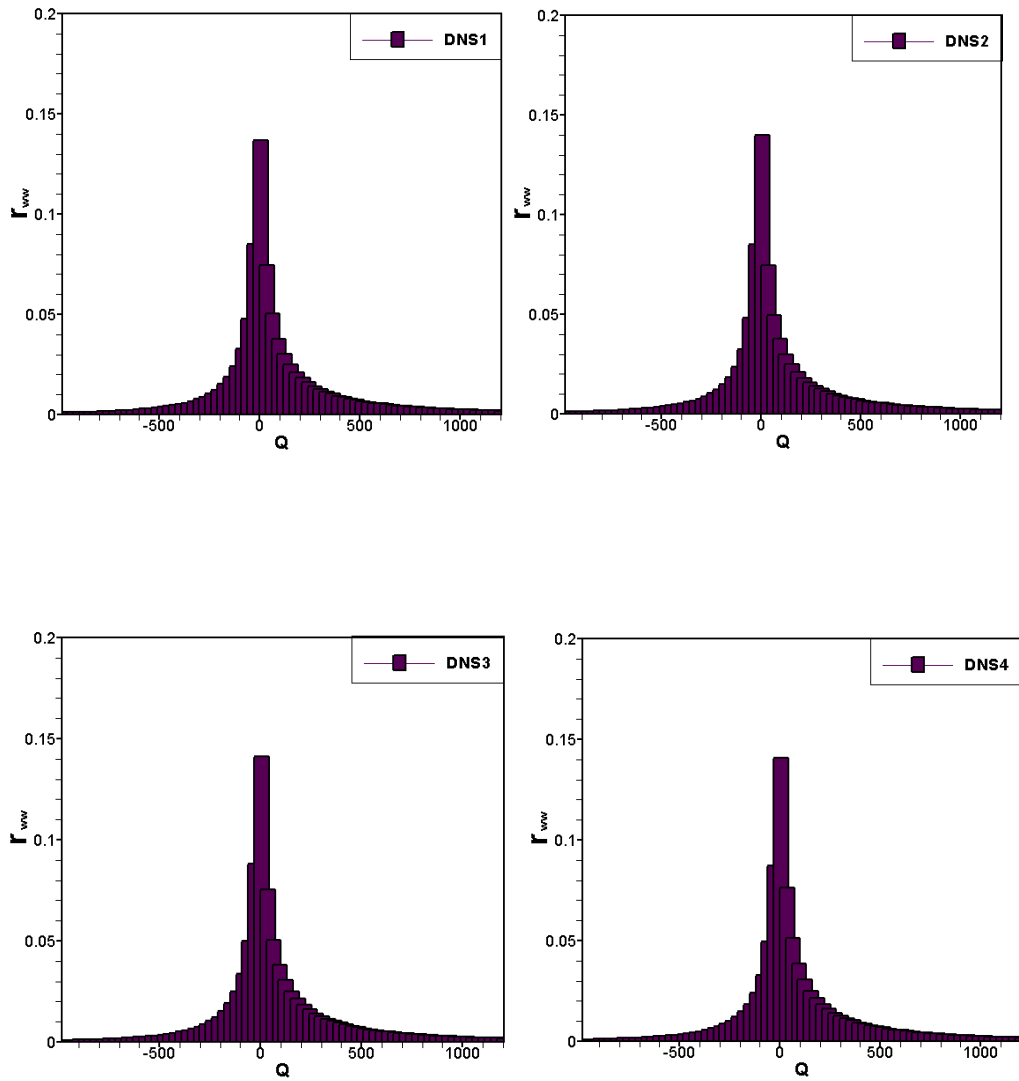
Figure 3.31: Instantaneous distribution of w'^2 according to Q.

3.4   Summary and Discussion

The results of a DNS of turbulent open-channel flow with a rough bed are employed to study the characteristics of the large-scale coherent structures. The majority of the structures locates in the inter-mediate region of the channel whilst the head of the hairpin vortices can reach the free-surface region and the small quasi-streamwise vortices grow from the wall region.

The length of the meandering structures can be larger than the length of the computational domain, here roughly 10 times the effective flow depth, and the width is between half to one effective flow depth. The structures are composed of small quasi-streamwise vortices at the bottom, larger quasi-streamwise vortices and asymmetric hairpin vortices above. The signature of the structures is the local maximum region of streamwise velocity created by the counter-rotating vortex pairs. The elongated high speed and low speed regions can perfectly explain the growth of the streaks along with the flow depth.

The model proposed explains the merging of the streaks from the near-wall region to the outer region as observed by many other studies, which cannot be explained by the hairpin packets mechanism. The large structures can not only activate the Reynolds Stress and Turbulent Kinetic Energy beneath the structures, but also above them. Below the structures, the fluctuation of streamwise velocity is more active than vertical and spanwise velocity. However, the vertical velocity fluctuation tends to be activated all the way up along with the flow depth, which is presumably

due to the upwash and downwash fluid between the vortices. Moreover, these vertical structures are demonstrated to contain more than 50% of the total RS and TKE. In particular, the small quasi-streamwise vortices contribute substantially to the stress and energy production.

Chapter 4
Structure Growth in the Larger Box

4.1   Literature Review

Adrian et al. (2000) reported the growth of the hairpin vortex packets in turbulent boundary layer flow at three different Reynolds numbers 930, 2,370 and 6,845. The hairpin vortices were about 200 viscous wall units near the wall and the distance between the vortex heads in the streamwise direction ranged from 100 to 150 viscous wall units roughly. The length of hairpin vortex packets could reach 2 times boundary layer thickness, with more than 10 hairpins in each packet. These packets were relatively stable and stretched along the whole flow depth, from the buffer layer to the outer region. The growth of the packets depended upon the growth of a single hairpin vortex in the packets as well as the organization of the vortices in the streamwise direction. They observed an obvious Reynolds number effect, i.e. when the Reynolds number increases, both the amount of hairpin vortices in the packets and the distance between the vortex heads increase.

Similar results were obtained by Roy et al. (2004) from measurements in gravel bed rivers, despite different flow conditions and bed roughness. Their results offered evidence that large-scale structures in rough-wall flow occupied the whole flow depth. The large structures were found to be 3 to 5 times flow depth in the streamwise direction and 0.5 to 1 times flow depth in spanwise direction.

Huther et al. (2007) measured the large scale coherent structures in rough wall open-channel flow with Reynolds numbers Re_θ varying from 1,300 to 7,900. The uniform momentum zones were produced by the streamwise coalescence of the hairpin vortices into a packet. They divided the uniform momentum region into three sub-zones according to their streamwise velocity. The zones might be not continuous due to the on-going development of the vortices and the separation between the zones depends upon the orientation of the vortices, which was shown to be a function of flow depth. The maximum length of the zone was 2.5 boundary layer thickness, agreed well with Adrian et al. (2000).
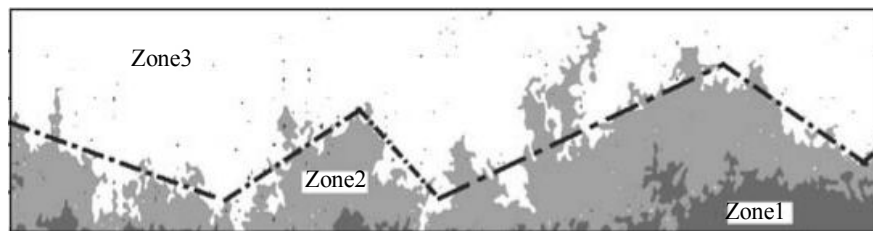
Figure 4.1: Three zones of uniform momentum(Hurther et al., 2007).

The lengths of large and very large scale motions in turbulent pipe flow (Guala et al., 2006) were shown to be 2 to 3 pipe radii and more than 8 to 16 pipe radii respectively. These two kinds of motions were generated from different mechanisms: the former from the connection of hairpin vortices and the latter from the alignment of the vortex packets. Their spectra analysis indicated that these very large structures produced more than half of the Reynolds stress and half of the turbulent kinetic energy of

streamwise fluctuating velocity. They also stated that these very large scale structures were fragile and thus possibly only occurred in fully developed pipe and channel flows, as well as gradually developing or equilibrium boundary layer flows. They also pointed out the necessity of computation, rather than modelling of the motions on account of the coherent stress for alignment.
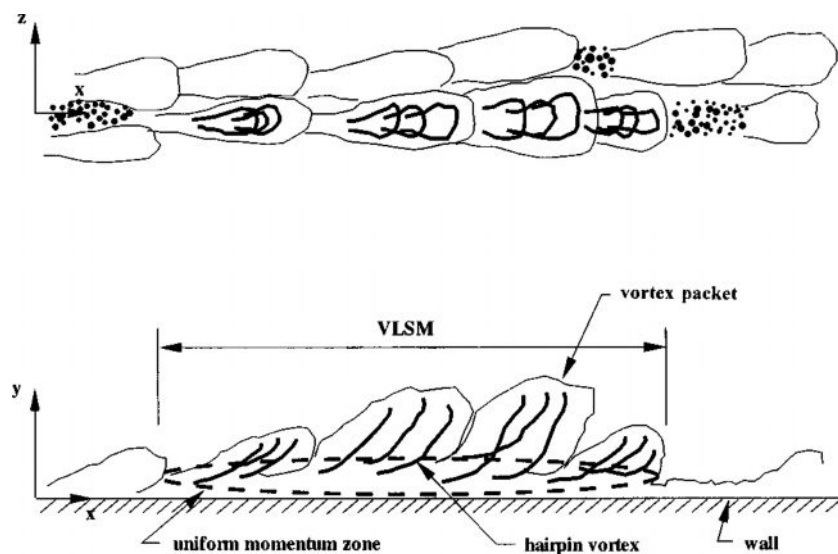
Figure 4.2: Connection of hairpin vortex packets in very large scale motions (VLSM) (Kim and Adrian, 1999).

Blakumar and Adrian (2007) compared large scale and very large scale motions in pipe flows (Fig.4.2), channel flows and boundary layer flows. The length of the large scale motions tends to increase from the wall until half depth of the channel and pipe, or the edge of boundary layer. The maximum length scale of the very large scale motions was shown to be

around 15 times channel depth in channel flows, 20 times pipe radius in pipe flows and about 4 times boundary layer thickness in boundary layer flows. They attributed the shorter length in the boundary layer flows to poor organization of the structures.

The length scale of the large coherent structures is an interesting topic since none of the studies reported a maximum value. It suggests that the connection of the structures can be continued in the streamwise direction if the domain is large enough. In order to observe the growth of the structures, the computational domain in this study is enlarged in both streamwise and spanwise directions. Although it is difficult to predict the maximum length scale, the influence of the computational domain on structure development can be observed.

4.2   Structure Growth

(a)

(b)
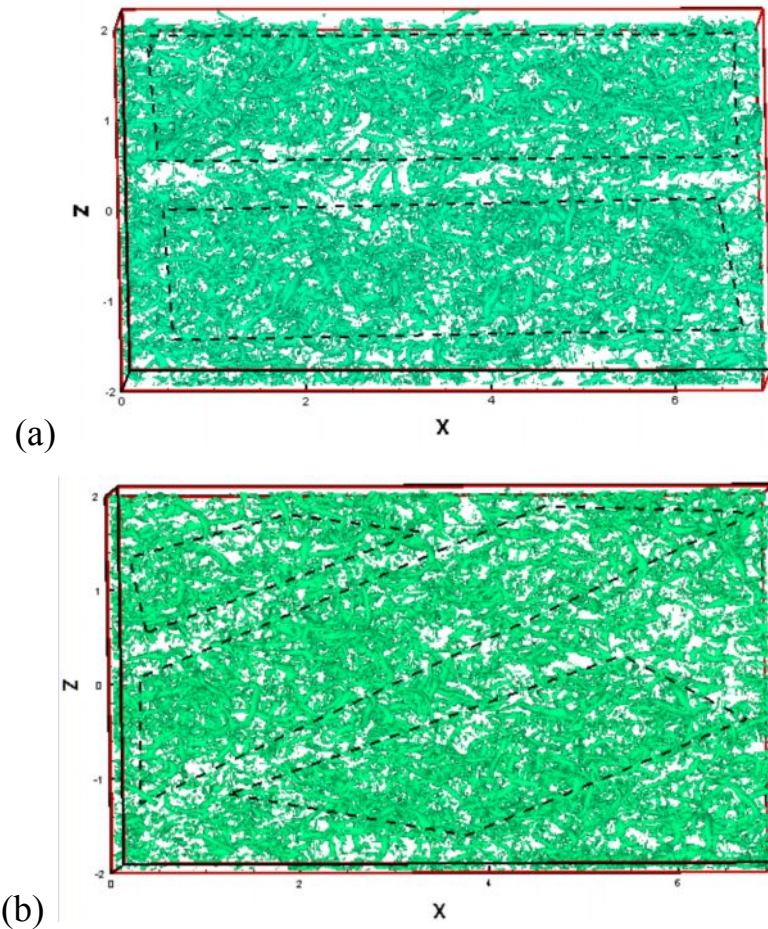
Figure 4.3: Two instantaneous large-scale coherent structures (a) and
(b) in the small box, visualized by *Q*-approach
(dashed lines denote large coherent structures).

The growth of the large-scale coherent structures due to the increase of the
computational domain can be observed clearly using the Q-approach, as in
Fig.4.3 and Fig.4.4 (Ma and Williams, 2010). By comparing the results of
the small and large box, it is found that the structures in the large box are
more complicated than those in the small one. In the large box, structures

of different length scales are aligned in different directions whilst in the small box, the two or three structures tend to be parallel. In addition to the chaotic organization, the extended domain is not large enough to capture the whole structure as the structure in the diagonal direction is simply longer than the length of box. Thus, even in the rough wall condition, very large structures can be longer than 20 times the effective flow depth, i.e. as long as those superstructures in pipe flows.

(a)

(b)
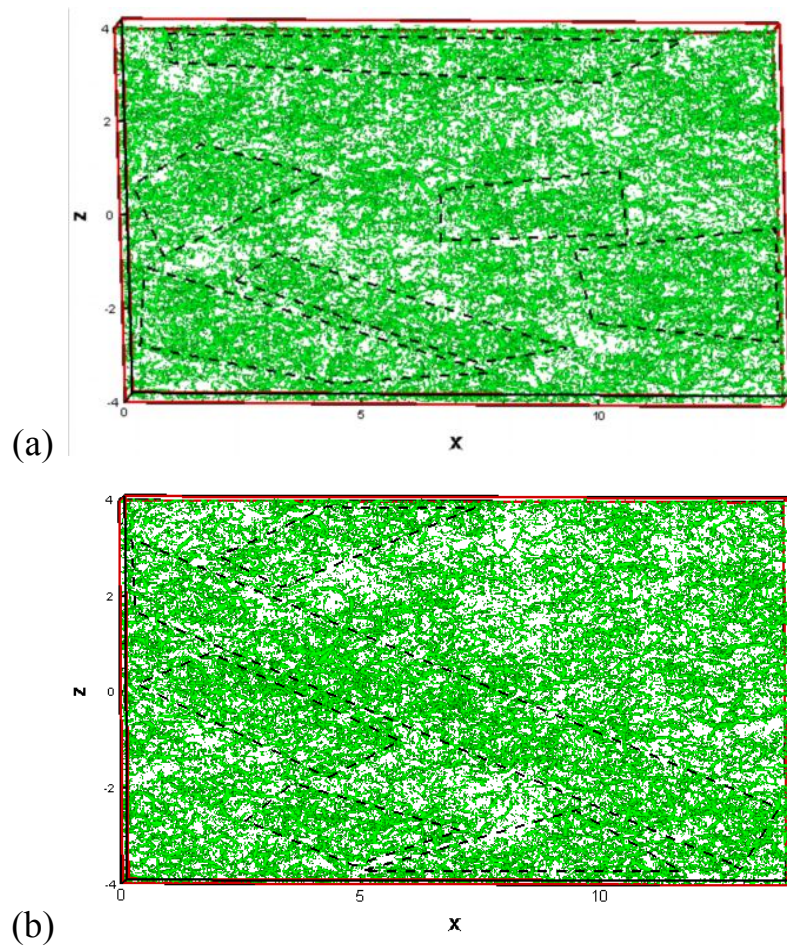
Figure 4.4: Two instantaneous large-scale coherent structures (a) and (b) in the large box, visualized by Q-approach (dashed lines denote large coherent structures).

Furthermore, the spanwise growth of the large structures as Tomkins and Adrian (2003) noted in their boundary layer flows was not observed. In their case, a merged low momentum region was observed downstream of the packet along with a stagnation point. But for the asymmetric hairpin vortices in this study, the flow pattern which produces high-speed momentum in the middle of the vortices is dominant, rather than the other pattern which produces low-speed momentum. Therefore, it is reasonable to conjecture that there is also a constant width for the large coherent structures composed of asymmetric hairpin vortices in the other flow conditions.

4.3   Two-point Correlations

Two-point spatial correlation is used for the measurement of structure length scale. The two-point spatial correlation (Bradshaw, 1971), is defined as $R_{uu} = \overline{u(x)u(x+r)}\big/\overline{u^2(x)}$. The length scale r is the distance between two adjacent points. Fig.4.5 ~ Fig.4.12 are the local streamwise and spanwise two-point correlations of the large structures ($L_{1\sim5}$ represent five adjacent correlations at the location of large structures) at different flow depth. The correlation of the large box is more fluctuating and the amplitude is smaller because more structures are contained in the box. Even the large box is not large enough to capture the whole structures as none of the streamwise correlation is equal to zero at the box extremity. Especially, the correlation of the streamwise fluctuating velocity is much larger than those of the vertical and spanwise fluctuating velocities. An ideal box should be a few times longer than the maximum length of a structure, and the correlation should be constantly around zero at the location of half of the box length. The width of the box is also not large enough. As observed in Fig.4.4, if the structure tends to align in the diagonal direction, the width also determines the organization of the structure. Therefore, the size of the computational and experimental domain simply determines the development of the flow structures and in consequence, the physical properties summarized from the data. This is an important reason for the different results obtained by different research groups.
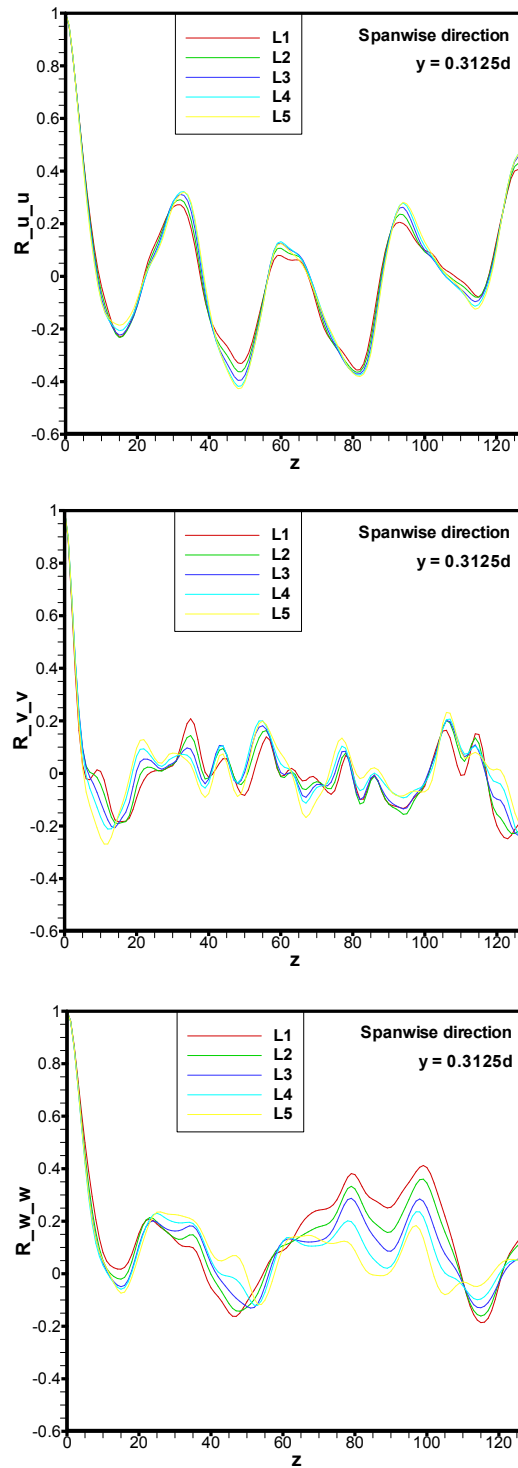
Figure 4.5: Spanwise two-point correlation of the small box at $y = 0.3125d$ (z is normalized by d).
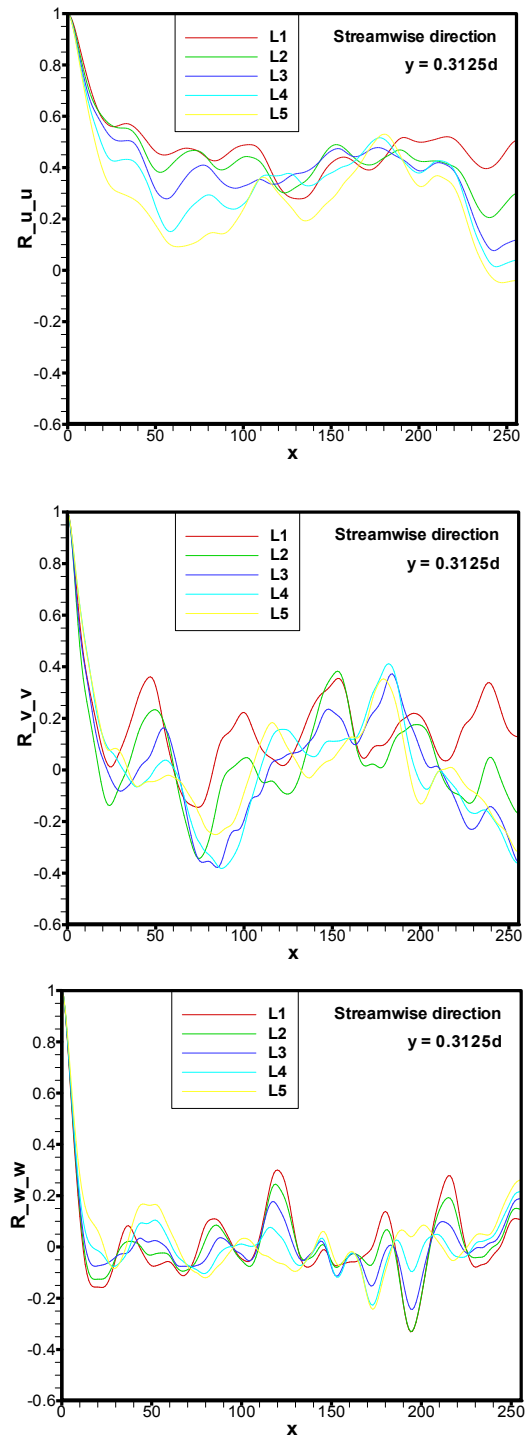
Figure 4.6: Streamwise two-point correlation of the small box at $y = 0.3125d$ (z is normalized by d).
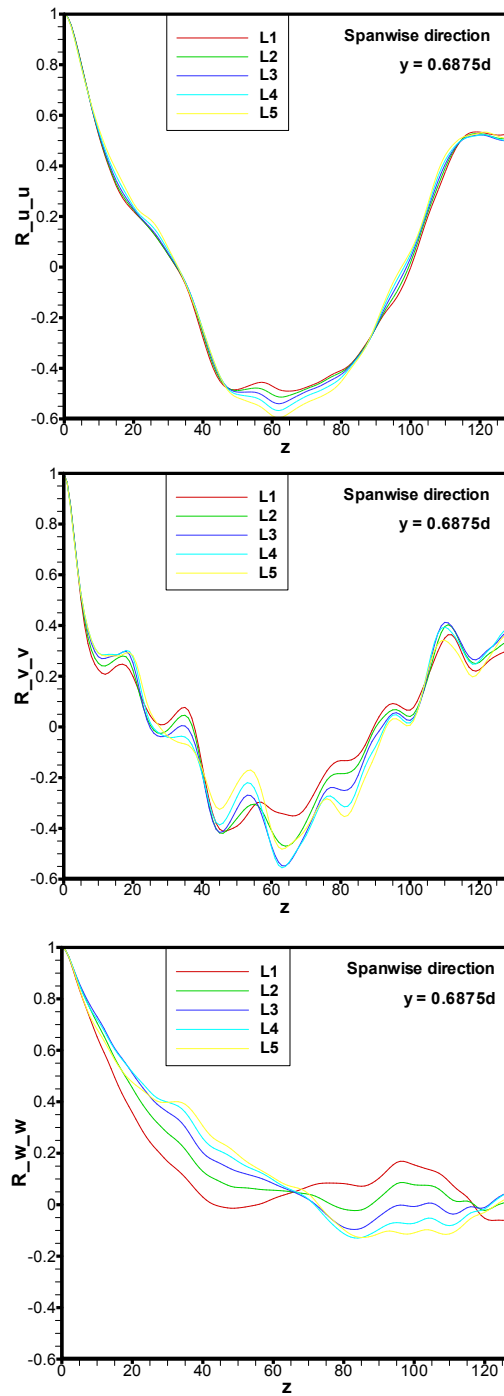
Figure 4.7: Spanwise two-point correlation of the small box at $y = 0.6875d$ (z is normalized by d).
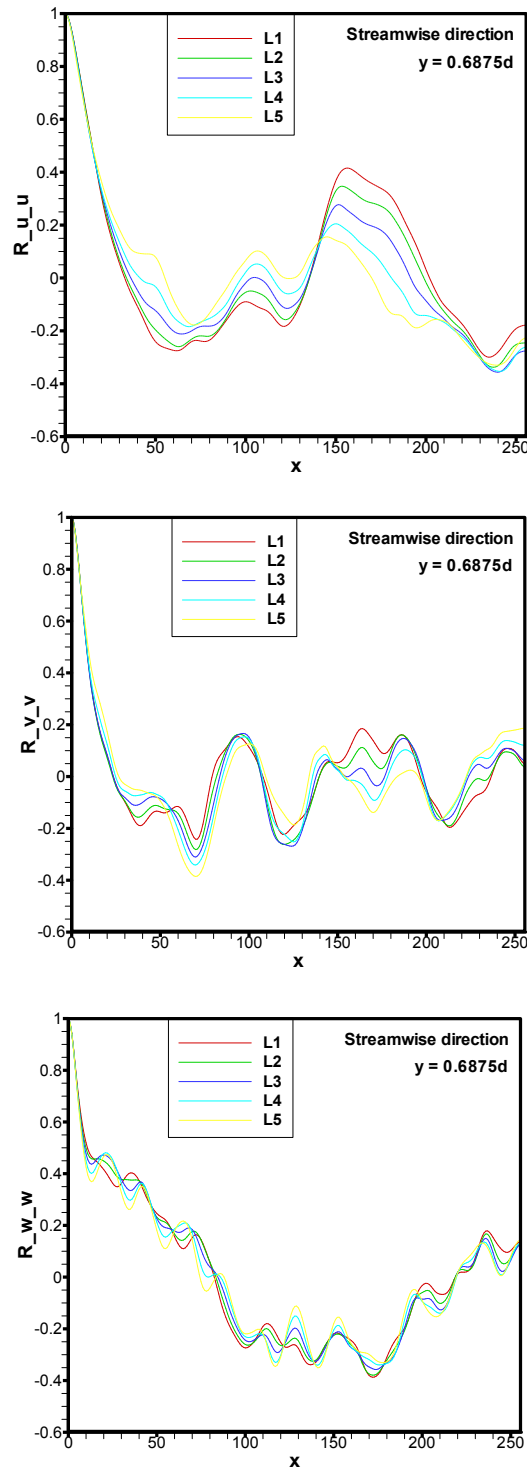
Figure 4.8: Streamwise two-point correlation of the small box at *y* = 0.6875*d* (*z* is normalized by *d*).
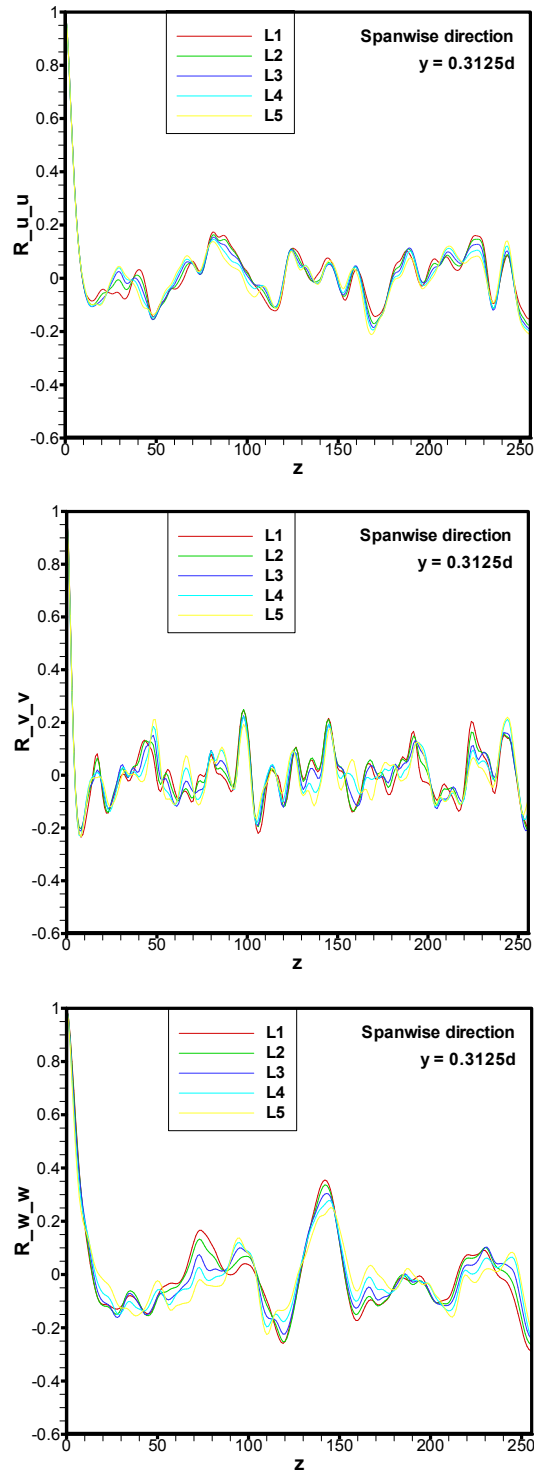
Figure 4.9: Spanwise two-point correlation of the large box at $y = 0.3125d$ (z is normalized by d).
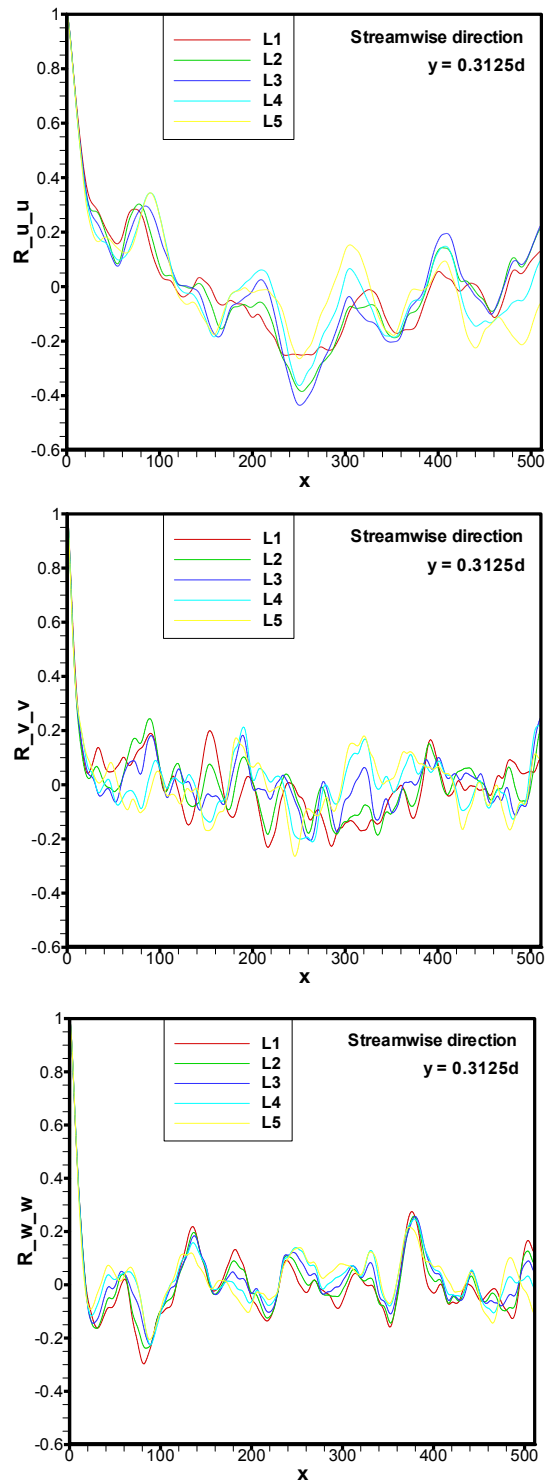
Figure 4.10: Streamwise two-point correlation of the large box at *y* = 0.3125*d* (*z* is normalized by *d*).
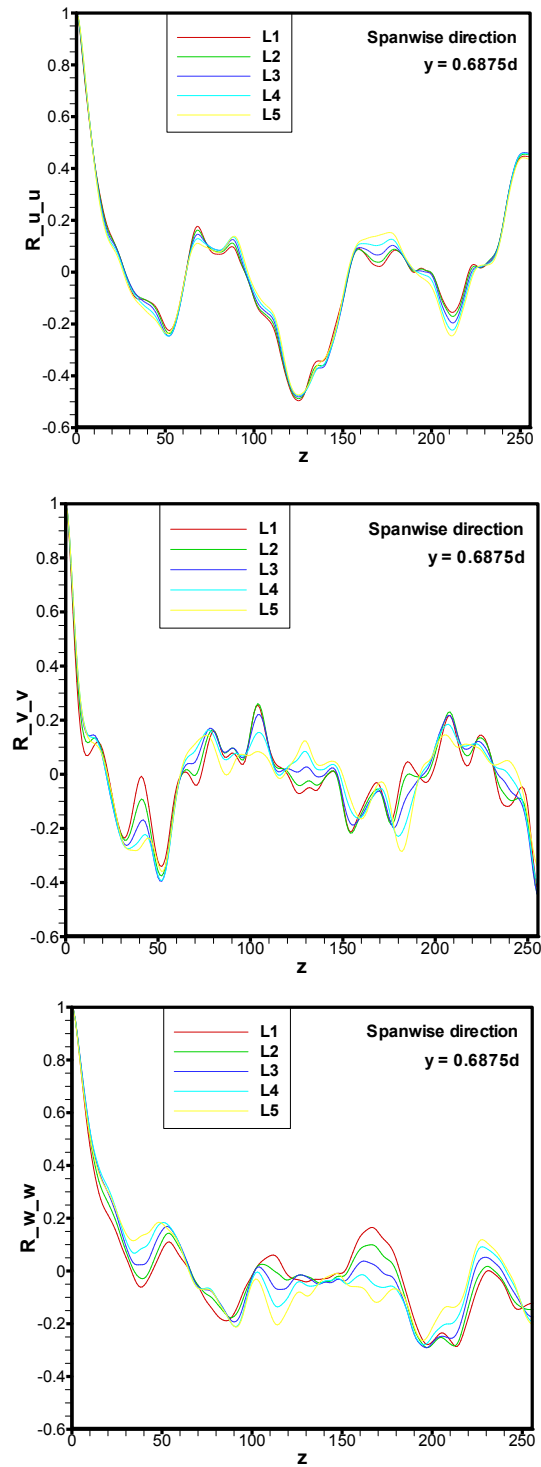
Figure 4.11: Spanwise two-point correlation of the large box at $y = 0.6875d$ (z is normalized by d).
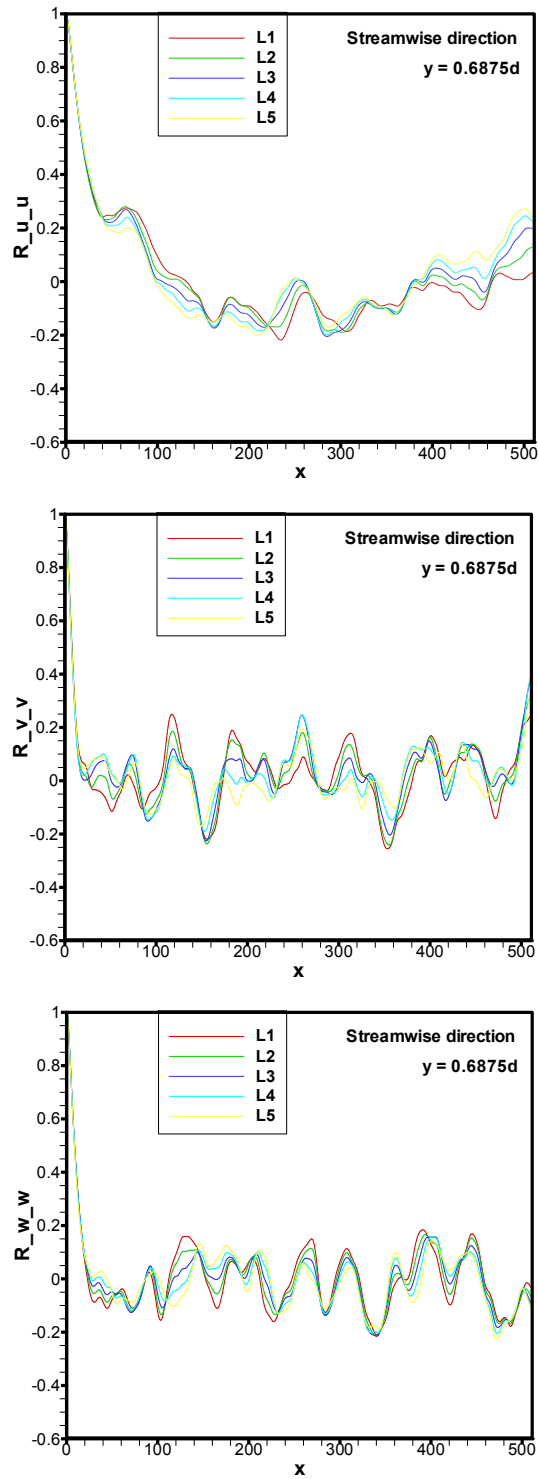
Figure 4.12: Streamwise two-point correlation of the large box at *y* = 0.6875*d* (*z* is normalized by *d*).

4.3 Summary and Discussion

The Large Eddy Simulation based on a couple of domains is performed to study the development of the large-scale coherent structures due to the increase of computational box. More vortices aggregate together to form the vortex packet when the box is enlarged. The structures in the large box are more complex and seem to be chaotic whereas in the small box, the structures tend to be parallel.

Two-point correlations suggest that even the large box cannot capture the whole large structures, which are shown to be more than 20 times the effective flow depth. Therefore, we can conclude that even in the rough wall condition, these very large structures can be as long those in the pipe flows. The alignment of the large structures in the diagonal direction implies that not only the length of the box, but the width controls the development of the structures to a large extent. Thus, for the study of the large coherent structures, the size of the computational or experimental domain determines the organization of the structures and also the physical properties of the flow field.

Chapter 5
Near-bed coherent structures

5.1 Literature Review
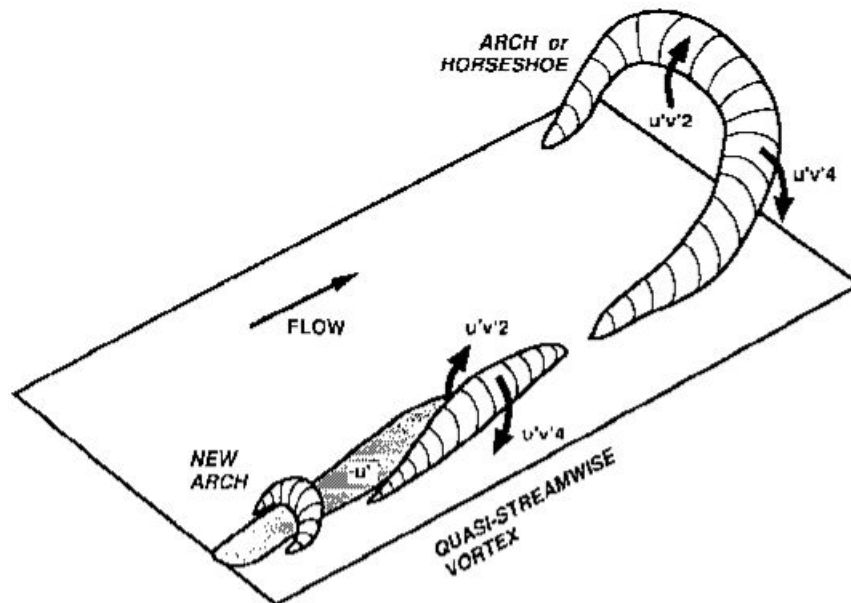
Figure 5.1: Quasi-streamwise vortex and bursting events in the near wall region (Robinson, 1991).

Brooke et al. (1993) investigated the origin of streamwise vortices (Fig.5.1) using Direct Numerical Simulation. The vortices were shown to be produced by the rise-up of large eddies from the near wall region and featured with opposite sign vorticity from the parent vortex. The authors argued that the vortices originated by themselves and thus were independent from the outer region.

The effect of surface roughness in the turbulent boundary layer flow was reported by Grass (1971). The ejection and inrush events primarily existed under different kinds of wall roughness and both contributed substantially to Reynolds Stress production. These events were shown to be discontinuous and randomly recurring. The influence of inrush events was generally restricted to the wall region whereas the ejections could reach the region far away from the boundary. The difference between smooth and rough surface boundaries was that in the smooth-wall condition, the fluid between the roughness elements remained stable whilst in the rough-wall condition, the fluid was more active during ejections. Therefore, surface roughness simply determined wall region stability according to this experiment.

Smith and Metzler (1983) reported that the spanwise spacing of low-speed streaks was independent of the Reynolds number and increased with flow depth due to merging and intermittency effect. The streaks were also shown to be persistent, which was due to the hairpin vortices. The low-speed streaks could remain stable much longer than the bursting time. The stretching of the counter-rotating vortices in the streamwise direction stabilized the streaks.

Wallace et al. (1972) measured the fractional contributions of four quadrant events to Reynolds Stress production in the near-wall region. The second and fourth quadrant events, i.e. ejections and sweeps, together contributed more than the total Reynolds Stress. The first and third quadrant events, i.e. outward and inward events, reduced the total

Reynolds Stress as their production was of the opposite sign. The timescales of ejections and sweeps were shown to be substantially larger than the other two events. The high energy dissipation regions were also related to the ejections and sweeps. Similar results regarding Reynolds Stress contribution and energy dissipation of the four events were observed by Nakagawa and Nezu (1976). They also reported the roughness effect of the wall, i.e. sweeps became more important than ejections when the roughness increased.

Blackwelder and Haritonidis (1983) argued that the frequency of the bursts should be scaled with the inner variables, rather than the outer variables. The frequency was basically independent of Reynolds number, though a slight decrease appeared when Reynolds number increased. They emphasized the importance of sensor length during the experiment as the spanwise structure of the eddy could be captured only when the sensor was small enough.

Raupach (1981) compared the characteristics of Reynolds Stress in rough-wall and smooth-wall turbulent boundary layers. The rough-wall was represented by cylindrical roughness elements arranged in square or diamond arrays of different densities. The result showed that the sweep was the main contributor of the Reynolds Stress in the near-wall region of several roughness heights, especially very adjacent to the rough surface. The sweep contribution also increased along with the increase of roughness concentration. The fractional contribution difference between ejections and sweeps to Reynolds Stress was strongly associated with the

streamwise and vertical fluctuating velocities.

Luchik and Tiederman (1987) developed detection methods for the timescale measurement of bursts in channel flows. They grouped several ejections into one single burst rather than detected the ejections separately. The average time between the bursts could be related to inner variables, wall shear stress and kinetic viscosity, instead of outer or mixed variables.

Nakagawa and Nezu (1981) investigated the space-time correlations of bursting events in the open-channel flow and proposed a qualitative model. Both the spatial and time scales of the sweeps were larger than the ejections. For the ejections, the spatial scale towards downstream direction was larger than towards upstream direction. However, the opposite condition occurred for sweeps. The spanwise spacing of the streaks keeps constant in the buffer layer, yet increased along with flow depth above that.

Lu and Willmarth (1973) experimentally studied the features of Reynolds Stress in the near-wall region of a boundary layer flow with different flow velocities. The convection velocities of the bursts and sweeps were approximately equal. The bursts were shown to contribute 77% of the total Reynolds Stress and the sweeps to contribute 55%. The mean time intervals of the two events were equal and kept constant under different flow conditions.

Sumer and Deigaard (1981) compared the particle motions in smooth-bottom and rough-bottom turbulent open-channel flows. The rough-bottom was represented by one layer of uniform pebbles and the roughness Reynolds number was 81. Their observation showed that the transport behaviour of small heavy particles was similar in the two bed conditions: the particles were first ejected from the near-wall region, then separated from the burst, and finally swept into the low-speed streaks. Although the particle motion was more intense in the rough-wall condition, there was no significant difference in the velocity profiles and frequency histograms of upward termination between smooth and rough conditions.

The near-wall vortex dynamics was reported by Bernard et al. (1993). The quasi-streamwise vortices were the dominant structures in the wall region, which were featured by self-production. The new vortices, which were easily nested by the old ones, were likely to be generated near the sweeps if the old vortices were strong enough to rotate the adjacent fluids. The appearance of spanwise vortices was explained by the interaction between the streamwise vortices during the transport process away from the wall. The high-speed upwash and downwash fluid was intensified by the counter-rotating vortex pairs, especially those of different convection velocities. The difference between the convection velocities eased the encounter and connection of the vortices. The large wall pressure and Reynolds Stress production were associated with the near-wall streamwise vortices, especially with the accompanied sweeping events. Further, the tilt of the vortex cores, which accelerates the velocities of the adjacent fluid, was another source of Reynolds Stress production.

Jimenez and Pinelli (1999) presented a near-wall regeneration cycle in a turbulent channel flow, which was independent of the outer flow (Fig.5.2). The cycle included two aspects: one was the generation of the streaks through the energy extraction from the main flow by the streamwise vortices and the other one was the formation of the vortices by the dynamics of the streaks. The other mechanisms, e.g. self-production from secondary vortices and outside flow disturbance, were taken to be secondary, though possibly exist in the other flow environment. They attributed the dependence of near-wall statistics on the Reynolds number to the other mechanisms which was not included in their study. However, this single process was shown to determine the majority of the near-wall dynamics. Moreover, the disturbance of the dynamic process was possibly the reason for drag reduction and turbulence decay.
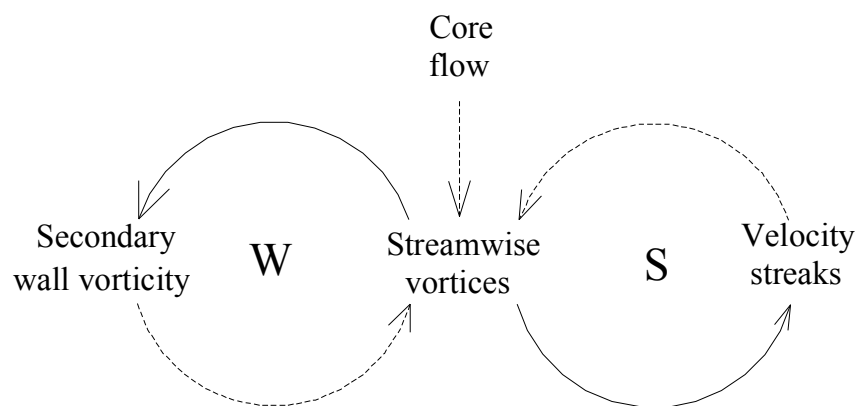
Figure 5.2: Mechanisms of turbulence production in the near-wall region (Jimenez and Pinelli, 1999).

Krogstad et al.(1992) reported the differences between rough-wall and smooth-wall boundary layer flows. The high surface drag due to the roughness caused the mean velocity profile of rough-wall to differ from the smooth-wall condition. The roughness also caused considerable increases of vertical turbulence intensity and Reynolds Stress. The ejections and sweeps over the rough-wall surface were much stronger and twice as frequent as those over smooth-wall surface. In consequence, the contributions from these two quadrant events to total Reynolds Stress were much larger. Such roughness effect on vertical intensity in the near-wall region was also reported by Jackson (1976) in his comparison of bed ripples. The spectral analysis showed difference between the two surfaces over the whole wavenumber, especially for the strength of vertical motion in the near-wall region.

Hamilton et al. (1995) performed a Direct Numerical Simulation, which was started from a fully developed turbulent flow, and reduced the streamwise and spanwise lengths of the computational domain to observe the regeneration mechanism in the near-wall region. The whole dynamic process was composed of three phases: streak generation, streak breakdown and vortex regeneration. The result also suggested that when the domain was further reduced, the dynamic process would be disrupted because the streak spacing was too small. Thus, a proper computational domain is the prerequisite of the simulation, which depends on the length scales of the flow structures.

Cao (1997) was probably the first to incorporate the near-bed coherent structures into the modeling of sediment entrainment. Average bursting period and mean area of all bursts per unit area were used as characteristic parameters of bursts for the flat, loose bed condition in the entrainment function. Good agreement was obtained compared with available experimental data. This implied that the prediction of sediment entrainment must be closely associated with the instantaneous turbulent flow field, rather than the mean flow velocity.
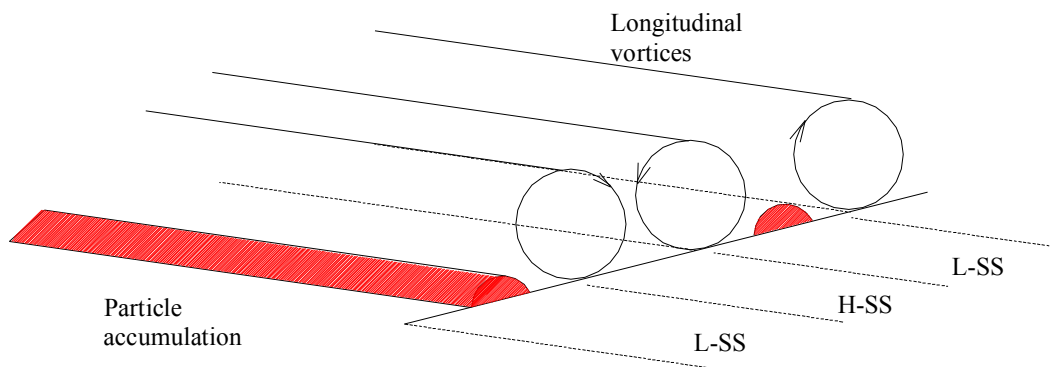
Figure 5.3: Particle accumulation due to quasi-streamwise vortices (Nino and Garcia, 1996).

Nino and Garcia (1996) employed a high-speed video system to investigate the relationship between the movement of sediment particles and flow structures in the near-wall region of an open-channel for both smooth and transitionally rough bed conditions (Fig.5.3). Flow Reynolds numbers ranged from 5,000 to 30,000 and Froude numbers from 0.5 to 0.6. For smooth bed flows, visualizations of the particles moving along the

channel bottom showed that the particles immersed in the viscous sub-layer were aggregated along low-speed streaks, through the sequence of being picked up from low-speed streaks, deposited into high-speed streaks and eventually pushed toward the low-speed streaks due to streamwise vortices. Average spanwise spacing between the streaks was roughly 100 wall units, implying a negligible effect on the spacing of the streaks from the particles. Also, the observations indicated a stabilizing effect on the viscous sub-layer in that the streaks were more persistent than those without particles. The large particles of sizes larger than the thickness of viscous sub-layer did not accumulate along the streaks but exhibited sudden accelerations due to inrushing fluid. For transitionally rough flows on the other hand, the formation of streaks was less obvious than in smooth flows, presumably because of the disturbance of the roughness elements. The small particles were observed to move within the interstices of the roughness elements, whilst large ones move over the elements without showing any tendency to group along the weak streaks.

Nelson et al. (1995) experimentally demonstrated that sweeps and outward interactions were the two main contributors of bed-load transport. They argued that the bed shear stress was a proper parameter for the estimation of sediment movement in well-developed boundary layers with steady and uniform flow, but not for developing boundary layers. In particular, non-uniform roughness could influence the distribution and characteristics of bursting events, though not the bed shear stress.

In the experiment conducted by Gyr (1997), sediment entrainment was intermittent and occurred randomly everywhere. Quasi-stable longitudinal sediment stripes were observed on each side of sweeps with an elevation of approximately one grain diameter. An interesting phenomenon was that when the wall shear stress increased, the stripes were destroyed and formed an arrow-like pattern. The distance between subsequent arrow patterns corresponded to the averaged length scale of sweeps. They concluded that the sweeping event was the only reason for movement and that the wall shear velocity only accounted for less than 30% of sediment transport.

Sechet and Guennec (1999) measured the time and space scale of the bed-load particle motions and the period of bursting events. They captured the displacement of sediment particles in smooth-bed open channel flow and compared the trajectories with the characteristic scales of bursting events. Results indicated that the average time between two successive displacements of sediment particles were roughly the same as the average time between two ejections, with a few exceptions whose resting time was on average longer than the ejection period. They postulated that there existed two kinds of transport modes for bed-load motion: one due to ejections, the other because of sweeps.

Cellino and Lemmin (2004) studied the interaction between coherent structures and suspended particles in both suspension flows and clear-water flow. In their case, the channel bed consisted of a single layer of gravel which were stuck to fixed plates. Conditionally averaged

instantaneous velocity profiles and suspended concentration profiles showed that the sequence of sweep and ejection was responsible for the dislodgement of particles over the whole flow depth. They also confirmed that ejections were the principal contributor of sediment suspension.
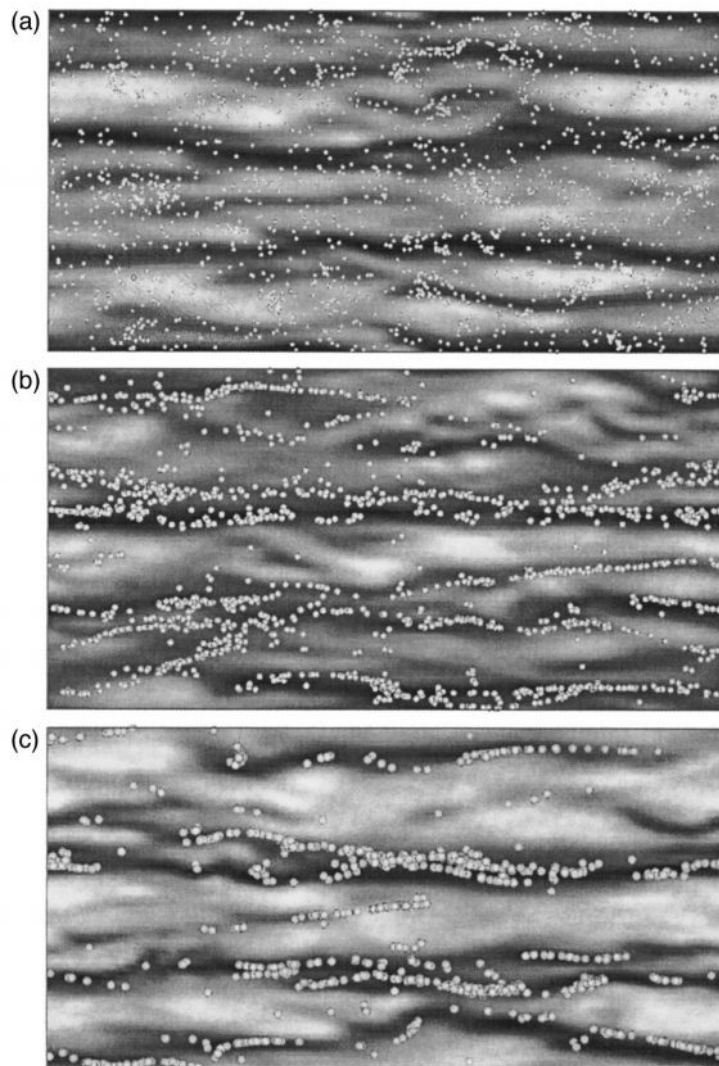
Figure 5.4: Particle distributions due to the effect of streaks (Pan and Banerjee, 1996).

Pan and Banerjee (1996) numerically investigated the interaction between particles and wall turbulence in an open-channel flow with Reynolds numbers of 85.4, 147.5 and 150 (Fig.5.4). Particle diameter, volume fraction of particle phase and still-fluid settling velocity were varied separately to check the interaction between fluid and particles. They showed that all the particles tended to move into the region with lower-than-mean fluid velocity and that the heavier-than-fluid particles were accumulated along the low-speed streaks and the smaller ones uniformly distributed in this region. They related such segregation to particle response time to local turbulence time scales, i.e. the smaller particles were much easier to be re-entrained and less likely to be pushed aside along the streaks compared to the larger ones.

Soltani and Ahmadi (1995) carried out a direct numerical simulation of particle entrainment in wall-bounded turbulent channel flow with a flow Reynolds number of about 6,500. The particle trajectories showed that the ejected particles formed lines with a spacing of about 100 to 150 wall units, which was approximately equal to the spacing of streaks in the viscous sublayer. The lines shifted due to the breakup of vortices and the generation of new ones as time progressed. In their case, there were more single streamwise vortices than counter-rotating vortex pairs. Particle trajectories also indicated that groups of entrained particles were, presumably, the result of the action of a single vortex whilst the effect of clockwise and anti-clockwise vortices were roughly the same on the entrainment of all particles.

Wu and Jiang (2007) incorporated a Gram-Charlier-type joint probability distribution of near-bed two-dimensional instantaneous velocities into a simple mechanistic model to study the effect of bursting events on entrainment. Lifting was the dominant mode for the entrainment of fine sediment and rollover was the predominant mode for coarse ones. Ejections and sweeps were shown to be more frequent than inward and outward events and that sweeps were the main factor for the entrainment in all cases. The critical velocity of entrainment decreased due to the increase of the standard deviation of grain-size distribution.

The near-wall coherent structures are composed of quasi-streamwise vortices and bursts. The effect of quasi-streamwise vortices on sediment entrainment is that the particles can be pushed or even absorbed by the vortices, depending on the particle density (Soltani and Ahmad 1995, Pan and Banerjee 1996, Nino and Garcia 1996). The influence of bursts is that the particles can transport along with ejections and sweeps, though it is not clear which bursting event is the dominant factor (Cao 1997, Nelson et al. 1995, Sechet and Guennec 1999, Cellino and Lemmin 2004, Wu and Jiang 2007). However, these near-wall coherent structures are affected by the particles either due to bed roughness or particle transport (Grass 1971, Raupach 1981, Sumer and Deigaard 1981, Krogstad et al. 1992, Nino and Garcia 1996). Therefore, the role of these structures on sediment transport is greatly determined by the sediments themselves.

In this study, the exact relationship between near-wall coherent structures and force moments exerting on the gravels will be studied, which is

essential for the modeling of sediment entrainment. Future work can investigate the relationship under different packing conditions in order to obtain a more realistic result for engineering application.

5.2 Quasi-streamwise Vortices

In order to investigate the influence of the quasi-streamwise vortices, the spheres which are influenced by single quasi-streamwise vortices are selected and the enstrophy $E = (\overline{\omega_x^2} + \overline{\omega_y^2} + \overline{\omega_z^2})/2$ of each vortex is calculated, where ω_x, ω_y and ω_z are angular velocities of a vortex in the x, y, z directions respectively (Nezu and Nakagawa 1993). The result shows that the streamwise vortex plays a deterministic role on M_{D2} on account that when M_{D2} is positive, the vortex is above the positive side of the sphere, whilst when M_{D2} is negative, the vortex is above the negative side of the sphere, as in Fig.5.5 and Fig.5.6 (Ma and Williams, 2009c). The vortices create a low pressure area on top of the sphere and in consequence, the moment in the spanwise direction. Obviously, the difference between sand and gravel bed conditions lies in the low pressure area due to vortex core. In sand bed cases (Soltani and Ahmadi 1995, Nino and Garcia 1996, Pan and Banerjee 1996), the particles tended to be pushed along the side of the vortex, rather than absorbed into its core, which means the rotation direction of the vortex determines the direction of particle movement. Here, in contrast, the influence of rotation direction is so small compared to the pressure difference that it can be considered to be a supplementary factor.

Angular velocities of the vortex vectors are used to estimate the diameter of vortices which is roughly d/8. The shape of near-bed quasi-streamwise vortices are not standard circles. Vortex diameter in the horizontal direction, rather than the vertical direction, is taken as an estimate because the vortex goes along the sphere surface mainly in horizontal direction.

Another factor which may influence the estimation of vortex diameter is its meandering, which changes the lever arm of the force slightly.

For a large vortex with an approximate diameter of $d/8$, M_{D2} decreases along with the increase of E; for a small vortex with an approximate diameter of $d/16$, the substantial distance between the sphere surface and the vorticity core reduces the influence of the vortex in some cases. In addition, it is the shape of the vortex which determines the area of exertion as this follows the surface of the sphere.

The high-speed upwash and downwash fluid, which originates from the high pressure area just above the sphere surface between the streamwise vortices, also plays an important role. Large M_{D2} is strongly associated with the combination of the vortex and the adjacent high speed fluid: one side of the sphere experiences extremely low pressure whilst the other high pressure (Fig.5.7). Such a combination is particularly favourable for the rollover of the sphere in the spanwise direction . Moreover, when the sphere is influenced by two or three vortices, the resultant moment depends on the position of the vortex set. If the vortices occur above the same side, the resultant moment is dramatically large; if they appear above different sides or just the top, the moment is quite small due to counterbalance (Fig.5.8). However, in the latter case, extreme large lift moments can be observed on account of the pressure gradient.
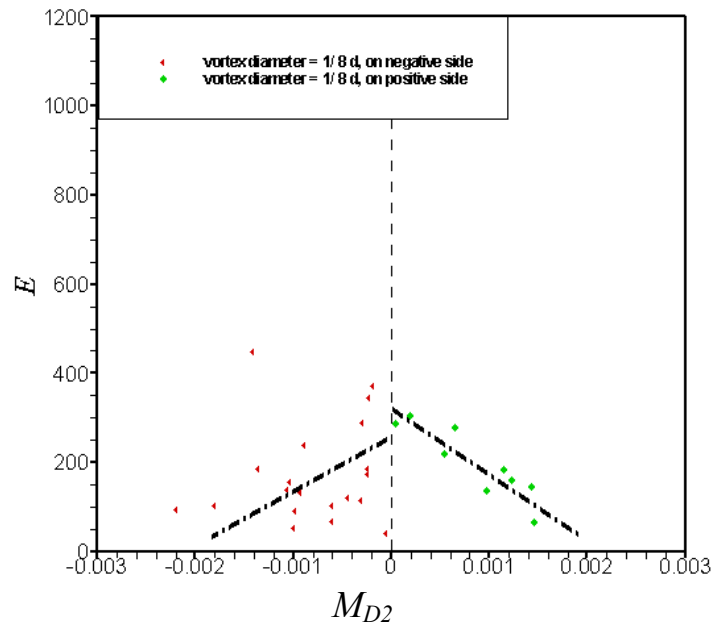
Figure 5.5: Relationship between M_{D2} and E
(M_{D2} is normalized by $\rho u_\tau^2 d^3$ and E is normalized by u_τ^2/d^2).
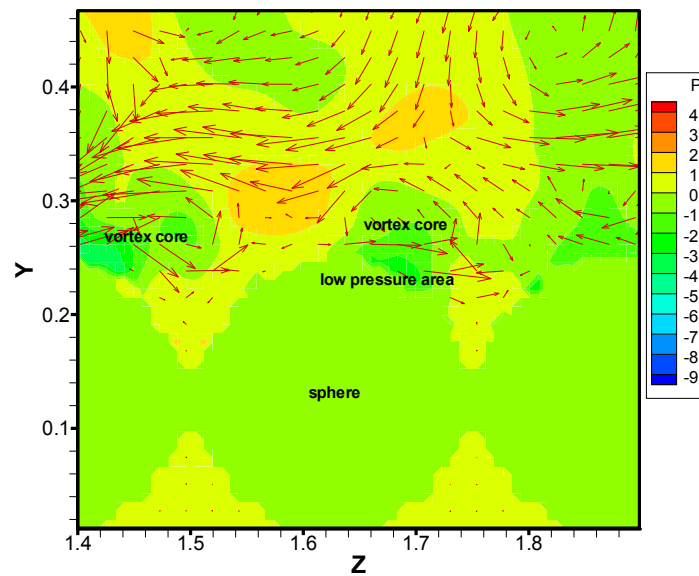
Figure 5.6: Single quasi-streamwise vortex on the positive side of sphere (P is normalized by ρu_τ^2, Y and Z are normalized by d).
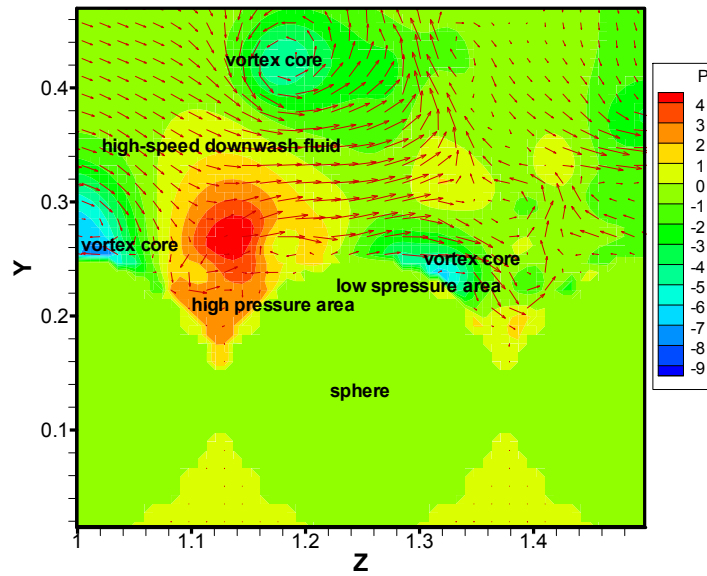
Figure 5.7: Flow structure responsible for large M_{D2}: high-speed fluid on one side of the sphere and single quasi-streamwise votex on the other side (P is normalized by ρu_τ^2, Y and Z are normalized by d).
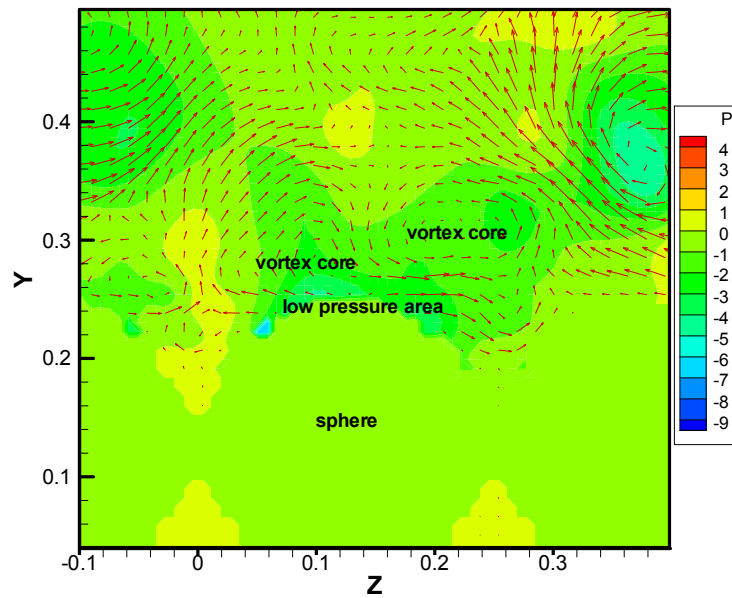
Figure 5.8: Counterbalance of a counter-rotating vortex pair for M_{D2} (P is normalized by ρu_τ^2, Y and Z are normalized by d).

5.3   Bursting events

Ejections and sweeps are frequently occurring bursting events near the bed due to vortices (Robison 1991). During ejection events, the low speed fluid is pushed away from the bed whereas in a sweep event, high speed fluid rushes inwards.

In order to distinguish bursting events from high speed upwash and downwash fluid between the quasi-streamwise vortices, the bursting produced by spanwise vortices are considered and a Reynolds decomposition is used. However, as presented by Adrian and Tomkins (2000), different reference frames produce different results because of the different velocities of the vortex cores. By comparison, it is found that the bulk mean velocity is roughly equivalent to the velocity of the vortex cores near the bed, although some vortices are lost further away which have a much larger velocity. All the spanwise vortices near the bed are therefore captured by subtraction of the bulk mean velocity.

All the successive fluid particles above the sphere are captured, whose velocity components are defined as ejections and sweeps, i.e. *u' < 0, v' > 0* and *u' > 0, v' < 0* respectively, and the average of the velocities is taken as an estimate of the representative velocity components for the bursting events.
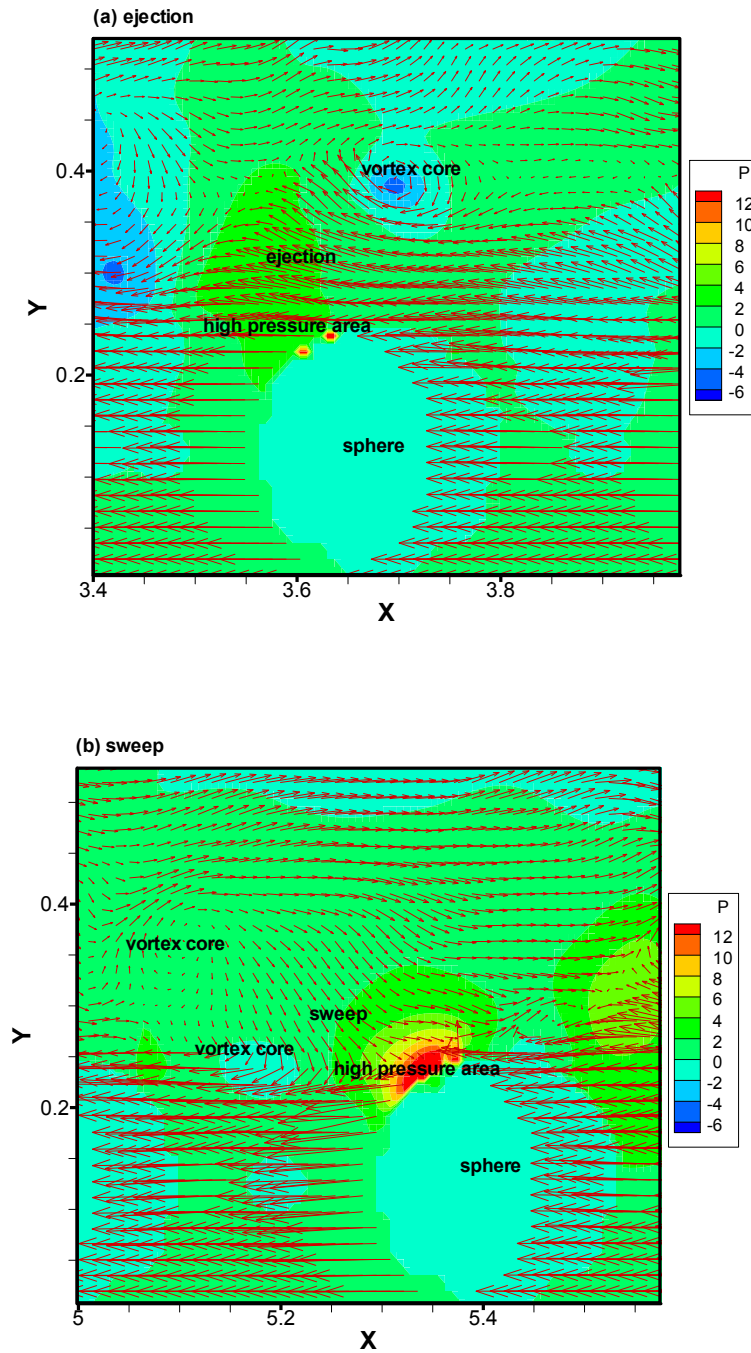
Figure 5.9: Effect of bursting events produced by spanwise vortices: (a) ejection and (b) sweep (P is normalized by ρu_τ^2, X and Y are normalized by d).
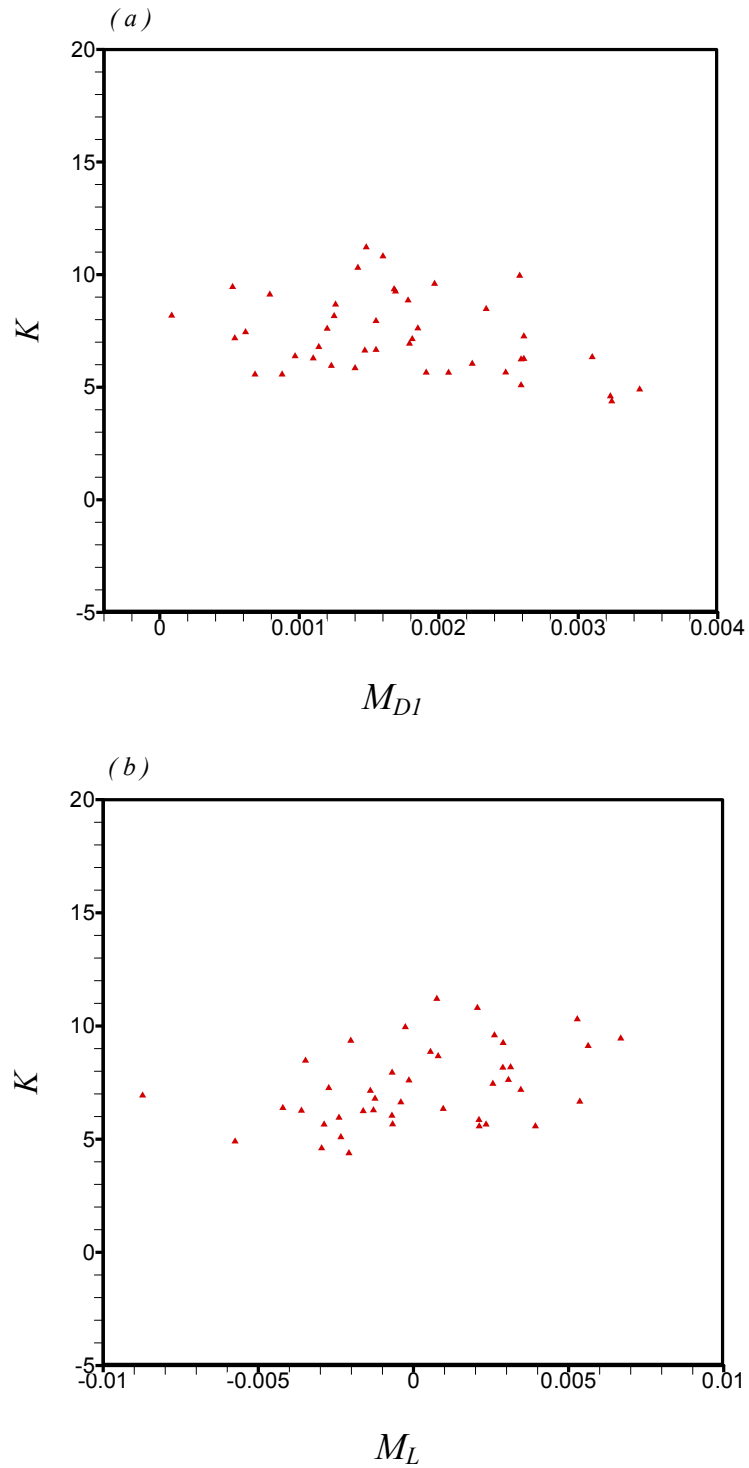
Figure 5.10: Variation of M_{DI} and M_L with K during ejection events (K is normalized by u_τ^2, M_{DI} and M_L are normalized by $\rho u_\tau^2 d^3$).

Fig.5.10 and Fig.5.11 show the relationship between the moment and turbulent kinetic energy $K = (\overline{u'^2} + \overline{v'^2} + \overline{w'^2})/2$, where u', v' and w' are representative fluctuating velocities of the bursting events. M_{DI} is positive for both ejections and sweeps whereas M_L is mainly negative for sweeps. During ejections, M_{DI} decreases along with the increase of K whilst M_L varies from negative to positive; during sweeps, both of large M_{DI} and M_L can be caused by intensive sweeping events. However, some fluctuations of data points can be observed during sweeps, which are probably due to the influence of adjacent vortices.

When it comes to M_{DI}/M_L, during sweeps, almost all of the ratio ranges from -1 to 0 with M_L being mainly negative (Fig.5.12). On the contrary, the moments are positive for high energy ejections. This implies that, for the initiation of entrainment, an ejection is more favourable than a sweep and the latter makes a gravel bed more stable, at least for a closely packed condition. Fig.5.9 shows the effect of ejection and sweep events on the stability of the sphere: in both conditions, there exist a high pressure area on the sphere surface. The position and direction of the events may determine the degree of the influence on the sphere, which is the possible reason for the scatter of data.

(a)

K

M_{DI}

(b)

K

M_L
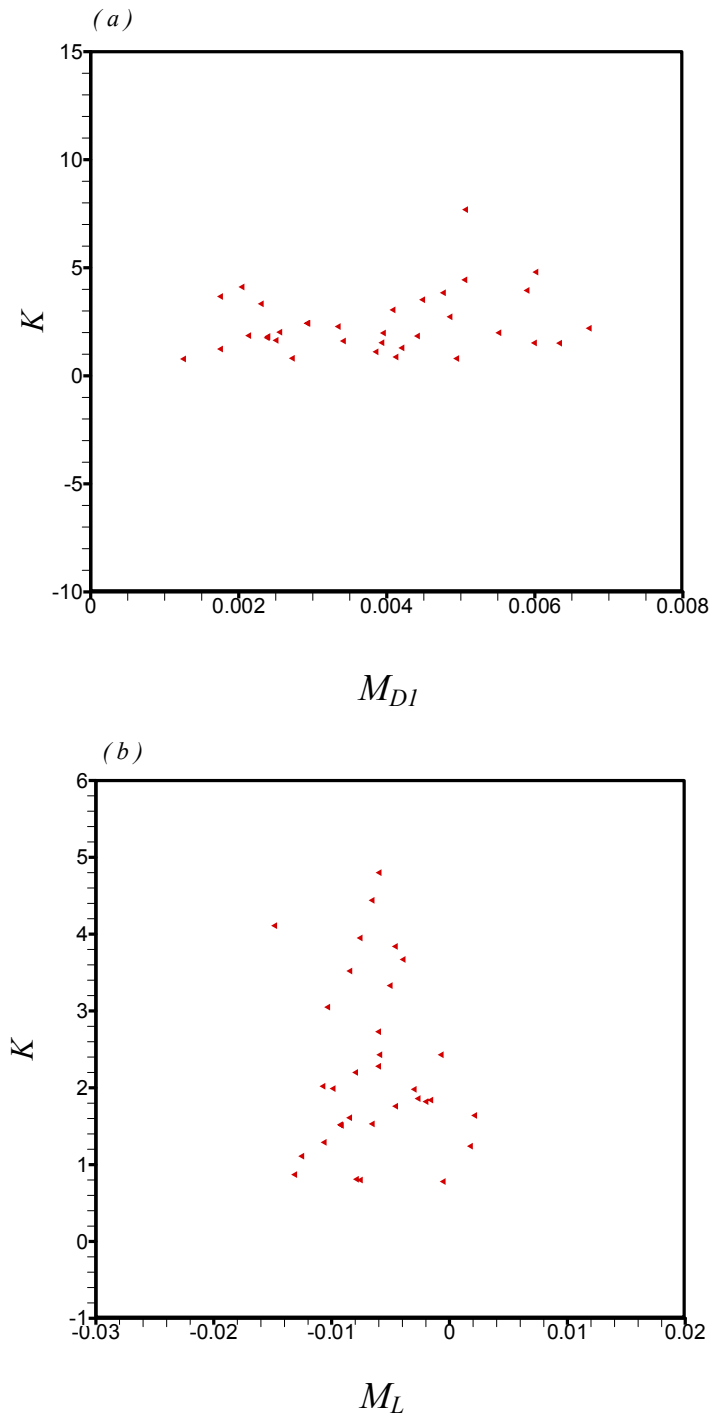
Figure 5.11: Variation of M_{DI} and M_L with K during sweep events (K is normalized by u_τ^2, M_{DI} and M_L are normalized by $\rho u_\tau^2 d^3$).

(a)

M_{Dl}/M_L

(b)

M_{Dl}/M_L
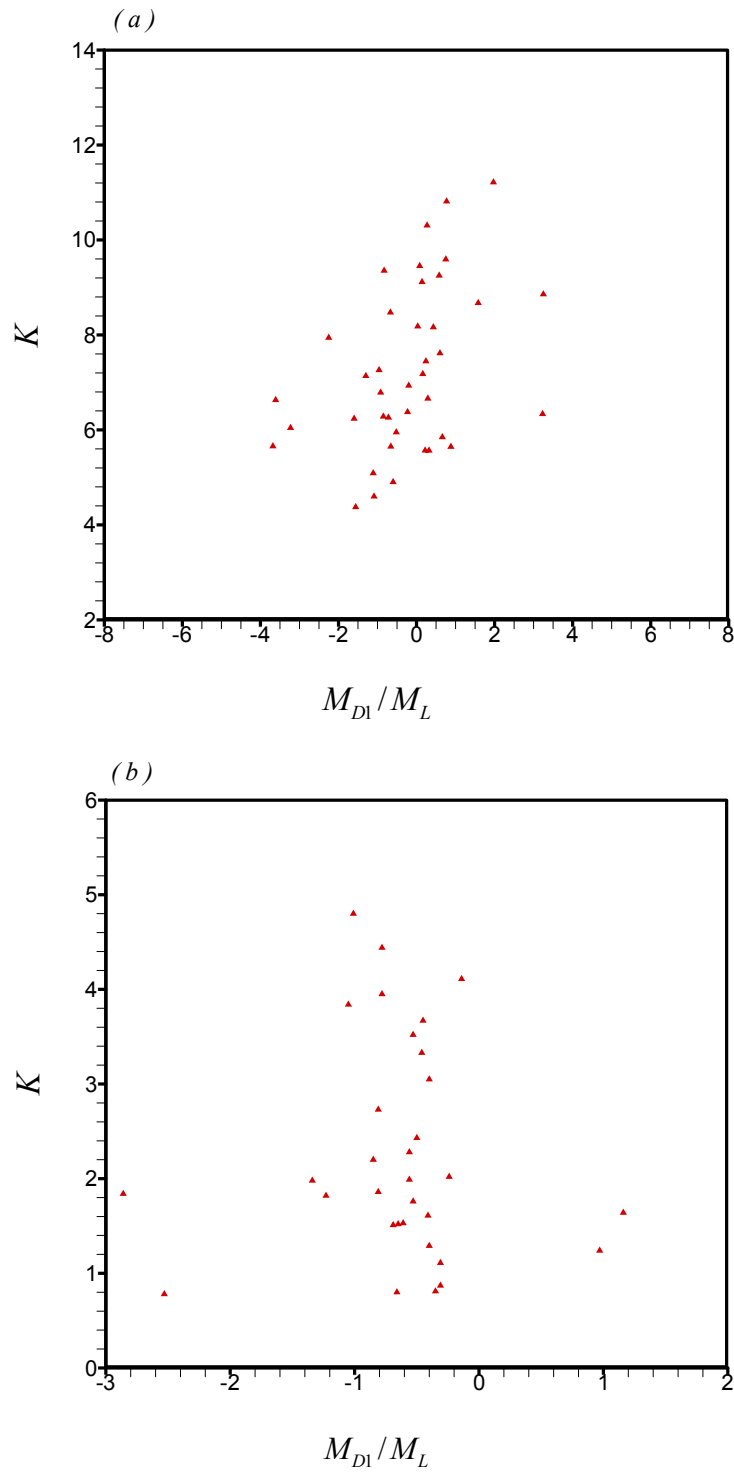
Figure 5.12: Variation M_{Dl}/M_L with K during ejections and sweeps
(K is normalized by u_τ^2).

An interesting phenomen is that for both events, the pressure part of M_{DI} and M_L have an inverse relationship owing to the position of the event. The increase of the moment lever arm in the streamwise direction will result in a decrease of the moment lever arm in the vertical direction. Another noteworthy feature is that more ejections and sweeps occur on the upstream side of the sphere than on the downstream side. In general, more spanwise vortices occur above the centre of the sphere than elsewhere thus producing ejections on the upstream side and sweeps on the downstream neighbour.

The effect of the velocity components of bursts are shown in Fig. 5.13 & Fig.5.14. This actually corresponds with the traditional formula for M_{DI} as a function of local streamwise velocity as an increase of u' causes u to increase for sweep and decrease for ejection. For both events, u' is the determinant for M_{DI}, rather than v'. In the analysis of Hofland et al. (2006), fluctuating drag force depended mainly upon horizontal velocity, not the vertical one, for highly exposed particles. But vertical velocity also accounted for the shielded particles. In this study, the hexagonally arranged spheres are of the same diameter; the upper half part is totally exposed to the flow actually. It is more similar to the condition of high exposure in his work.
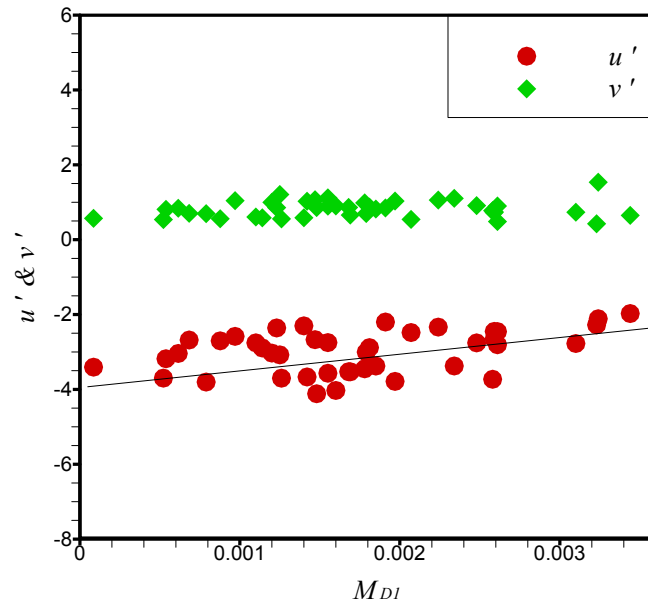
Figure 5.13: Relation between u',v' and M_{D1} during ejections (u' and v' are normalized by u_τ, M_{D1} is normalized by $\rho u_\tau^2 d^3$).
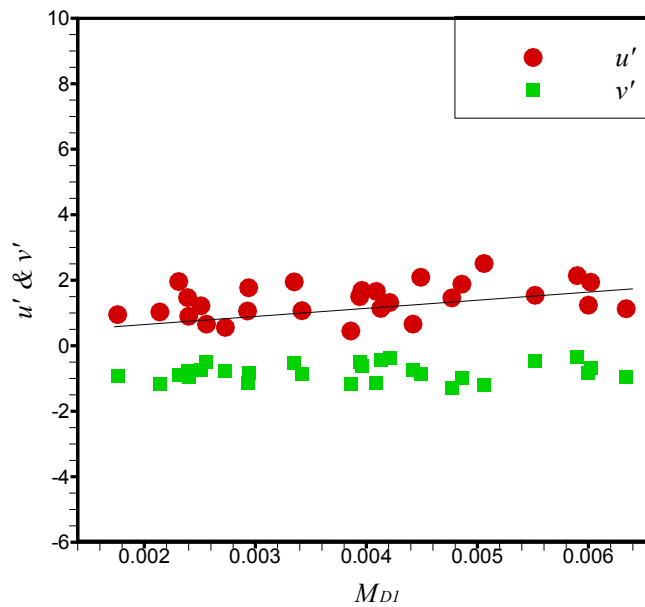
Figure 5.14: Relation between u',v' and M_{D1} during sweeps (u' and v' are normalized by u_τ, M_{D1} is normalized by $\rho u_\tau^2 d^3$).

5.4 Summary and discussion

The results from a Direct Numerical Simulation of turbulent open-channel flow are used to reveal the relationship between near-wall coherent structures and gravel bed entrainment.

The quasi-streamwise vortices are shown to be closely related to the spanwise drag moment. The vortices themselves, together with the high-speed upwash and downwash fluid between the vortices, create the pressure difference on the particle surface and consequently the spanwise drag moment. The linear relationship between the enstrophy of quasi-streamwise vortices and spanwise vortices is helpful for the modeling of sediment entrainment. But it depends upon several factors, such as the ratio of gravel diameter to vortex diameter, the shape of the gravel, the position of the vortex, the exposure of the gravel, etc.

The bursting events, both of ejections and sweeps, are greatly associated with the streamwise drag and lift moments. During ejections, the stronger events can increase the lift moment but decrease the streamwise drag moment whereas during sweeps, more intensive events can cause large streamwise drag moments and large lift moments. When it comes to the influence of bursting events on the particle entrainment, ejection is shown to be more favorable than sweep for the threshold of entrainment on account that both of M_{DI} and M_L can be positive if the ejection is strong enough, but M_L is mainly negative and larger than M_{DI} for almost all of the

sweeps.

The relationship between fluctuating velocities and M_{D1} for the bursts is also revealed. During both ejections and sweeps, the fluctuating velocities in the streamwise direction, rather than vertical direction, appear to determine M_{D1}. However, such an obvious effect of velocity fluctuation on M_L is not observed. In real conditions, bursting events are actually three-dimensional, whether or not the fluctuating velocity in spanwise direction, *w'*, also plays a role is not clear. It is a good topic for future research to take into account all the three velocity components. It may help to explain the difference of opinions regarding the effect of bursts on sediment entrainment.

Chapter 6
Entrainment of Sediment Bed

6.1 Literature Review

The study of hydrodynamic forces acting on bed particles in open-channel flow is one of the most important topics regarding sediment transport. For coarse particles, there are two ways for the initiation of motion: sliding and rollover. However, the mechanisms involved in the threshold are still not clear. The initiation of entrainment depends on the balance of force moments exerted on the sediments:

$$F_D L_D + F_L L_L > F_W L_W \qquad (3)$$

where F_D is drag force in the streamwise direction, F_L is lift force in the vertical direction, F_W is submerged gravitational force, L_D, L_L and L_W are lever arms of drag, lift and submerged gravity respectively. Drag force is mainly produced by the flow velocity and lift force is due to the unequal distribution of pressure over the surface of the particle (Fig.6.1). The forces exerted by the fluid vary from particle to particle due to size, exposure and local fluid velocity etc.

A large number of experimental and theoretical studies have been carried out so far. However, due to the difficulty of obtaining detailed data along the surface of particles, particularly the lower surfaces, the prediction of the bed stability is far from accurate.
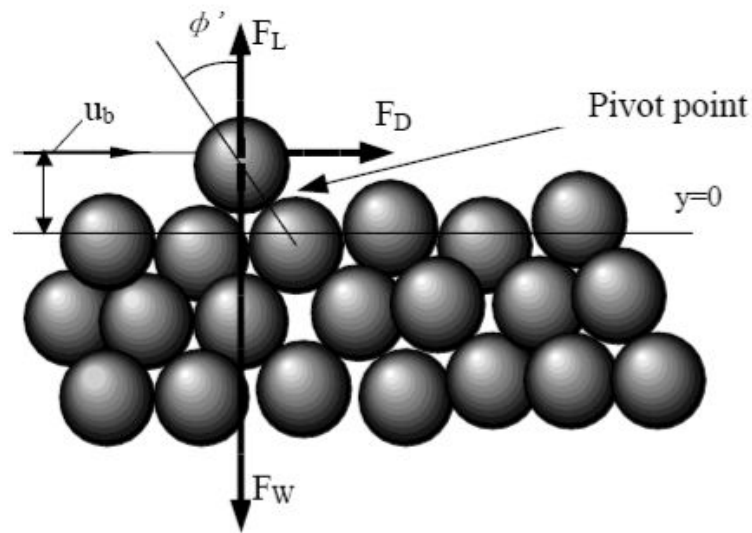
Figure 6.1: Drag and lift forces exerted on a sediment particle (Zanke, 2004).

Einstein and El-Samni (1949) reported the importance of lift force on the entrainment of particles from a rough bed, which was divided into an average value and a fluctuating part. The drag force could be predicted by the logarithmic law whilst the lift force was not. Their results simply indicated that the origin of the lift force was absolutely different from the drag force. The latter was determined by the main stream velocities whilst the former was influenced by the turbulence. Lift force was the dominant factor for the rollover of sediment particles.

Davies and Samad (1978) reported the features of lift force on a bed particle. The result indicated that if the particle Reynolds number was less than 5 and flow could reach the area beneath the particle, the lift force could be negative. This implied that in the loose bed condition, the particle

Reynolds number could totally change the threshold of movement. The variation of bed form, from ripple to dune, could also be explained by the increase of particle Reynolds number. The small particle Reynolds number caused the sediment to rest on the bed and the large particle Reynolds number caused the sediment to suspend.

Wiberg and Smith (1987) proposed an equation for the critical shear stress based on the roughness Reynolds number. The effect of bed geometry was represented by particle repose angle. The repose angle was determined by the ratio of particle diameter to bed roughness. The increase of particle diameter would cause the decrease of repose angle and consequently, the decrease of critical shear stress. Their calculation suggested that particle protrusion was also an important factor for the critical shear stress if the bed was composed of grains of different sizes. Moreover, both of the flow Reynolds number and flow depth limited the application of the equation as the drag force was variable under different flow conditions.

Similarly, Wu et.al (2000) proposed a correction factor for the calculation of the critical shear stress of entrainment. This factor, associated with the size and gradation of bed particles, was taken as a function of the hiding and exposure probabilities. Better agreement could be seen compared to the models which just considered particle size.

James (1990) proposed a model for the entrainment of non-uniform and non-cohesive sediments. His model was based on the moments of the forces about their pivots at the point of initial movement and a group of

parameters were used to quantify the effect of packing conditions. The velocity at the top of the particles was taken as the characteristic velocity for the computation of the drag and lift forces and the lift force coefficient was expressed in terms of the drag force coefficient. In transiton and smooth boundary conditions, the ratio of the lift coefficient to drag coefficient was a function of roughness Reynolds number and; the prediction seemed to be greatly dependent on this ratio.

The dynamic lift originating from turbulent structures was also investigated by Dittrich et al. (1996). In their experiments, glass spheres and cubes were used to represent the artificial roughness. They found that sweep events were the dominant coherent structures near the rough wall. The ratio of lift force to drag force decreased considerably due to increase of roughness. As a consequence, they suggested a roughness density parameter to be added in the analysis of gravel bed stability.

Ling (1995) derived two entrainment criteria for rolling and lifting separately. The only empirical coefficient used was the drag coefficient and, the lift force for the lifting mode for large Reynolds number was based on the maximum lift force for the rollover condition. The difference between low and high particle Reynolds number conditions was that for the former case, the critical shear stress for lifting was substantially larger than that for rolling; whilst for the latter, there was little difference between two critical shear stresses.

Cheng and Chiew (1998) derived an equation for the probability of sediment pickup. In their model, lifting was the dominant mode for entrainment, i.e. when the instantaneous lift force was greater than the effective gravitational force, the sand particles were picked up from the bed. The probability function agrees well with experimental measurements when the lift coefficient was set to 0.25.

McEwan and Heald (2001) proposed a model for the entrainment of randomly arranged sediment beds. The sediment grains were represented by spheres. They argued that the shear stress for the threshold of entrainment of uniform sediment grains should be described as a distribution of values, instead of a single value. The distribution of critical shear stress was independent of grain size for the uniform sediment beds due to the similarity of bed surface. They also reported the influence of sheltering from the protrusion of upstream sediments on the critical shear stress, which increased with the degree of sheltering.

Wu and Chou (2003) studied the entrainment probabilities for both rollover and suspension in smooth and transitional flows. Their formula included the effect of turbulent fluctuation and bed geometry, as well as modified lift coefficient by particle Reynolds number. The suspension probability increased with the shear stress whereas the rollover probability might decrease for large shear stress. The critical entrainment probability for the initiation of movement not only depended on the threshold shear stress, but the shear Reynolds number. Thus, the critical entrainment probability behaved as a function, instead of a constant.

Wang and Fontijn (1993) experimentally studied the drag and lift forces on the roughness element downstream of a backward-facing step. The mean drag force increased linearly with the square of mean streamwise velocity, which was taken at the height of 0.15 mean particle diameter above the element. The similar relationship for the lift force could be observed far away downstream. Also, the fluctuating forces were shown to be as significant as the mean force and, the instantaneous lift force could be even three times the mean value in a large number of cases. The spectral analysis of the forces indicated that the low frequency part was the main contributor of the power. Thus, the eddies shedded from the step were supposed to be the reason for the large fluctuation of the forces.

Hofland et al. (2005) measured fluctuating forces on coarse sediments in rough-bed open-channel flow. As usually assumed, both mean value and fluctuation of the forces increased with exposure of the particle. The most energetic drag force fluctuations had low frequencies which could be attributed to large scale flow structures from the main stream. Lift force fluctuations contained high frequency energy arising from near-wall eddies. They concluded that any model of the extreme forces of the threshold of movement was not simply an extension of the average forces. Their quadrant analysis implied that the drag force was determined by both streamwise and vertical velocities. Consequently, the traditional formula, describing the forces as a function of streamwise velocity, was not sufficiently accurate to predict the hydrodynamic forces of entrainment.
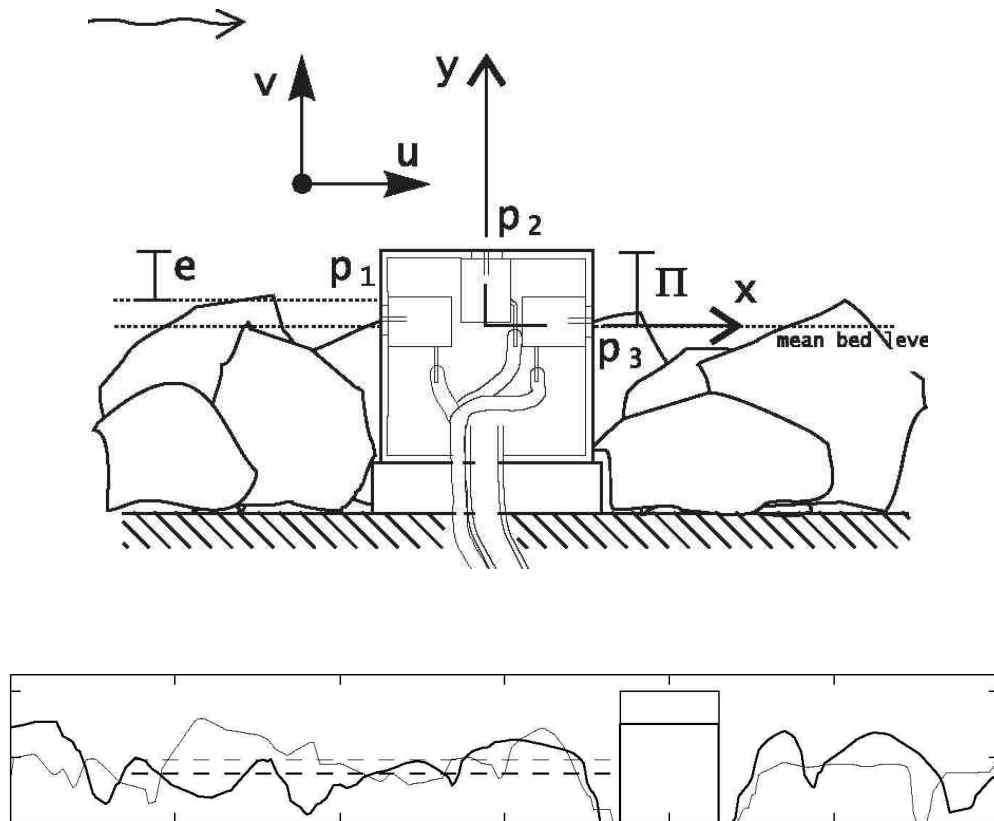
Figure 6.2: Measurement setup of the test cube and bed geometry (Hofland et al., 2005).

The probability density function of the instantaneous drag force developed by Hofland and Battjes (2006) provided new information on the origin of the drag force. The function was based on the normal distribution of near-bed velocity and, for uniform and low turbulent flow, it could forecast the drag force accurately. But in highly turbulent flow, the deviation between the theoretical function and measurements indicated that the drag force no longer could be predicted totally by the traditional function of local near-bed velocity. The influence of near-bed coherent structures, such

as bursting events, quasi-streamwise vortices, etc. must be included in the function in order to predict the fluctuating part.

The effect of particle packing density on the threshold of entrainment was investigated by Dancey et al. (2002). The uniform spherical glass beads of the same density were placed on the gravel bed. The packing density was determined by the amount of glass beads distributed in the test section. Both of the critical shear stress for the entrainment and the bed-load transport rate increased greatly with the packing density. However, the effect of packing density could be negligible when the density was small. Because the particles were isolated, instead of packed. The disadvantage of the experiment was that the influence of the availability of the particles was not filtered from the relationship.

Lick et al. (2004) reported a theoretical description of the entrainment of uniform quartz sediments. The grain size was an important factor as cohesive forces appear for the small grains. In consequence, the threshold shear stress increased when the grain size decreased. The bulk density, as a parameter of packing condition, determined the magnitude of the cohesive force. Cohesive force was important not only because it affected the critical shear stress directly, but it caused the particles to aggregate. The aggregation enlarged the effective lift and drag forces, which resulted in easier entrainment. Further, some mineral material could cause such kind of aggregation, thus should be taken into consideration for the calculation in the real condition.

Cao et al. (1997) proposed a model regarding the relationship between the bursting process and sediment entrainment in open-channel flows. The bursting process was represented by mean duration and the intensity, which was taken as the fractional contribution of the vertical burst intensity to total vertical turbulent intensity. The model could basically predict the concentration distributions of the suspended sediments.
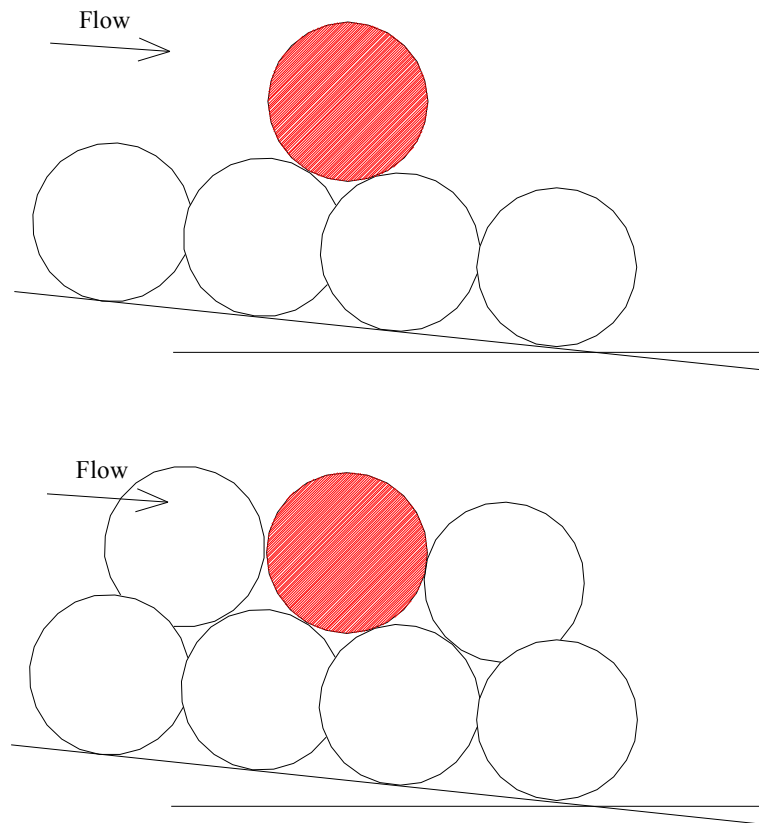
Figure 6.3: Fully exposed and fully packed conditions of uniform spheres (Papanicolaou, 2002).

Papanicolaou et al. (2002) further developed a model based on the concept that near-bed turbulence was the dominant role for sediment entrainment. Three bed-packing conditions: isolated, wake interference and skimming were taken into consideration in this model. The isolated and wake flow conditions were represented by a particle fully exposed and; the skimming condition was represented by the particles well packed (Fig.6.3). The evidence in their study indicated that the probability of occurrence of turbulent events was equal to sediment entrainment probability for a large number of cases and, the conventional assumption of the flow parameters being described by a normal distribution in stochastic models was not accurate for the prediction.

On the other hand, the features of sediment particles for initial sediment movement have also been investigated. Ashworth and Ferguson (1989) observed size-selective entrainment of bed-load movement, namely entrainment depended only on absolute particle size, even if the bed material contained mixed size gravels.

Cube	Sphere	Rect. Prism	Rect Prism	Irregular
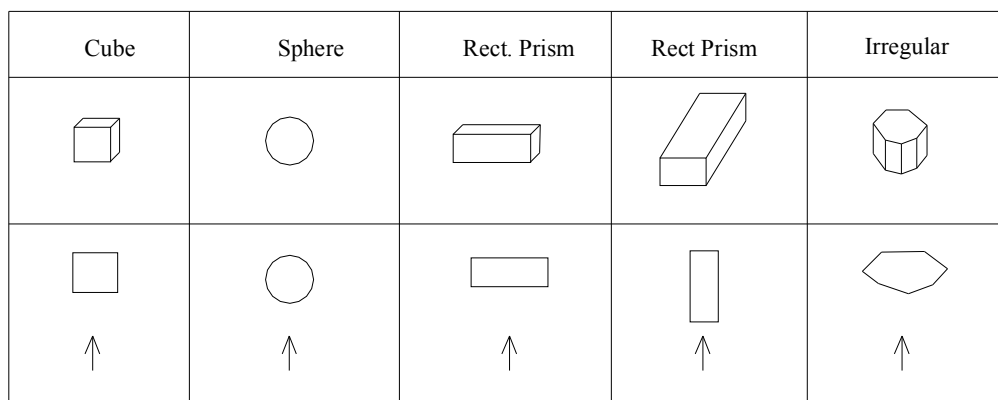
Figure 6.4: Particle shapes and plan view in flow direction (Mogus and Defne, 2005).

Gogus and Defne (2005) studied the effect of size and shape on the entrainment, including spheres, cubes, prisms and irregular particles, in a tilting flume (Fig.6.4). The threshold of movement was determined by the slope of the flume. It was observed that particle Reynolds number increased as the shape factor decreased at the threshold of movement and that the required critical shear stress was smaller for coarser particle grains with similar volume. The results also revealed that entrainment was influenced by the ratio of flow depth to grain diameter.

As reviewed above, sediment entrainment is determined by two aspects; one is the features of sediment, the other is the flow condition. The features of sediment are particle shape, size, density, packing condition, etc.(Wiberg and Smith 1987, Dancey et al. 2002, Papanicolaou et al. 2002, Ashworth and Ferguson 1989, Gogus and Defne 2005) and the flow condition is characterized by the representative velocity. For a long period, the representative velocity was taken as the local mean streamwise velocity. However, the studies recently suggested that the velocity fluctuations, which were related to near-wall bursts and vortices, could be as significant as mean velocity. This implies the importance of fluctuating forces on sediment entrainment (Wu and Chou 2003, Wang and Fontijn 1993, Hofland et al. 2005).

Because the near-wall coherent structures are three-dimensional, it is more reasonable to perform a three-dimensional analysis on the forces. Further, the drag and lift forces will be compared in this study in order to determine which is the dominant factor for gravel entrainment. The location of

effective lift force will also be explored as most of the previous works assumed that it was at the center of sediment particles. However, it should be pointed out that the location is variable for different bed conditions.

6.3 Drag Force Moments

Traditionally, the analysis of the hydrodynamic forces acting on bed gravels has been mainly two-dimensional. The drag force on the sediment is taken to be in the streamwise direction and is determined by the streamwise flow velocity. The horizontal force in the spanwise direction has mostly been neglected. In this fully developed turbulent rough-bed flow, the spanwise horizontal force has been found to be of the same order of magnitude and, in some cases, even larger.

The probability density function (PDF) of a single variable is written as $\int_{-\infty}^{\infty} PdX = 1$ (Bradshaw, 1971). P represents the probability of the variable lying between $X - dX/2$ and $X + dX/2$. The moments in the spanwise direction are calculated and compared with the streamwise drag moment using the data of different letouts (Ma and Williams, 2009a).

The two drag moments are totally different. The probability density distributions (Fig.6.5 & Fig.6.6) show that M_{D1} is mainly positive, with just a few exceptions, whilst M_{D2} is symmetrically distributed around 0. This suggests that the origin of the F_{D2} is different from that of F_{D1} and implies that the traditional approach used to describe the streamwise drag moment cannot be used to describe the spanwise drag moment. It is conjectured that this kind of distribution is due to the quasi-streamwise

vorticies, most of which occur as counter-rotating vortex pairs. The existence of a spanwise drag moment not only changes the total horizontal drag moment, but also the lift moment. The combination of the two horizontal drag force moments, which is different for every individual sphere, determines the rolling direction of the sphere and in consequence, the actual moment produced by the lift force at the threshold of entrainment.

Fig.6.7 & Fig.6.8 describe the probability distribution functions of pressure and viscous force to effective streamwise and spanwise drag moments respectively. For the streamwise drag moment, the contributions from pressure and viscous forces are roughly equal. For spanwise drag moments, the main contributor is pressure: viscous force contributes only approximate 20% of the total moment but pressure contributes 80%. This implies that the flow structure produces large pressure differences on the sphere surface in spanwise directions and forces the sphere to rotate. This again can be attributed to the quasi-streamwise vortices which create low pressure areas on sphere surfaces.

As summarized by Bridge and Bennett (1992), the displacement of the drag force in the streamwise direction is mostly taken as $0.5\sim0.7$ times the diameter of grain above the bed level. The real position depends upon the local velocity and bed packing condition.
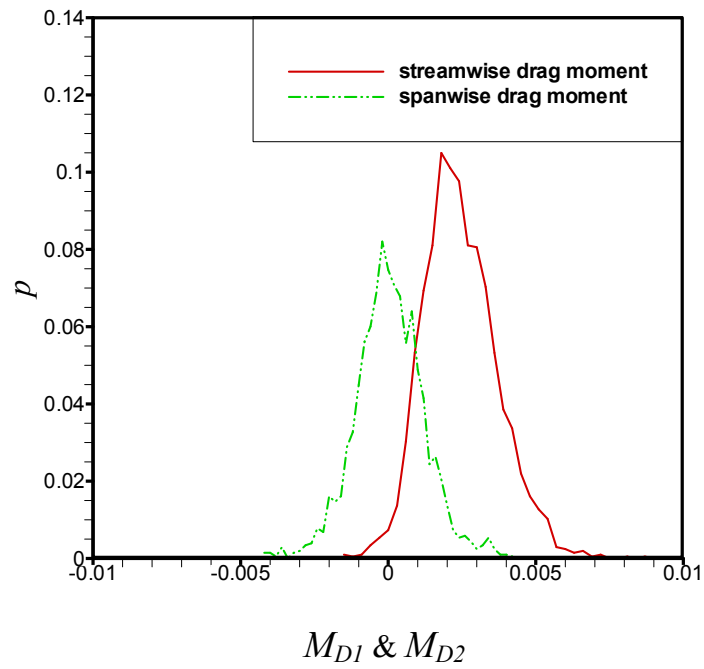
M_{D1} & M_{D2}

Figure 6.5: Probability distribution of M_{D1} and M_{D2}
(M_{D1} and M_{D2} are normalized by $\rho u_\tau^2 d^3$).
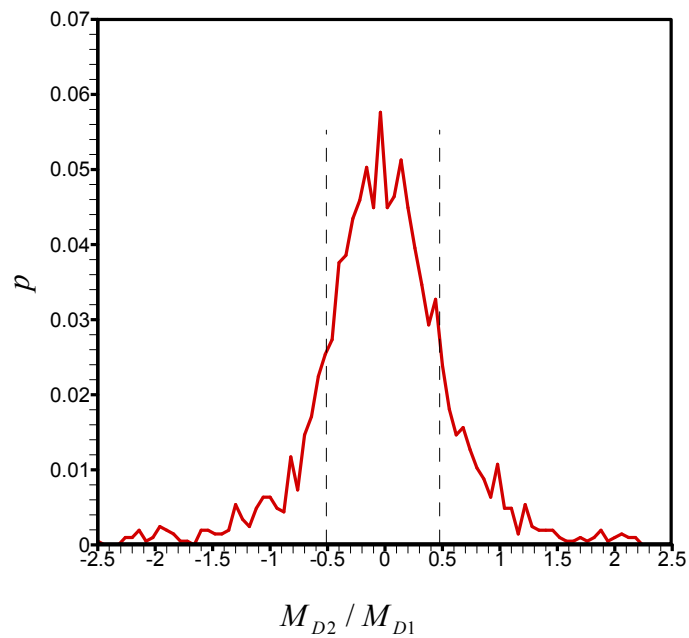
M_{D2} / M_{D1}

Figure 6.6: Probability distribution of M_{D2} / M_{D1}.
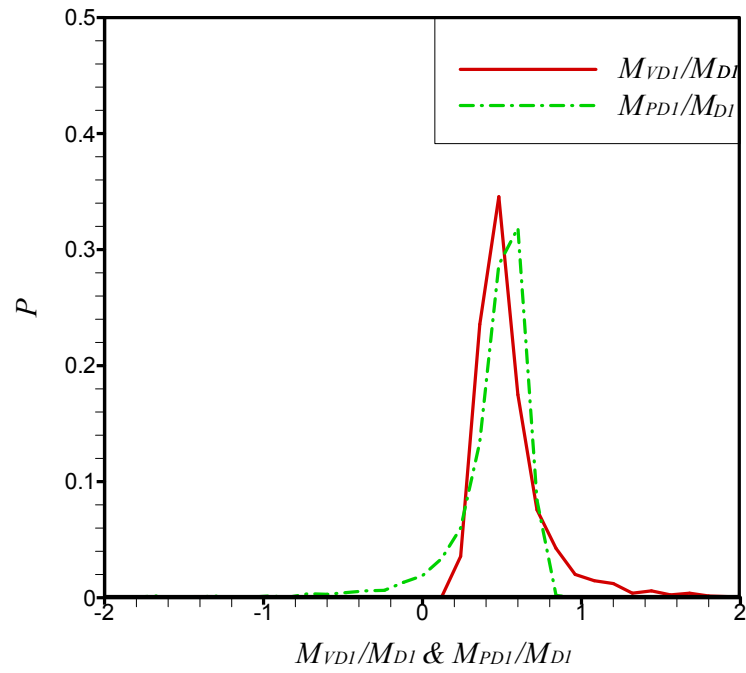
Figure 6.7: Probability distribution of M_{VD1}/M_{D1} & M_{PD1} /M_{D1}.
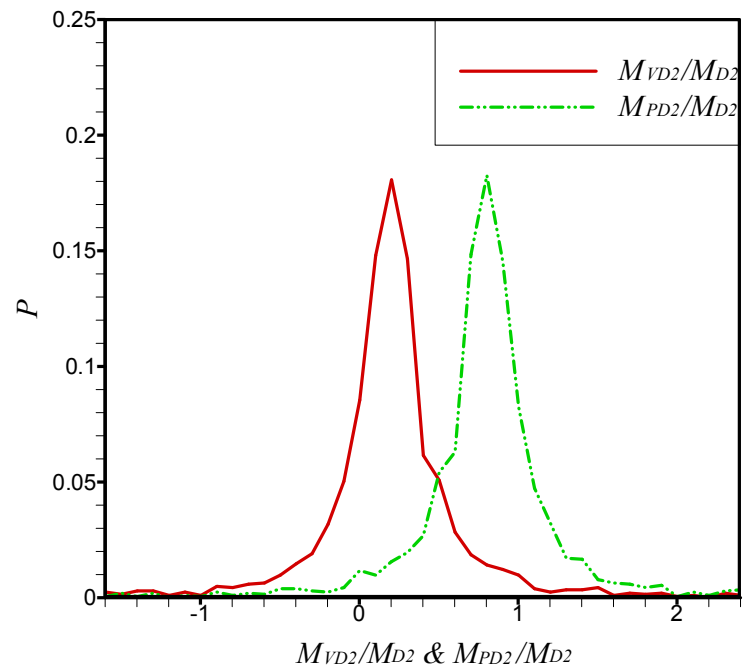
Figure 6.8: Probability distribution of M_{VD2}/M_{D2} & M_{PD2} /M_{D2}.

The height of the sphere is divided into eight equal regions and the contributions of the forces from different regions of the sphere to the total moment are calculated. R_i and r_i represent the contributions from the different regions (from bottom to top), where $R_i = M_{D1i} / M_{D1}$, and, $r_i = M_{D2i} / M_{D2}$, $i = 1 \sim 8$.

As shown in Fig.6.9~Fig.6.12, for all of the eight regions, the distributions in spanwise direction are much wider than in streamwise direction. Such differences indicate a more random mechanism accounting for M_{D2} than M_{D1}. It can be seen that PDFs are symmetrical around 0 below the middle plane of the spheres. For $R(5)$ and $r(5)$, the PDFs become more adjacent to 0, which can be taken as a critical region. After that, the PDFs move towards the positive direction.

Apparent differences can be observed in that the moment on the top $d/8$ area contributes much more to the total moment in the streamwise than the spanwise direction. In the latter case, it increases gradually from the middle plane to the top. The increasing trend of M_{D1} can be explained well by the log law of local streamwise velocity as it increases greatly from the effective bed level. This also indicates the different origins of the two horizontal forces: the former principally from the local streamwise velocity whilst the latter related to quasi-streamwise vortices.
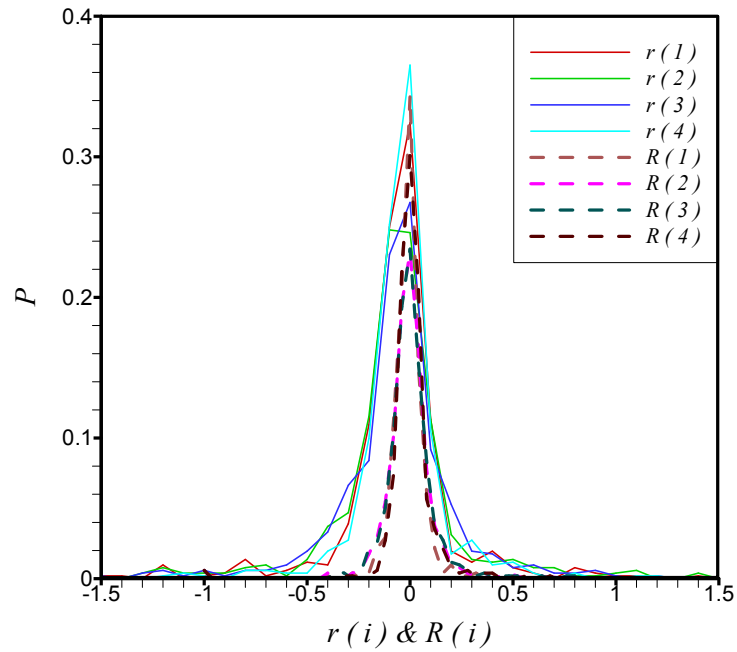
Figure 6.9: Probability distribution of contributions to total moment from $i = 1 \sim 4$, $R(i) = M_{D1i}/M_{D1}$ and $r(i) = M_{D2i}/M_{D2.}$
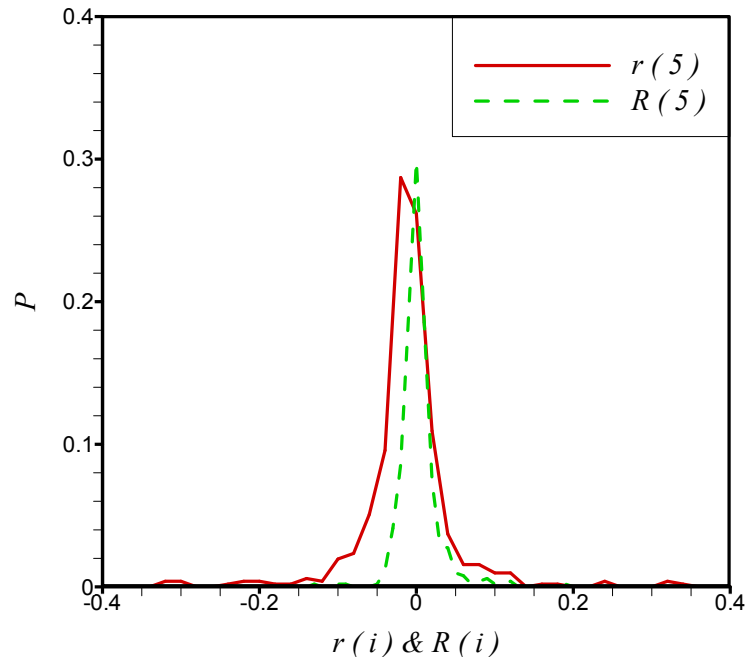
Figure 6.10: Probability distribution of contributions to total moment from $i = 5$, $R(i) = M_{D1i}/M_{D1}$ and $r(i) = M_{D2i}/M_{D2.}$
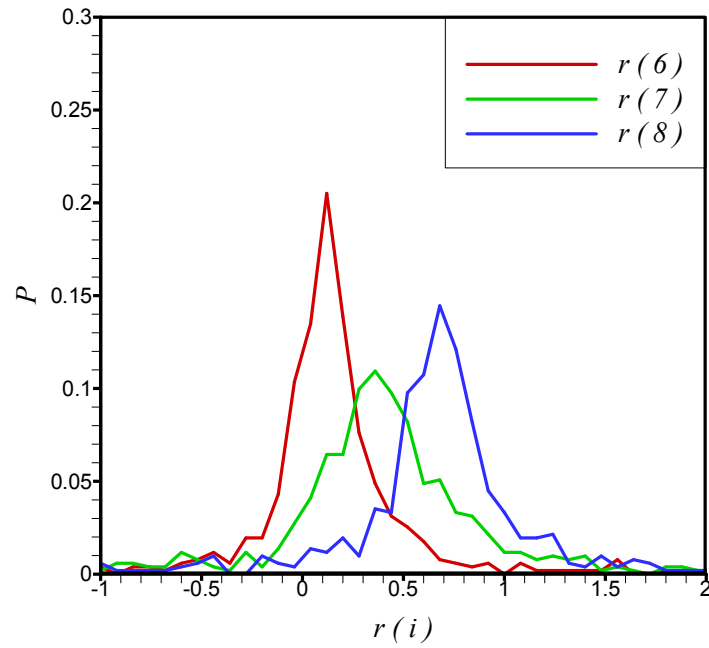
Figure 6.11: Probability distribution of contributions to total moment from $i = 6\sim8$, $r(i) = M_{D2i} / M_{D2}$.
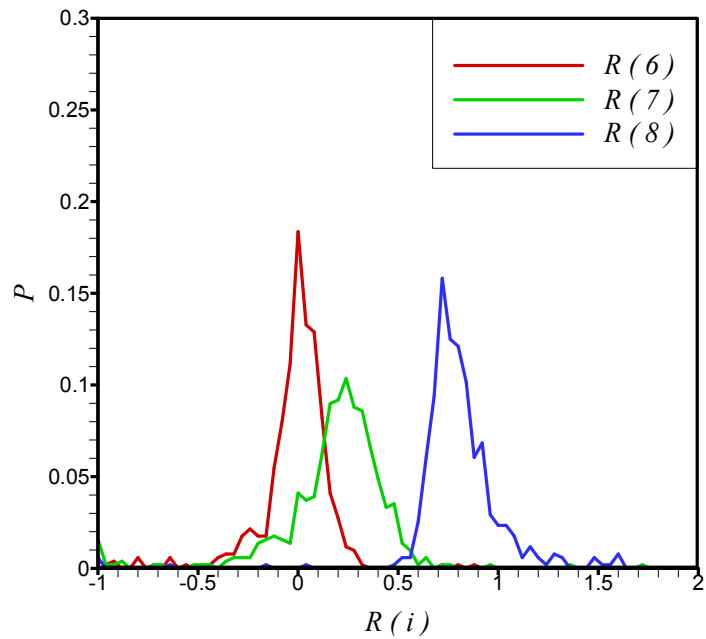
Figure 6.12: Probability distribution of contributions to total moment from $i = 1\sim4$, $R(i) = M_{D1i} / M_{D1}$.

On the other hand, in Fig.6.9, for some cases in both conditions, the contributions from the lower part of the spheres can be quite large, indicating that some flow events can approach the bottom area of the spheres and make a considerable contribution. For spanwise conditions, it is observed to be high-speed fluid between the quasi-streamwise vortices. For the streamwise conditions, the well-known bursting events are the main contributor.

6.3 Lift Force Moments

As reviewed by James (1990), there is a considerable body of opinion that attribute entrainment to the drag force. The lift force is generally considered to be one order of magnitude smaller than the drag force and thus a secondary factor for entrainment unless the particle Reynolds number is considerably large. On the contrary, Einstein and El-Samni (1949) concluded that the lift force is the deterministic factor for entrainment. Here, an inverse relationship is observed for the instantaneous streamwise drag moment and lift moment (Fig.6.13). Instantaneous flow fields show that sweeps are the most frequent events related to large M_{DI}, following by spanwise vortices. Large M_L is apparently associated with the vortices, either quasi-streamwise or spanwise. Hofland et al (2005) stated that during their experiment, vortex shedding only caused lift force fluctuations. In our simulation, vortex shedding accounts for both streamwise drag force and lift force fluctuations, depending upon the direction and position of the vortex. Only in rare cases, when the spanwise vortex occurs above the sphere, can the sphere experience large M_{DI} and M_L simultaneously. As shown in Fig.6.13, large M_{DI} appear with large negative M_L; such a combination cannot in fact cause entrainment. But when M_L is positive, M_{DI} can be positive in a large number of cases, though possibly slightly smaller than M_L. Therefore, for the threshold of entrainment, the lift force is much more significant than the drag force.
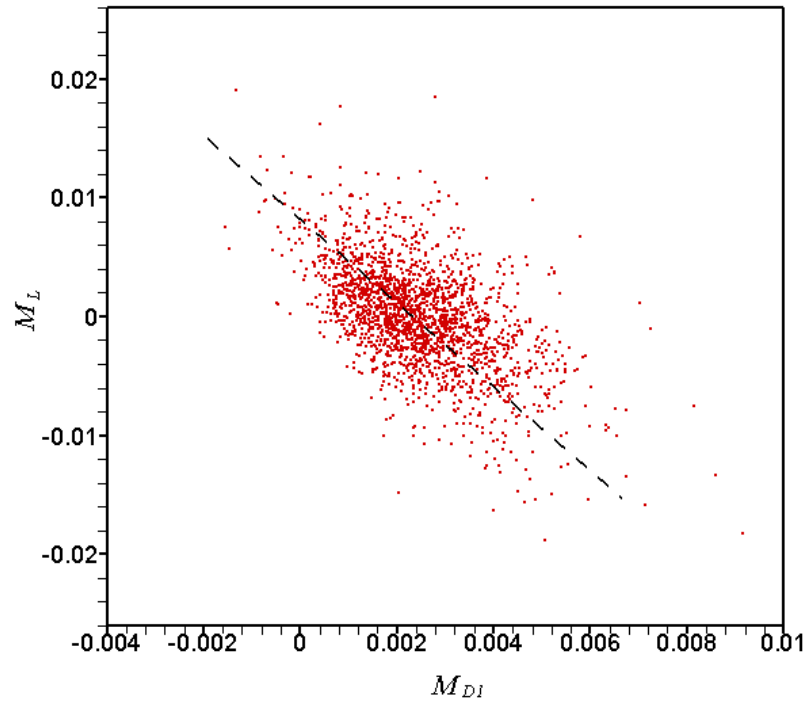
Figure 6.13: Instantaneous M_{DI} vs. M_L. (M_{DI} and M_L are normalized by $\rho u_\tau^2 d^3$).
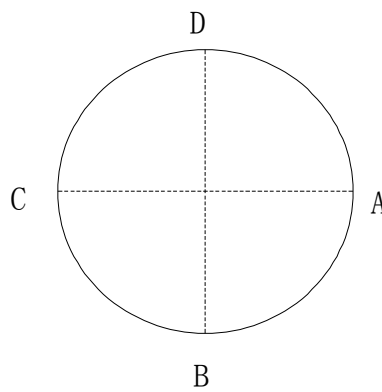
Figure 6.14: Four reference points of lift force moment (top view).

To date, there is no agreement on the position of the lift force and it is normally taken through the center of the sphere for simplication in the modeling of sediment entrainment. The moments of the lift force of the four reference points: *A, B, C, D* (Fig.6.14) are computated to determine the real position. If the effective lift force acts through the center of the sphere, the moments should be equivalent to each other approximately. However, Fig.6.15 shows that the lift force on the surface of sphere is quite randomly distributed, not symmetrical in either streamwise or spanwise directions. The position of effective lift force is near the center line in the spanwise direction but in the streamwise direction, approximately 0.2 times the gravel diameter downstream of the center line.
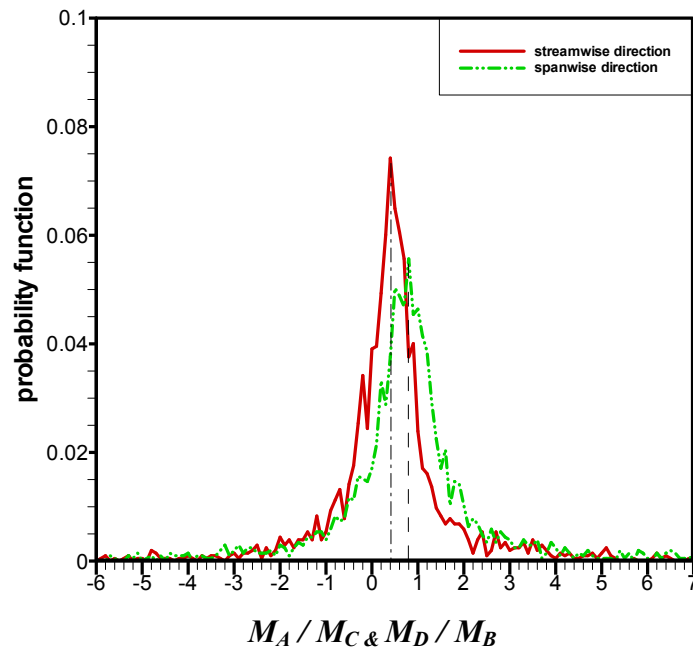
Figure 6.15: Comparison of the lift force moments
in the opposite directions.

6.4   Summary and Discussion

The features of drag and lift moments are explored, which act on the bed gravels for the threshold of entrainment in both streamwise and spanwise directions. The probability distribution of the spanwise drag moment, which has been ignored previously, is shown to be an important factor for the total horizontal moment and the effective lift moment. Pressure is demonstrated to be the main contributor for the spanwise drag moment, whilst the viscous force is equally important for the streamwise drag moment.

The contributions from vertical regions along sphere height to these two drag moments are totally different as shown by the probability density function. The majority of M_{D1} originates from the top surface of the spheres where the contribution increases sharply. On the contrary, the distribution of M_{D2} increases gradually over the divided sub-regions. All these differences between the two drag moments make it impossible to describe the total horizontal drag moment as a function of local streamwise velocity.

The position of the effective lift force is actually not at the center of the particle as idealized by many works previously, which should be roughly 0.2 times the particle diameter downstream of the particle center line.

The comparison of streamwise drag moment and lift moment reveals that the lift force is more important than drag force because even if the drag

force moment is large, the simulataneous lift force moment tends to be negative and causes the particles to remain stable. Only when the lift force moment is positive can the threshold of movement occur.

Chapter 7
Conclusions and Recommendations

7.1 Conclusions

The data of a DNS and a LES of turbulent open-channel flow with a rough wall are employed to study the characteristics of large-scale coherent structures and the mechanism of bed entrainment. The findings are summarised in the following two subsections.

7.1.1 Large-scale Flow Structures

Large-scale coherent structures are located in the wall region and the inter-mediate region of the channel whilst the head of the hairpin vortices can reach the free-surface region. The length of the meandering structures is larger than the length of the computational domain, here roughly 20 times the effective flow depth, and the width is one order of magnitude smaller than the length. The structures are composed of a group of vortices aligned in the streamwise direction: small quasi-streamwise vortices at the bottom, larger quasi-streamwise vortices and asymmetric hairpin vortices above. The signature of the structures is the local maximum momentum of streamwise velocity between the counter-rotating vortex pairs. The elongated alternating high-speed and low-speed regions can properly explain the growth of the streaks with flow depth.

More than half of the total Reynolds Stress and Turbulent Kinetic Energy is contributed from the large structures, particularly from the near-wall quasi-streamwise vortices. The contributions to the kinetic energy from u', v' and w' show very similar distributions according to the Q value, i.e. the large coherent structures play an important role for all of the three components. The energy variation along with the flow depth indicates that u' is the main contributor for the total energy. The cumulative distributions of Reynolds Stress and Turbulent Kinetic Energy imply that both of the Reynolds Stress and energy, beneath and above the structures, can be activated simultaneously. The vertical fluctuating velocity is activated from the top of roughness to nearly the free surface, which is suspected due to the high-speed upwash and downwash fluid between the counter-rotating vortices.

The growth of the large-scale coherent structures due to the enlargement of the computational domain is clearly observed by both Q-method and two-point correlations. The structures in the large box are much longer and more complicated than those in the small box. But the large box is simply not large enough to capture the full growth of the structures. Therefore, even under rough-wall conditions, the large-scale structures could be longer than 20 times the effective flow depth. The width of the computational box is as important as the length since the orientation of the large structures is pretty random, instead of strictly along the streamwise direction. The organization and evolution of the flow structures might be constricted if the width is not enough. Thus, the physical properties of the structures and the whole flow field are determined by the size of the

computational or experimental domain.

7.1.2 Bed Entrainment

The results of the DNS are used to study the features of the drag and lift moments for the threshold of movement and to reveal the relationship between near-wall coherent structures and gravel bed entrainment.

The spanwise drag moment is shown to be greatly determined by the near-wall quasi-streamwise vortices. The position of the vortices controls the direction of the spanwise drag moment and in consequence, the direction of movement. There is an inverse linear relationship between the enstrophy of the vortices and spanwise drag moment, which indicates that the energetic vortices, with small enstrophy, can produce large spanwise drag moment. Also, the adjacent high-speed downwash fluid generates high pressure on the sphere, which enlarges the pressure difference and eases the entrainment. However, the counter-rotating vortex pairs above the sphere may be not able to produce large pressure difference due to the counter-balance effect.

Both of the bursting events, ejections and sweeps, are closely related to the streamwise drag moment and lift moment. For the ejections, large streamwise drag moment is caused by weak ejections whereas large lift moment is produced by strong ejections. On the other hand, sweeps can cause both large streamwise drag and lift moments. The comparison of the

relationships between the kinetic energy of bursts and the ratio of M_{D1}/M_L indicates that particles are more easily entrained by ejections than sweeps. During strong ejections, both of M_{D1} and M_L can be positive, but during all of the sweeps, M_L is generally negative and larger than M_{D1}. Therefore, even if sweeps can produce large M_{D1}, the total effective moment is possibly not promising for the entrainment.

The relationship between fluctuating velocities and streamwise drag moments shows that M_{D1} increases along with u' for both ejections and sweeps. The effect of bursting events on the entrainment is in fact determined by u', instead of v'. However, the effect of spanwise fluctuating velocity w' should be also included in the future as bursts are three-dimensional.

The probability distributions of streamwise and spanwise drag moments are totally different as the former is symmetric around zero and the latter is mainly larger than zero. The distribution of ratio M_{D2}/M_{D1} suggests that M_{D2} is actually important, rather than negligible as previously considered, compared with M_{D1} in a large number of cases. Pressure difference in the spanwise direction is the main reason for M_{D2} whereas viscous force is also an important contributor as pressure for M_{D1}. The vertical distributions of the two drag moments on sphere surfaces are different above the sphere mid-plane. The majority of M_{D1} focuses on the top surface whereas M_{D2} gradually increases from the mid-plane to the top. These differences suggest that the computation of M_{D2} can not be treated

the same as M_{D1}, i.e. as a function of streamwise velocity. The relation between the quasi-streamwise vortices and M_{D2} must be incorporated into the modeling of sediment entrainment.

The position of the effective lift force is confirmed by calculating moments at four reference pivots. It should be approximately 0.2 times the particle diameter downstream of the particle centerline, rather than idealized at the center as previously. Furthermore, the lift force is shown to be more important than drag force for the threshold of movement due to the fact that when the drag force moment is large, the lift force moment is negative and the total effective moment is consequently small; but when the lift force moment is positive, the particles are more likely to be entrained, under the effect of simultaneous positive drag force moment.

7.2   Recommendations

Although a large amount of works have been performed regarding the large-scale coherent structures, the exact length scale is still not clear. Since the vortices are connected to each other gradually, instead of simultaneously, a maximum length scale should apply. The breakup of the conection between the vortices, which causes the evolution of the structure, is the strong evidence. However, the maximum length is simply too large to observe in any computational or experimental domain employed before.

The DNS and LES used in this study is for shallow flow condition. How does the flow depth determine the growth of the large structures, as the vortices themselves grow gradually? The variation of flow depth should influence the vertical development of the structures. The top surface of the channel is treated as a stress-free hard lid in this study. How does the strong wind exerting on the free surface influence the development of the large structures? The effect of wave and current can be added to the free surface though such dynamic effect is complex and not as frequent as quiescent condition for open-channel flows. Also, the reason for the difference between the vortical structures reported by different studies is not clear. In some cases, the hairpin vortices are mainly symmetric although not perfectly; and in the other cases, the hairpin vortices are characterized by single leg as the other one is greatly shortened like the situation in this study. The influence of different kinds of roughness elements on the large-scale structures is an interesting topic as it is one of

the possible reasons for the disturbance of structure organization.

The results regarding the gravel bed entrainment are based on the particular flow and bed packing conditions. Future work should include variation of Reynolds number, flow depth, etc. in order to further quantify the influence. The kinetic energy of the bursts is taken as the only factor for the influence on particle entrainment in this study. The effects of position, vertical direction and horizontal orientation of the events should be also included. For the modeling of sediment entrainment, the quantitative relationships developed in this study can be incorporated into the previous models. The relationship between near-wall coherent structures and force moments can be employed to predict the threshold of sediment movement. The spanwise drag moment can be used to model the rollover directions of the gravels and effective total drag moment. The effective positions of drag and lift forces are helpful to improve the sediment transport equations. In order to investigate the movement of the gravels after the entrainment, the simulation of movable particles should be performed, which includes the effects of particle shape, size, density, protrusion,etc.

References

Adrian, R. J., Meinhart, C. D. and Tomkins, C. D. (2000). "Vortex organization in the outer region of the turbulent boundary layer." *J. Fluid Mech.*, 422, 1-54.

Ashworth, P. J. and Ferguson, R. I. (1989). "Size-selective entrainment of bed load in gravel bed streams." *Water Resour. Res.*, 25(4), 627- 634.

Balakumar, B. J., and Adrian, R. J. (2007). "Large and very-large-scale motions in channel and boundary-layer flows." *Phil. Trans. R. Soc. A*, 365, 665-681.

Bernard, P., Thomas, J. M. and Handler, R. A. (1993). "Vortex dynamics and the production of Reynolds stress." *J. Fluid Mech.*, 253, 385-419.

Blackwelder, R. F. and Haritonidis, J. H. (1983). "Scaling of the bursting frequency in turbulent boundary layers." *J. Fluid Mech.*, 132, 87-103.

Blazek, J. (2001). "Computational Fluid Dynamics: Principles and Applications." Elsevier.

Bradshaw, P. (1971). "An Introduction to Turbulence and its Measurement." Pergamon Press.

Bridge, J. S. and Bennett, S. J. (1992). "A model for the entrainment and

transport of sediment grains of mixed sizes, shapes, and densities." *Water Resour. Res.*, 28(2), 337- 363.

Brooke, J.W. and Hanratty, T. J. (1993). "Origin of turbulence-producing eddies in a channel flow." *Phys. Fluids*, 5, 1011-1022.

Cao, Z. (1997). "Turbulent bursting-based sediment entrainment function." *J. Hydr. Engrg.*, 123(3), 233-236.

Cao, Z., Zhang, X. and Xi, H. (1996). "Turbulent bursting-based diffusion model for suspended sediment in open channel flows." *J. Hydr. Res.*, 34(4), 457-472.

Cellino, M. and Lemmin, U. (2004). "Influence of coherent flow structures on the dynamics of suspended sediment transport in open-channel flow." *J. Hydr. Engrg.*, 130(11), 1077-1088.

Cheng, N.-S. and Chiew, Y.-M. (1998). "Pickup probability for sediment entrainment." *J. Hydr. Engrg.*, 124(2), 232-235.

Dancy, C. L., Diplas, P., Papanicolaou, A. and Bala, M. (2002). "Probability of individual grain movement and threshold condition." *J. Hydr. Engrg.*, 128(12), 1069 - 1075.

Davies, T. R. H. and Samad, M. F. A. (1978). "Fluid dynamic lift on a bed particle." *J. Hydr. Divi.*, 104(HY8), 1171- 1182.

Del Alamo, J. C., Jimenez, J., Zandonade, P. and Moser, R. D. (2006). "Self-similar vortex clusters in the turbulent logarithmic region." *J. Fluid Mech.*, 561, 329-358.

Dittrich, A., Nestmann, F. and Ergenzinger, P. (1996). "Ratio of lift and shear forces over rough surfaces." *Coherent Flow Structures in Open Channels*, John Wiley & Sons Ltd.,125- 146.

Einstein, H. A. and El-Samni E.A. (1949). "Hydrodynamic forces on a rough wall." *Rev. Mod. Phys.*, 21(3),520-524.

Falco, R. E. (1991). "A coherent structure model of the turbulent boundary layer and its ability to predict Reynolds number dependence." *Phil. Trans. R. Soc. A*, 336, 103-129.

Ferziger, J. H. and Peric, M. (2002). "Computational Methods for Fluid Dynamics." Springer-Verlag, Berlin, Heidelberg.

Ganapathisubramani, B., Hutchins, N., Hambleton, W. T., Longmire, E. K. and Marusic, I. (2005). "Investigation of large-scale coherence in a turbulent boundary layer using two-point correlations." *J. Fluid Mech.*, 524, 57-80.

Ganapathisubramani, B., Longmire, E. K. and Marusic, I. (2003). "Characteristics of vortex packets in turbulent boundary layers." *J. Fluid Mech.*, 478, 35-46.

Gogus, M. and Defne, Z. (2005). "Effect of shape on incipient motion of large solitary particles." *J. Hydr. Engrg.*, 131(1), 38-45.

Grass, A. J. (1971). "Structural features of turbulent flow over smooth and rough boundaries." *J. Fluid Mech.*, 50, 233-255.

Grass, A. J., Stuart, R. J. and Mansour-Tehrani, M. (1991). "Vortical structures and coherent motion inturbulent flow over smooth and rough boundaries." *Phil. Trans. R. Soc. A*, 336, 35-65.

Guala, M. G., Hommema, S. E. and Adrian, R. J. (2006). "Large-scale and very-large-scale motions in turbulent pipe flow." *J. Fluid Mech.*, 554, 521-542.

Gyr, A. (1997). "Turbulent flows over smooth erodible sand beds in flumes." *J. Hydr. Res.*, 35(4), 525-544.

Haidari, A. H. and Smith C. R. (1994). "The generation and regeneration of single hairpin vortices." *J. Fluid Mech.*, 277, 135-162.

Hamilton, J. M., Kim, J. and Waleffe, F. (1995). "Regeneration mechanisms of near-wall turbulence structures." *J. Fluid Mech.*, 287,

317-348.

Handler, R. A., Saylor, J. R., Leighton, R. I. and Rovelstad, A. L. (1999). "Transport of a passive scalar at a shear-free boundary in fully developed turbulent open channel flow." *Phys. Fluids*, 11, 2607-2626.

Head, M.R. and Bandyopadhyay, P. (1981). "New aspects of turbulent boundary-layer structure." *J. Fluid Mech.*, 107, 297-338.

Hofland, B., Battjes, J. A. and Booij, R. (2005). "Measurement of fluctuating pressures on coarse bed material." *J. Hydr. Engrg.*, 131(9), 770- 781.

Hofland, B. and Battjes, J. A. (2006). "Probability density function of instantaneous drag forces and shear stresses on a bed." *J. Hydr. Engrg.*, 132(11), 1169- 1175.

Hunt, J. C. R., Wary, A. A. & Moin, P. (1988). "Eddies, stream, and convergence zones in turbulent flows." Center for turbulence Research Report CTR-S88, p.193.

Hurther, D., Lemmin, U. and Terray, E.A. (2007). "Turbulent transport in the outer region of rough-wall open-channel flows: the contribution of large coherent shear stress structures (LC3S)." *J. Fluid Mech.*, 574, 465-493.

Hussain, A. K. M. F. (1983). "Coherent structures- reality and myth." *Phys. Fluids*, 26, 2816-2850.

Hutchins, N., and Marusic, I. (2007). "Large-scale influences in near-wall turbulence." *Phil. Trans. R. Soc. A*, 365, 647-664.

Jackson, R. G. (1976). "Sedimentological and fluid-dynamic implications of the turbulent bursting phenomenon in geophysical flows." *J. Fluid Mech.*, 77, 531-560.

James, C. S. (1990). "Prediction of entrainment conditions for non-uniform, noncohesive sediments." *J. Hydr. Res.*, 28(1), 25-41.

Jimenez, J., Del Alamo, J. C. and Flores, O. (2004). "The large-scale dynamics of near-wall turbulence." *J. Fluid Mech.*, 505, 179-199.

Jimenez, J. and Pinelli, A. (1999). "The autonomous cycle of near-wall turbulence." *J. Fluid Mech.*, 389, 335-359.

Kaftori, D., Hetsroni, G. and Banerjee, S. (1994). "Funnel-shaped vertical structures in wall turbulence." *Phys. Fluids*, 6, 3035-3050.

Kim, H.T., Kline, S. J. & Reynolds, W.C. (1971). "The production of turbulence near a smooth wall in a turbulent boundary layer." *J. Fluid Mech.*, 50, 133-160.

Kim, J. and Moin P. (1986). "The structure of the vorticity field in turbulent channel flow. Part 2. Study of ensemble-averaged fields." *J. Fluid Mech.*, 162, 339-363.

Kim, K. C. and Adrian R. J. (1999). "Very large-scale motion in the outer layer." *Phys. Fluids*, 11, 417-422.

Komori, S., Nagaosa, R., Murakami, Y., Chiba,S., Ishii, K. and Kuwahara, K. (1993). "Direct numerical simulation of three-dimensional open-channel flow with zero-shear gas-liquid interface." *Phys. Fluids*, 5, 115-125.

Krogstad, P. A. , Antonia, R. A. and Browne, L. W. B. (1992). "Comparison between rough- and smooth-wall trubulent boundary layers." *J. Fluid Mech.*, 245, 599-617.

Lick, W., Jin, L. and Gailani, J. (2002). "Initiation of movement of quartz particles." *J. Hydr. Engrg.*, 130(8), 755- 761.

Ling, C.-H. (1995). "Criteria for incipient motion of spherical sediment particles." *J. Hydr. Engrg.*, 121(6), 472-478.

Liu, Z., Adrian, R. J. and Hanratty, T. J. (2001). "Large-scale modes of turbulent channel flow: transport and structure." *J. Fluid Mech.*, 448, 53-80.

Lu, S. S. and Willmarth, W. W. (1973). "Measurements of the structure of the Reynolds stress in a turbulent boundary layer." *J. Fluid Mech.*, 60, 481-511.

Luchik, T. S. and Tiederman, W. G. (1987). "Timescale and structure of ejections and bursts in turbulent channel flow." *J. Fluid Mech.*, 174, 529-552.

Ma, J. and Williams, J. J. R. (2009a). "Implication of horizontal force moments for the threshold of bed entrainment in an open-channel flow." *J. Hydro-enviro. Res.*, 3, 2 - 8.

Ma, J. and Williams, J. J. R. (2009b). " Large-scale coherent structures in turbulent rough-bed open-channel flow." *Proc. 6th Int. Conf. on Turb. Shear Flow Phenomena, Seoul, Korea, 22 – 24 June 2009, Vol. III*, 1137 - 1141.

Ma, J. and Williams, J. J. R. (2009c). "Three-dimensional analysis of the relation between near-bed coherent structures and force moments for bed-load movement." *J. Hydr. Engrg.*, accepted.

Ma, J. and Williams, J. J. R. (2010). "Large coherent structures in Large Eddy Simulation of the open-channel flow." *Proc. 17th Cong. of Asia and Pacific Division of Int. Association of Hydr. Engrg and Res. and 7th Int. Urban Watershed Management Conf., Auckland, New Zealand, 21 – 24 Feb. 2010*, accepted.

McEwan, I. and Heald, J. (2001). "Discrete particle modeling of entrainment from flat uniformly sized sediment beds." *J. Hydr. Engrg.*, 127(7), 588- 597.

Moin, P. and Kim, J. (1985). "The structure of the vorticity field in turbulent channel flow. Part 1. Analysis of instantaneous fields and statistical correlations." *J. Fluid Mech.*, 155, 441-464.

Nakagawa, H. and Nezu, I. (1977). "Prediction of the contributions to the Reynolds stress from bursting events in open-channel flows." *J. Fluid Mech.*, 80, 99-128.

Nakagawa, H. and Nezu, I. (1981). "Structure of space-time correlations of bursting phenomena in an open-channel flow." *J. Fluid Mech.*, 104, 1-43.

Nelson, J. M. and Shreve, R. L. (1995). "Role of near-bed turbulence structure in bed load transport and bed form mechanics." *Water Resour. Res.*, 31(8), 2071- 2086.

Nezu, I. and Nakagawa, H. (1993). "Turbulence in Open-Channel Flows." Balkema, Rotterdam.

Nino, Y. and Garcia, M. H. (1996). "Experiments on particle-turbulence interactions in the near-wall region of an open channel flow: implications for sediment transport." *J. Fluid Mech.*, 326, 285-319.

Pan, Y. and Banerjee, S. (1996). "Numerical simulation of particle interactions with wall turbulence." *Phys. Fluids.*, 8, 2733-2755.

Papanicolaou, A. N., Diplas, P., Evaggelopoulos, N. and Fotopoulos, S. (2002). "Stochastic incipient motion crition for spheres under various bed packing conditions." *J. Hydr. Engrg.*, 128(4), 369-380.

Praturi, A. K. and Brodkey, R. S. (1978). "A stereoscopic visual study of coherent structures in turbulent shear flow." *J. Fluid Mech.*, 89, 251-272.

Raupach, M. R. (1981). "Conditional statistics of Reynolds stress in rough-wall and smooth-wall turbulent boundary layers." *J. Fluid Mech.*, 108, 363-382.

Robinson, S. K. (1991). "Coherent motions in the turbulent boundary layer." *Annu. Rev. Fluid Mech.*, 23, 601-639.

Roy, A. G., Buffin-Belanger, T., Lamarre, H. and Kirkbride, A. D. (2004). "Size, shape and dynamics of large-scale turbulent flow structures in a gravel-bed river." *J. Fluid Mech.*, 500, 1-27.

Smagrinsky, J. (1963) "General circulation experiments with the primitive equations. I. The basic experiment." *Mon. Wea. Rev.*, 91, 99-164.

Schoppa, W. and Hussain, F. (2002). "Coherent structure generation in near-wall turbulence." *J. Fluid Mech.*,453, 57-108.

Sechet, P. and Guennec, B. L. (1999). "Bursting phenomenon and incipient motion of solid particles in bed-load transport." *J. Hydr. Res.*, 37(5), 683-696.

Singh, K. M., Sandham, N. D. and Williams, J. J. R. (2007). "Numerical simulation of flow over a rough bed." *J. Hydr. Engrg.*, 133(4), 386-398.

Smith, C. R. and Metzler, S. P. (1983). "The characteristics of low-speed streaks in the near-wall region of a turbulent boundary layer." *J. Fluid Mech.*, 129, 27-54.

Smith, C. R., Walker, J. D., Haidari, A. H. and Sobrun, U. (1991). "On the dynamics of near-wall turbulence." *Phil. Trans. R. Soc. A*, 336, 131-175.

Soltani, M. and Ahmadi, G. (1995). "Direct numerical simulation of particle entrainment in turbulent channel flow." *Phys. Fluids*, 7, 647-657.

Sumer, B. M. and Deigaard, R. (1981). "Particle motions near the bottom in turbulent flow in an open channel. Part 2" *J. Fluid Mech.*, 109, 311-337.

Toh, S. and Itano, T. (2005). "Interaction between a large-scale structure and near-wall structures in channel flow." *J. Fluid Mech.*, 524, 249-262.

Tomkins, C. D. and Adrian R. J. (2003). "Spanwise structure and scale growth in turbulent boundary layers." *J. Fluid Mech.*, 490, 37-74.

Townsend, A. A. (1976). "The structure of turbulent shear flow." Cambridge University Press.

Wallace, J. M., Eckelmann, H. and Brodkey, R. S. (1972). "The wall region in turbulent shear flow." *J. Fluid Mech.*, 54, 39-48.

Wang, X. and Fontijn, H. L. (1993). "Experimental study of the hydrodynamic forces on a bed element in an open channel with a backward-facing step." *J. Fluids Struct.*, 7, 299-318.

Wiberg, P. L. and Smith, J. D. (1987). "Calculations of the critical shear stress for motion of uniform and heterogeneous sediments." *Water Resour. Res.*, 23(8), 1471- 1480.

Wu, F.- C. and Chou, Y. - J. (2003). "Rolling and lifting probabilities for sediment entrainment." *J. Hydr. Engrg.*, 129(2), 110 - 119.

Wu, F.-C. and Jiang, M.-R. (2007). "Numerical investigation of the role of

turbulent bursting in sediment entrainment." *J. Hydr. Engrg.*, 133(3), 329-334.

Wu, W., Wang, S. S. Y. and Jia, Y. (2000). "Nonuniform sediment transport in alluvial rivers." *J. Hydr. Res.*, 38(6), 427-434.

Zanke, U. C. E. (2003). "On the influence of turbulence on the initiation of sediment motion." *Int. J. Sediment. Res.*,18(1), 17-31.

Zhou, J., Adrian, R. J., Balachandar, S. and Kendall, T. M. (1999). "Mechanisms for generating coherent packets of hairpin vortices in channel flow." *J. Fluid Mech.*, 387, 353-396.